

**NASA
Technical
Paper
2209**

1983

Analysis of Gap Heating Due to Stepped Tiles in the Shuttle Thermal Protection System

**D. H. Petley,
D. M. Smith,
C. L. W. Edwards,
and A. B. Carlson**
*Langley Research Center
Hampton, Virginia*

NASA

National Aeronautics
and Space Administration

Scientific and Technical
Information Branch

1983

Use of trade names or names of manufacturers in this report does not constitute an official endorsement of such products or manufacturers, either expressed or implied, by the National Aeronautics and Space Administration.

CONTENTS

	Page
SUMMARY	1
INTRODUCTION	1
SYMBOLS.....	2
CALCULATION OF PRESSURE DISTURBANCES DUE TO STEPPED TILES	6
INCOMPRESSIBLE STEADY FLOW MODEL	10
STEADY FLOW MODEL WITH COMPRESSIBILITY	15
TRANSIENT THERMAL MODEL	20
Conduction and Radiation	21
Mass Transfer	22
Convection	23
Surface Temperature	24
Gas Inlet Temperature	24
FLOW-TO-THERMAL MODEL INTERFACE	27
CALCULATED FILLER-BAR TEMPERATURES DUE TO STEPPED TILES	28
POTENTIAL SOLUTION TO THE PROBLEM OF FILLER-BAR CHARRING	29
CONCLUDING REMARKS	30
REFERENCES	31
TABLES	33
FIGURES	39



SUMMARY

An analytical study has been performed to investigate excessive heating in the tile-to-tile gaps of the Shuttle orbiter thermal protection system (TPS). The excessive heating caused visible discoloration and charring of the filler bar and strain isolator pad (SIP) used in the attachment of tiles to the aluminum substrate. The study concentrated on determining if tile-to-tile steps and gaps measured after flight could create a sufficient pressure disturbance around a stepped tile to cause hot gas flow in the gaps during entry. Techniques based on existing experimental data were developed to predict the local pressure disturbances. In addition, a technique was devised to approximate the energy potential of the air flowing from the local boundary layer into the tile-to-tile gap. A tile internal flow model, developed previously for the pressure loading on a tile during ascent, was modified to account for compressibility in the flow in the tile-to-tile gaps during entry. The flow model predicts mass flow rates and pressure distributions in the tile-to-tile gaps, in the SIP, and within the tiles. It utilizes analogies between conventional heat conduction and internal gas flow in the calculation procedure. With the flow rates established, a thermal model of adjacent tiles, the tile-to-tile gap, filler bar, and SIP is used to predict temperature distributions throughout the system. An energy balance is maintained on the air flowing through the tile system.

These analytical tools are used to predict conditions under which damage to the filler bar and SIP could occur.

INTRODUCTION

The Space Transportation System (STS) orbiter employs silica tiles in the design of a reusable thermal protection system (TPS). (See fig. 1(a).) The tiles are typically 6 in. by 6 in. and are of variable depth, depending on their location on the orbiter. The tiles are attached to the aluminum substrate with a strain isolator pad (SIP) made of high-temperature nylon fibers that is bonded to the bottom of the tiles and the aluminum with silicone rubber. The bonded area of the SIP is 5 in. by 5 in. on the bottom of the tiles. The aluminum substrate outside the tile/SIP/ substrate bonding area and directly under the tile-to-tile gaps is protected with a high-temperature nylon fiber filler bar that has been heat-treated to withstand higher temperature exposure than SIP. The filler bar is bonded to the aluminum substrate, but it is not bonded to the bottom of the tiles. The filler bar also has a silicone rubber membrane that is applied to the top of the bar to restrict gas flow under the tiles. During the first Shuttle flights, the filler bar experienced higher than expected heating at random locations on the lower side of the fuselage and wing. The excessive heating on the filler bars caused varying degrees of damage - from slight discoloration of the silicone rubber membrane to complete charring of the membrane and high-temperature nylon fiber. The damage to the filler bars occurred on the bottom of the fuselage and wings in geometrically flat regions where the aerodynamic pressure gradient is essentially zero. Ceramic fiber gap fillers are used between tiles in regions where pressure gradients exist, such as near the leading edge of the wings. Gap fillers were not used at these damaged filler-bar locations.

Postflight inspection of the vehicle and its TPS yielded no obvious rationale for the char pattern exhibited in figure 1(b). All tiles were intact and firmly

attached. The tile step and gap measurements were somewhat irregular and often exceeded preflight measurements. The mismatches were as large as 0.120 in. in step height and 0.160 in. in gap width. Attention was focused on the tile-to-tile steps as a possible cause of the filler-bar heating, since local pressure disturbances would be created on the upstream and downstream faces of the stepped tile. A combination of high and low pressures around a tile causes airflow in the tile-to-tile gap, in the SIP, in the filler bar, and in the tile itself. This airflow, at a high energy potential during entry, can cause damage to the filler bar and SIP if they are exposed to these airflow rates over a sufficient period of time. It was not immediately obvious that the observed tile step heights were large enough to cause significant airflow in the tile-to-tile gaps, since they were deeply submerged in the local boundary layer during entry. Boundary-layer thicknesses on the forward part of the wing and fuselage were approximately 2.8 in. and 4 in., respectively, during peak entry heating. An analytical effort was undertaken to define the step heights and gap widths which could produce local conditions capable of charring the filler bars to the extent observed.

This report describes the techniques used and the results of an analytical investigation of excessive heating in the gaps between high-temperature reusable surface insulation (HRSI) tiles of the thermal protection system (TPS) on the lower surface of the fuselage and wings of the Shuttle orbiter. The investigation centered around determining analytically whether the observed postflight tile-to-tile steps and gaps were large enough to generate sufficient hot-gas flows in the gaps to cause damage to the filler bar and SIP. Techniques were developed for estimating the pressure disturbances due to a stepped tile and for calculating the disturbance-induced mass flow rates in the tile-to-tile gaps, the filler bar, the SIP, and the tile itself. These results were used to perform a thermal analysis in the tile-to-tile gap to determine temperature response to the hot-gas flow. Calculations were performed at one location on the fuselage and one location on the left wing, where damaged filler bars were observed on the first flight. The results of the analysis are presented in this report.

SYMBOLS

A_c	cross-sectional area for flow
A_{p_1}	area for pressure loading of SIP
A_{p_2}	area for pressure loading of filler bar
A_s	surface area
A_{σ_1}	area of SIP which is stressed
A_{σ_2}	area of filler bar which is stressed
C_c	Chapman-Rubesin constant
\dot{c}_m	specific heat of solid material
C_p	constant-pressure specific heat of gas
E_1	modulus of elasticity of SIP

E_2	modulus of elasticity of filler bar
F_x	force on tile in x-direction
F_y	force on tile in y-direction
f	friction factor
G	conductance
g_c	unit conversion for acceleration
h	tile step height
h_c	convective heat transfer coefficient
K_p	permeability
K_s	lateral spring constant for SIP
k	thermal conductivity
L	length of duct
L_t	tile thickness
ℓ_1	SIP thickness after tile installation
ℓ_2	filler-bar thickness after tile installation
\bar{M}	local Mach number in boundary layer
M_{loc}	local Mach number outside boundary layer
M_∞	free-stream Mach number
\dot{m}	mass flow rate
\dot{m}_s	mass flow rate when flow is choked
N_{Pr}	Prandtl number
N_{Re}	Reynolds number
N_{St}	Stanton number
p	static pressure
p_{base}	pressure at base of rearward-facing step
p_{ff}	pressure at forward-facing step over tile-to-tile gap
p_{loc}	local static pressure outside boundary layer
p_{peak}	peak static pressure at forward-facing step

P_{plateau} plateau pressure, pressure at constant pressure region
 P_{scale} pressure scaling factor to account for decay of plateau pressure with step height
 P_{sep} static pressure at separation point
 P_{trough} slight pressure drop which occurs ahead of reattachment
 p_{∞} free-stream static pressure
 p_1 average pressure across upstream gap of stepped tile (boundary condition for gap flow calculation)
 p_2 average pressure across downstream gap of stepped tile (boundary condition for gap flow calculation)
 R gas constant
 r recovery factor
 Δs straight-line length from node to node
 T static temperature
 \bar{T} static temperature in boundary layer
 T_{average} average static temperature
 T_{inlet} temperature of gas entering tile-to-tile gap at surface
 T_{loc} local static temperature
 T_0 stagnation temperature
 \bar{T}_0 local stagnation temperature in boundary layer
 T_w wall temperature
 T_{∞} free-stream temperature
 T_1 upstream temperature
 T_2 downstream temperature
 t time
 U_{loc} local velocity outside boundary layer
 u velocity
 \bar{u} local velocity in turbulent boundary layer
 V average velocity

W_f	filler-bar-to-tile gap width
W_{min}	minimum gap between filler bar and tile
W_o	initial gap width
W_t	tile-to-tile gap width
X, Y	Shuttle orbiter coordinates (fig. 1(b))
x	distance from leading edge
$x_{(h = \delta_{eff})}$	length of separation when $h = \delta_{eff}$
x_{ref}	normalized separation length
x_{sep}	length of separation
Δx	longitudinal coordinate measured in downstream direction from point of separation
Δx_{ff}	longitudinal coordinate measured in upstream direction from a forward-facing step
Y_n	homogeneous solutions to energy equation for a compressible laminar boundary layer
Z	compressibility factor
z	distance from wall surface
α	angle of attack
γ	ratio of specific heats
Δ	thermal boundary-layer thickness
δ	velocity boundary-layer thickness
δ_{eff}	effective boundary-layer thickness
δ^*	displacement thickness used when flow is turbulent
η	independent variable
Θ	particle shape factor for flow through porous media
Λ	sweep angle
μ	viscosity
μ_{loc}	local viscosity outside boundary layer
μ_w	viscosity at wall

ξ_{cor}	correlated pressure ratio over extent of separation when step height equals boundary-layer thickness
ξ_p	plateau pressure ratio over separated-flow region
ξ_{pk}	peak or reattachment pressure ratio for a given step height and boundary-layer thickness
ρ	density of gas
ρ_m	density of solid material
τ	shear at wall
ϕ	flow turning angle equivalent to a wedge angle which will produce a pressure rise equal to plateau pressure rise at local Mach number
ψ	stream function

A prime indicates a derivative with respect to an independent variable.

Abbreviations:

B.L.	boundary layer
SIP	strain isolator pad

Mass flow rates:

$\left. \frac{\dot{m}_x}{A_x} \right|_{TH}$ mass flow rate per unit area in x-direction for THERM

$\left. \frac{\dot{m}_z}{A_z} \right|_{TH}$ mass flow rate per unit area in z-direction for THERM

$\left. \frac{\dot{m}_x}{A_x} \right|_{FL}$ mass flow rate per unit area in x-direction from FLOW

$\left. \frac{\dot{m}_z}{A_z} \right|_{FL}$ mass flow rate per unit area in z-direction from FLOW

CALCULATION OF PRESSURE DISTURBANCES DUE TO STEPPED TILES

Two locations on the lower surface of the orbiter, one on the fuselage and one on the left wing (see fig. 1(b)), were selected for analysis, since damaged filler bars were observed in the vicinity and flight pressure and temperature data were available from instrumentation at these locations. The period of interest from the first-flight entry trajectory (ref. 1) of the orbiter is illustrated by the curves

shown in figure 2. The time t equals 0 when the Shuttle orbiter reaches an altitude of 400 000 ft during atmospheric entry. Prior to $t = 500$ sec, gap flow does not contribute significantly in heating the filler bar. Later than 1400 sec, flow velocities have decreased ($M_{\infty} < 4$), so that the available aerodynamic heating is insufficient to damage the filler bar. The plotted symbols in figure 2 represent the trajectory times chosen for calculation of the pressure disturbances caused by a stepped tile. Pressure disturbances for other times in the trajectory were obtained by interpolation.

The pressure and other thermodynamic properties at the edge of the boundary layer were calculated using a tangent-cone approximation, where the half-angle of the cone is equal to the local flow-deflection angle (i.e., the local body-deflection angle plus the angle of attack). The real-gas, axisymmetric, flow-field solution over a cone was obtained using a time-asymptotic numerical procedure with equilibrium thermodynamic properties obtained from reference 2. The tangent-cone approximation has been shown to yield reasonably accurate predictions of the local flow on the windward surface of Shuttle-like configurations. (See ref. 3.) The boundary-layer thicknesses used to estimate the pressure perturbations at the tile-step junctures were calculated by the method described in reference 4.

The principal inviscid and viscous local flow parameters used in this study are presented in figure 3. Even though the flight Mach numbers ranged from approximately 26 down to 5, the corresponding local Mach numbers for both locations on the lower surface of the orbiter were confined to a relatively narrow band from 3.75 down to 2.5. The variations in local static pressure are more dramatic, exhibiting a rapid rise beginning at about 700 sec and peaking near 1200 sec.

The local boundary-layer thicknesses of interest are also presented in figure 3 for the wing and fuselage locations. When the boundary layer is laminar, the boundary-layer thickness is the correlating parameter in the subsequent separated-flow pressure distributions. When the boundary layer is turbulent, the correlating parameter is the displacement thickness. The entry time at which boundary-layer transition from laminar to turbulent occurred was based on flight thermocouple data and was determined to be approximately 1200 sec for the fuselage location and approximately 1100 sec for the wing location. The corresponding boundary-layer thicknesses vary from approximately 0.87 to 4.0 in. on the fuselage and from 0.54 to 1.54 in. on the wing. The measured postflight step heights ranged from -0.099 to 0.12 in. in a fairly random manner; however, in this study the maximum step heights were limited to ± 0.10 in. at the fuselage location and ± 0.06 in. at the wing location. The ratios of step height to boundary-layer thickness were always less than 0.2.

The pressure disturbances around a vertically stepped tile are illustrated in figure 4. The disturbance aft of the downstream face is a reduced pressure region where the flow leaves the surface of the stepped tile and reattaches downstream. The disturbance forward of the upstream face is caused by the separated flow region in front of the step. Both disturbances are directly over gaps between adjacent tiles.

The base pressure on the downstream side of a vertically displaced tile is fairly insensitive to the range of local conditions encountered on the lower surface of the orbiter during entry. A base-pressure correlation for two-dimensional laminar and turbulent flow (ref. 5) employed in this study is presented in figure 5. The correlation is based on the local unit Reynolds number, $\frac{\rho u}{\mu_{loc}}$, which is

then multiplied by the characteristic length $h \left(\frac{h}{\delta_{\text{eff}}} \right)^{2n-2}$. The characteristic length is a function of the boundary-layer thickness δ and the step height h . The exponent n was empirically determined in reference 5 to be 0.9. The base-pressure histories of the fuselage and wing points for the STS-1 entry as determined from the above correlation are presented in figure 6. The two histories are almost identical.

The pressure distributions ahead of the vertically displaced tile are characteristic of a forward-facing step. If the step height is large enough, the pressure distribution assumes a characteristic shape (fig. 7). The key features include the undisturbed local pressure $p_{1\text{loc}}$, a rise associated with boundary-layer lift-off from the surface, p_{sep} , a constant pressure region p_{plateau} , and a slight pressure drop p_{trough} , which generally occurs just ahead of the final pressure rise at reattachment. The plateau pressure also tends to be a reasonable average of the pressure over the extent of separation.

The existence of a plateau pressure for both laminar and turbulent separated boundary layers has been experimentally verified over a wide range of flow conditions and for several triggering mechanisms such as forward-facing steps, flaps deflected into the stream, shock impingement, and compression surfaces. When the local flow conditions are known, the plateau pressure can be predicted fairly accurately with a simple algebraic equation. Several such equations have been empirically developed (e.g., see refs. 6 and 7) and employed with various degrees of success. Figure 8 is a plot of $p_{\text{plateau}}/p_{1\text{loc}}$ versus Mach number from test data reported in reference 8 and experimental results reported in references 6, 7, and 9. The data are directly applicable to the lower surface of the orbiter, since the local Mach number behind the bow shock ranges from 2.5 to 3.75 during the high aerodynamic heating period of entry. The lack of an expression which includes the influence of Reynolds number would normally cause doubt about the range of applicability and overall accuracy. Therefore, a large amount of laminar and turbulent data, including the summaries from two other empirical correlation studies, were used to validate the expression (refs. 6 and 7). The data in the figure fall within a ± 5 -percent accuracy band.

The extent of separation of the flow ahead of a forward-facing step is dependent upon the local flow conditions and the step height. In this study, it was assumed that the dividing streamline over the extent of separation was a straight line, as illustrated in figure 9. The average or plateau pressure ratio over the separated-flow region ξ_p is known, and the expression for the flow turning angle (or equivalent wedge angle) ϕ corresponding to the plateau (or average) pressure rise can be found from the relationships for an oblique shock over a wedge (ref. 10). To account for real-gas effects, an effective ratio of specific heats γ was used in the ideal-gas oblique shock relations at high free-stream Mach numbers. In addition, it is known that the boundary-layer reattachment point always occurs at the top of the forward-facing step. The range of validity of this assumption is dependent upon the nature of the boundary layer (laminar or turbulent) and its thickness relative to the step height. When the boundary layer is laminar, the step height must be equal to or greater than the boundary-layer thickness δ , and when the boundary layer is turbulent, the relation for x_{sep} shown in figure 9 is accurate only if the step height is equal to or greater than 1.5 times the displacement thickness δ^* . These two parameters are designated δ_{eff} in this study. All the step heights of concern in this study were less than δ_{eff} . Therefore, an empirical correlation of extent of separation for laminar and turbulent boundary layers for step heights less than δ_{eff} was established (see fig. 10) from the data in references 11 and 12.

Several experimental studies have been made of the pressure distributions ahead of steps whose heights are fractions of the boundary-layer thickness. (See refs. 11 through 13.) Figures 11(a) through 11(c) present turbulent data for the range of local Mach numbers of interest in this study. It can be seen from these figures that both the plateau pressure and the character of the pressure distribution begin to change significantly for $h/\delta^* < 1.5$, the differences becoming greater with decreasing ratios of step height to boundary-layer thickness. The local Mach number for the data of figure 11(d) is lower than any critical Mach number of this study. It is presented here to illustrate the effect of the limiting condition of very small step heights to boundary-layer thickness ratios. For a given boundary-layer thickness and a set of local flow conditions, the pressure distributions associated with a range of step heights tended to form a closely related set of curves when plotted relative to the separation point rather than the step face. (See ref. 13.) The information seems applicable to the empirical approach employed in this study, except that the present data set covers a wide range of boundary-layer thickness and local flow conditions in addition to the variation in step height. Therefore, in this study the experimental pressure data were normalized by calculated plateau pressures, and the experimental longitudinal separation lengths were normalized by the empirical relations for estimating extent of separation already established in an attempt to correlate the data. Although the data did not correlate exactly, an average pressure distribution for $h = \delta_{eff}$ was identified, as well as functions for perturbing that average to represent the pressure distributions for step heights less than δ_{eff} . (See fig. 12.) The abscissa x_{ref} is simply the normalized separation length relative to the location of the initial pressure rise (i.e., $x_{ref} = x_{sep}/x_{(h = \delta_{eff})}$ where $x_{(h = \delta_{eff})}$ is calculated for $h = \delta_{eff}$

and $x_{ref} = 0$ is coincident with the initial pressure rise). The curve labeled ξ_{cor} is the plateau pressure ratio representing $h = \delta_{eff}$, the pressure distribution which is perturbed to generate the pressure distributions at lesser step heights. The curve P_{scale} represents the decay in plateau pressure ratio with decreasing step height and is also used to scale the basic pressure ratio distribution ξ_{cor} in the pressure direction. The curve ξ_{pk} represents the decay in maximum (or reattachment) pressure ratio with step height.

The validity of the approach is demonstrated through the unswept forward-facing step data displayed in figure 11. The data presented in figure 13 are replotted from figure 11 relative to the separation point corresponding to a step height equal to δ_{eff} (or $h/\delta^* = 1.5$ in this case). The separation point is at $\Delta x/\delta^* = 0$. A functional relationship between the family of experimental curves is quite evident and consistent over the range of local Mach numbers of interest. When the correlations developed in this study are applied to the data, the major discrepancy seems to be a slight underprediction of the extent of separation which is amplified at lower Mach numbers. However, the basic pressure distribution and the envelope of peak pressures seem adequate except at the lowest Mach number, at which both peak and distributed pressures are underpredicted.

The data available to establish correlations for the effects of sweep on forward-facing steps were extremely limited. Reference 14 is a fairly comprehensive study of sweep effects for two step heights at two local Mach numbers (1.61 and 2.01) on turbulent boundary-layer separation. Even though there was an indication of a slight effect of Mach number on the results due to sweep, the two available Mach numbers were not adequate for a correlation study. The data for the higher Mach number were used because Mach 2.01 is closer to the Mach numbers of interest in this study (fig. 14).

Because of the limited parametric experimental data, an approach was developed based on the data for a local Mach number of 2.01 and the step size corresponding to δ_{eff} (i.e., $h/\delta^* = 1.5$). It is assumed that the effects of reduced step heights are adequately represented by the previous correlations and that the effects of sweep would be adequately represented by simple ratios of swept-to-unswept pressure distributions at $M_{\text{loc}} = 2.01$ and $h/\delta^* = 1.5$. The ratios for the four available sweep angles ($\Lambda = 0^\circ, 15^\circ, 30^\circ, \text{ and } 45^\circ$) are presented in figure 15. The ratio for $\Lambda = 0^\circ$ is, of course, equal to one and is shown only for reference. The decrease in pressure at $\Lambda = 15^\circ$ is nearly constant and is small over the extent of separation. The major difference (or reduction) in pressure for the higher sweep angles occurs nearest the face of the step. The 30-percent reduction in pressure for $\Lambda = 30^\circ$ is nearly constant over the 50 percent of the separation length closest to the face of the step. The reduction in pressure for the 45° -swept step is the primary condition of interest in this study, because the TPS tile pattern relative to the local flow direction was designed to be as near to a 45° sweep as possible. The percentage reduction in pressure at 45° sweep is quite large. It varies continuously across the length of separation and reaches a minimum value of approximately 25 percent at 20 percent of the separation-length location in front of the step.

The effects of these pressure reduction ratios on the unswept pressure distributions are illustrated in figure 16 for the case when the step height is equal to δ_{eff} . The basic pressure distribution E_{cor} is shown in figure 12. The resulting distributions look reasonable, with the possible exception of the 45° sweep. However, all the basic elements of the characteristic separated-flow pressure distribution shown in figure 7 are retained in each distribution, with the 45° -sweep distribution being more representative of the character noted for large step sizes at lower Mach numbers.

INCOMPRESSIBLE STEADY FLOW MODEL

An existing incompressible steady flow model, originally developed for ascent loads analysis for the Shuttle thermal protection system (TPS), was modified to include compressibility effects in the gap. The incompressible steady flow model represents an array of nine tiles. The Martin Interactive Thermal Analysis System (MITAS), a general purpose finite-difference heat transfer program, was used for computer modeling of airflow through the TPS system. (See ref. 15.) The MITAS program can be used for internal incompressible flow because of the similarity between internal incompressible flow and heat transfer equations.

The input to the MITAS program for steady-state flow is node and conductor definition, or, in other words, an electrical analog representation of the geometric configuration. All modeling was done in three dimensions to obtain tile, SIP, and filler-bar internal pressures and tile-to-tile gap pressures from given surface pressure boundary conditions.

A single-tile three-dimensional model was developed first. A sketch showing the flow paths through a single tile is shown in figure 17. The ceramic coating, which covers most of the tile surface, is considered impermeable in this study. The flow through the silicone-rubber bond line on the bottom of the tile is considered to be insignificant. Thus, areas where flow can enter or leave a tile are the terminator gap area and the 1/2-in. wide unbonded area on the bottom outer edge of the tile. Flow can enter or leave the SIP through the unbonded area on the bottom of the tile or through the gap between the tile bottom and the filler bar. The connections to the surface through which all internal flow enters or leaves are the gaps between the

tiles. The dimensions of the single-tile model are 6 in. by 6 in., and the thicknesses of the tile and SIP are variable. The nodal arrangement for the single tile, also called the subject tile in the nine-tile model, is shown in figures 18 through 20. Figure 18 shows nodes 61 through 96, which are the nodes inside the tile at the surface. Figure 19 shows nodes 25 through 60 (inside the tile at the bond-line plane), nodes G1 through G24 (at the bottom of the gap between tiles), and nodes B201 through B224 (the boundary nodes for the internal flow, located at the surface over the gap between tiles). Figure 20 shows nodes 97 through 132, which are in the SIP. Conductors were defined to connect the nodes in three dimensions. Examples of nodes in the x-y plane that were connected by conductors would be 61 to 62, 61 to 67, 25 to 26, 25 to 31, 97 to 98, and 97 to 103. Examples of nodes that were connected by conductors for flow in the z-direction would be 61 to 25, 62 to 26, 67 to 31, 68 to 32, 25 to 97, 26 to 98, 31 to 103, and 32 to 104. There are two parallel flow paths from the bottom of the gap to the bottom of the tile: one flow path through the edge of the tile and one flow path under the edge of the tile between the tile and filler bar (fig. 17, view A). These flow paths are represented in figure 19 by electrical resistance symbols connecting gap nodes to tile bond-line nodes, such as nodes G2 and 26. Figure 19 also shows the conductors connecting surface boundary nodes to nodes at the bottom of the gap, such as the conductor shown connecting boundary node B202 to gap node G2.

Using the single-tile model as a guide, an array of nine tiles was developed by adding eight more similar tiles to the single-tile model. Flow from one tile to another is through the filler bar and through the gaps between tiles. The overall pattern of tiles from which the multitile model was developed is shown in figure 21. The nine tiles in the model are shown numbered 1 through 9. The locations of the nodes in the multitile array are shown in figures 22 through 24. Figure 22 shows nodes inside the tile at the surface for each of the nine tiles. Figure 23 shows nodes at the tile bond line and at the surface and bottom of the adjacent gaps for each of the tiles. Figure 24 shows nodes in the SIP for each of the tiles.

The flow conductance modeling for the nine-tile flow model is described in the paragraphs which follow. The general categories of conductance values to be determined were tile material, SIP material, gap between tiles, tile terminator gap, gap between tile and filler bar, and gap between filler bar and SIP.

The conductance for flow through tile and SIP was based on flow through porous media. The conductance for flow through porous media as used in the analysis is determined as follows:

$$\text{Conductance} = \frac{K_p \rho A_c}{\mu \Delta s} \quad (1)$$

The flow through the tile in the terminator gap area is flow through porous media but due to the coarseness of the model it was necessary to use an entrance effect factor on this conductance to account for the local geometry.

The conductance for flow through the gap between tiles and the gap between tile and filler bar resembles flow between parallel walls. The equations for mass flow

and conductance based on laminar flow between parallel walls as used in the analysis are as follows:

$$\dot{m} = - \frac{1}{12} \frac{\rho w_t^2 A_c}{\mu} \frac{dp}{ds} \quad (2)$$

$$\text{Conductance} = \frac{1}{12} \frac{\rho w_t^2 A_c}{\mu \Delta s} \quad (3)$$

where

$$\frac{dp}{ds} = \text{Pressure gradient}$$

$$\Delta s = \text{Distance from center of one node to the next}$$

The gap size and resulting conductance for flow through the gap between tiles was calculated iteratively for tiles which had significant side pressure forces on them. These side forces result from the surface pressure gradient. Figure 25 shows the tile-to-tile gaps in the global model which were varied. The calculations of tile deflection were only made on the subject tile (tile 9). The force on the subject tile was obtained by integration of the gap pressures on the sides of the tile to get a resultant side force in the x- and y-directions. Neglecting rotation of the tile about the z-axis, the translational motion of the subject tile was then obtained from a spring representation of the SIP according to the following equations:

$$\Delta x_s = F_x / K_s \quad (4)$$

$$\Delta y_s = F_y / K_s \quad (5)$$

where

$$\Delta x_s = \text{Subject tile x-deflection}$$

$$F_x = \text{Force in x-direction}$$

$$\Delta y_s = \text{Subject tile y-deflection}$$

F_y = Force in y-direction

K_s = Lateral spring constant for SIP

The SIP lateral spring constant was 110 lb/in. (ref. 16). The gaps which change are shown in figure 25. The shaded gaps close and were decreased from the initial value by the tile deflection. The cross-hatched gaps open and were increased from the initial value by the tile deflection multiplied by a factor to account for deflection of the adjacent tile. The maximum gap measured after the first Shuttle flight, 0.126 in., was used to set this factor. This factor was 1.55 so that the gap width for the opening gaps would be 0.126 in. at the maximum tile deflection. A condition which takes priority is that the tile-to-tile gap must always be greater than the effective gap which exists when the two smooth surfaces are in contact. These gaps and the resulting flow conductance based on laminar flow between parallel walls were changed based on the calculated pressures until the calculated gap sizes converged.

The gap size and resulting conductance for flow through the gap between tile and filler bar was calculated iteratively for all tiles in the global model. The size of this gap is determined by the relative normal deflection between the bottom surface of the tile and filler bar, and also by the silicone-rubber membrane effect. The size of this gap is determined in a manner similar to the tile-to-tile gap. The dimensions and deflections which influence this gap are shown in figure 26. The equation used to compute tile deflection is

$$\Delta l_1 = \frac{\Delta p_1}{E_1} \frac{A_{p_1}}{A_{\sigma_1}} l_1 \quad (6)$$

where

Δp_1 = Pressure difference between tile top surface and SIP

A_{p_1} = Area which Δp_1 acts on, loading SIP

A_{σ_1} = Area of SIP which is stressed

l_1 = SIP thickness after tile installation

E_1 = Modulus of elasticity of SIP

The filler-bar deflection is due to the pressure differential across the silicone-rubber surface membrane and is defined by

$$\Delta l_2 = \frac{\Delta p_2}{E_2} \frac{A_{P_2}}{A_{\sigma_2}} l_2 \quad (7)$$

where

Δp_2 = Pressure difference between tile-to-tile gap and filler bar

A_{P_2} = Area of filler bar which Δp_2 acts on

A_{σ_2} = Area of filler bar which is stressed

l_2 = Filler bar thickness after tile installation

E_2 = Modulus of elasticity of filler bar

The desired filler-bar-to-tile gap width is obtained based on the following equation:

$$W_f = \Delta l_2 - \Delta l_1 + W_o \quad (8)$$

where W_o is the initial gap width. The minimum limiting value for W_f is defined as W_{min} , the effective gap width which exists when the tile bottom touches the filler bar (FB). The final condition which was considered in the determination of the gap width was the silicone-rubber membrane effect. This effect causes a check valve action which restricts flow out of the SIP/FB more than it restricts flow into the SIP/FB. It was assumed that this membrane effect would dominate the gap-size determination. So for this analysis, it was adequate to assume that the gap height for flow out of the SIP/FB would be W_{min} and the gap width for flow into the SIP/FB would be as calculated from the above equation. The tile-to-filler-bar gaps and the resulting flow conductance based on laminar flow between parallel walls were also changed based on the calculated pressures until the calculated gaps converged.

The flow through the gap between the SIP and filler bar was modeled as flow through a slot. The equations describing this type of flow are

$$\dot{m} = C_D A_c (2\rho g_c \Delta p)^{1/2} \quad (9)$$

$$\text{Conductance} = C_D A_c \left(\frac{2\rho g_c}{\Delta p} \right)^{1/2} \quad (10)$$

The discharge coefficient C_D for this slot was assumed to be 0.5. The flow cross-sectional area for tiles with significant side deflections is varied consistent with the side deflections calculated for the tile-to-tile gap deflections mentioned previously.

STEADY FLOW MODEL WITH COMPRESSIBILITY

During ascent, the gap flow was assumed to be incompressible. However, during entry the pressure differences from forward-facing and rearward-facing steps were found to be large enough that compressibility effects would be important in the tile-to-tile gaps. Consequently, it was necessary to modify the existing flow model to account for this.

The modification consisted of changing the tile-to-tile gap flow calculation from one of laminar incompressible flow to one of compressible flow, either laminar or transitional. The modeling of compressible flow in the gap was accomplished under the assumption of compressible internal flow of an ideal gas with constant cross-sectional area and frictional effects. This type of flow is often referred to as Fanno Line flow. The approach taken was to solve the appropriate equations of conservation of mass, momentum, and energy to obtain an equation for mass flow rate as a function of upstream pressure and temperature and downstream pressure. An equation of this form can be represented in the MITAS program as follows:

$$\dot{m} = f(p_1, T_1, p_2) \quad (11)$$

$$G = \dot{m} / (p_1 - p_2) \quad (12)$$

where

\dot{m} = Mass flow rate

p_1 = Upstream pressure

p_2 = Downstream pressure

T_1 = Upstream temperature

G = Conductance

The equations used to represent this constant-area internal flow are

Energy equation:

$$T = T_o - \frac{\dot{m}^2}{2\rho^2 A_c^2 C_p} \quad (13)$$

Momentum equation:

$$-dp - \frac{\tau}{A_c} A_s = \rho V(dV) \quad (14)$$

Continuity:

$$\dot{m} = \rho A_c V \quad (15)$$

Ideal-gas law:

$$p = \rho RT \quad (16)$$

where T_o is the stagnation temperature (assumed to be constant). The difference between these equations and the equations for incompressible flow is that for incompressible flow dp and dV are zero and the ideal-gas law does not apply.

For the case of laminar compressible flow, the momentum equation becomes

$$-dp - \frac{12\dot{m}\mu}{\rho A_c W_t^2} dx = \rho V(dV) \quad (17)$$

This equation was solved simultaneously with the energy equation, continuity equation, and ideal-gas law to obtain an equation for mass flow as a function of p_1 , p_2 , T_1 , and T_2 . Initially, T_2 is assumed to be equal to T_1 . The resulting equation for mass flow rate is

$$\dot{m} = [-b + (b^2 + 4A_c)^{1/2}] / 2a \quad (18)$$

where

$$a = \left[\left(\frac{1 + \gamma}{\gamma} \right) \frac{\ln(\rho_1/\rho_2)}{2A_c^2} - \left(\frac{\gamma - 1}{\gamma} \right) \frac{\rho_1^2 - \rho_2^2}{4\rho_1^2 A_c^2} \right]$$

$$b = 12\mu L / (A_c w_t^2)$$

$$c = (0.5)RT_1(\rho_1^2 - \rho_2^2)$$

An approximate form of the energy equation is used to adjust the initial estimate of T_2 . After differentiating equation (15) to obtain

$$dT = \frac{\dot{m}^2}{\rho^3 A_c^2 C_p} d\rho \quad (19)$$

and making the approximations

$$dT \approx T_2 - T_1$$

$$d\rho \approx \rho_2 - \rho_1$$

$$\rho \approx \rho_1$$

the following energy equation as used in the analysis is obtained:

$$T_2 = T_1 + \frac{\dot{m}^2 (\rho_2 - \rho_1)}{\rho_1^3 A_c^2 C_p} \quad (20)$$

where

$$\rho_1 = p_1/RT_1$$

$$\rho_2 = p_2/RT_1$$

The mass flow is then recomputed using this improved value of T_2 .

For the case of compressible transition flow, the momentum equation was obtained from a plot of friction factor found in reference 17. The range of transition flow was estimated to be $2500 < N_{Re} < 6000$ for flow between parallel plates, or channel flow as it is often called. The Reynolds number as used here is defined to be

$$N_{Re} = \frac{2\rho V W_t}{\mu} = \frac{2W_t \dot{m}}{\mu A_c} \quad (21)$$

An empirical equation for friction factor was used to represent the transition region. The form of the equation was

$$\frac{f}{4} = aN_{Re}^2 + b \quad (22)$$

where

$$f = \frac{8\tau}{\rho V^2} \quad (23)$$

The values of the constants a and b were obtained by imposing two conditions for a Reynolds number of 6000. First, the value of $f/4$ must be 0.009. Second, the slope of the curve represented by equation (22) must equal the slope of the curve for the equation for turbulent friction factor. The equation for turbulent friction factor, as given in reference 18, is

$$\frac{f}{4} = \frac{0.08}{N_{Re}^{1/4}} \quad (24)$$

The conditions to be met at a Reynolds number of 6000 are

$$0.009 = aN_{Re}^2 + b \quad (25)$$

$$8aN_{Re} = -0.08N_{Re}^{-5/4} \quad (26)$$

The values of the constants a and b are obtained from these two conditions, and the resulting empirical equation is

$$\frac{f}{4} = (-3.156 \times 10^{-11})N_{Re}^2 + 0.01014 \quad (2500 < N_{Re} < 6000) \quad (27)$$

This expression for $f/4$ was then substituted into the momentum equation to obtain a transition momentum equation as follows:

$$\frac{1}{8} f \rho V^2 = \frac{1}{8} f \frac{\dot{m}^2}{\rho A_c^2} \quad (28)$$

Equation (28) was then solved simultaneously with the energy equation, continuity equation, and ideal-gas law, as was done for the laminar flow case, to obtain mass flow as a function of p_1 , p_2 , T_1 , and T_2 . This equation for mass flow was solved in two iterations as in the laminar-flow case. The equation for mass flow in the transition region as described above was

$$a\dot{m}^4 + b\dot{m}^2 + c = 0 \quad (29)$$

and was solved for \dot{m} to obtain the equation

$$\dot{m} = \left\{ \left[-b + (b^2 - 4A_c) \right]^{1/2} / 2a \right\}^{1/2} \quad (30)$$

where

$$a = (-3.156 \times 10^{-11}) \frac{4W_t L}{\mu^2 A_c^4}$$

$$b = \frac{R \ln(\rho_2/\rho_1)}{2A_c^2 C_p} - \frac{\ln(\rho_2/\rho_1)}{A_c^2} + \frac{R(\rho_2^2 - \rho_1^2)}{4\rho_1^2 A_c^2 C_p} + 0.002536 \frac{4L}{A_c^2 W_t}$$

$$c = \frac{g_c RT}{2} (\rho_2^2 - \rho_1^2)$$

The Reynolds number based on twice the gap width was always less than 6000, so it was not necessary to include turbulent-flow equations.

The mass flow was limited by sonic velocity as indicated by the expressions

$$\dot{m}_s = \rho_2 A_c (\gamma RT_2)^{1/2} \quad (31)$$

$$\dot{m} < \dot{m}_s \quad (32)$$

where

\dot{m}_s = Mass flow rate for sonic velocity

γ = Ratio of specific heats

TRANSIENT THERMAL MODEL

The thermal model was developed to represent the insulation system and aluminum structure in the vicinity of a tile-to-tile gap. This modeling was done using the MITAS program. The region modeled was half the length of a tile-to-tile gap. The width of the model from the center of the gap into each adjacent tile could be set between 1.033 in. and 1.405 in. to change the size of the model and the location of nodes and boundaries when necessary. The width of the model was adequate, because the heat-transfer rates in the direction away from the gap are small at the boundary. Half the length of the tile-to-tile gap (3 in.) is adequate if the mass flow rate down the gap being modeled is much greater than any flow into the gap being modeled from the adjacent gap at either edge of the model. The top and side view of the

model are shown in figure 27. Figure 28 is an enlarged side view of the model. The parts of the tile system which were modeled were the tile, tile coating, SIP, aluminum substrate, filler bar, filler-bar surface membrane, and the flowing gas in the gaps, SIP, and filler bar. The types of heat transfer considered were conduction, radiation, mass transfer, and convection. Conduction was considered in the tile, tile coating, SIP, filler bar, silicone-rubber membrane, and aluminum substrate. Radiation was considered on the tile surface and in the gap between tiles. Mass transfer was considered in the gaps, through the filler bar and SIP, and into or out of the tile. Convection was considered between the gas in the tile-to-tile gap and the side wall of the tile, between the gas in the gap and the filler-bar membrane, between the gas in the filler bar and the filler-bar membrane, and between the gas in the SIP and the bottom of the tile. The input to the thermal program from the flow program was the mass flow rate per unit area at points where mass-transfer heating was included in the thermal model. For the fuselage location, the boundary conditions for the thermal model were a specified temperature of the gas entering the gap and a tile surface heat flux versus time, from which surface temperature was calculated. For the wing location, tile surface temperature versus time was used for a boundary condition rather than surface heat flux versus time.

The numbering system used in the model is shown in figures 27 and 28. Shown in figure 28 are the node centers which are in the same plane. There are three planes like this shown in figure 27 as the 2000-, 3000-, and 4000-series locations, with the numbers of the nodes in figure 28 added to 2000, 3000, or 4000 for the three planes (for example, 2152, 3152, and 4152). The tile surface is node number 101. It is the same for all three planes, and therefore does not have the thousand series added to it. The input dimensions of the model are shown in figure 28 as R10, R11, R12, R13, R20, R21, R22, R23, and R24. The width of tile nodes 2212, 2222, 2232, 2242, and 2252 are $R12/15$, $2(R12/15)$, $4(R12/15)$, $8(R12/15)$, and $16(R12/15)$, respectively. The width of all of the tile nodes are related to R12 with this same progression. When the 2000- or 4000-series tile nodes are bounded by a tile corner, the nodes and conductors in the tile in that plane are changed to represent a boundary as shown in figure 27.

Conduction and Radiation

Conduction and radiation are represented in the model in the usual way for a finite-difference program. Conduction between nodes is represented as kA_c/L . The thermal conductivity k is a function of temperature, except in the HRSI insulation tiles where it is a function of temperature and pressure. The aluminum substrate has 1000- and 5000-series nodes included in the model for edge continuity. These nodes are the same size as the corresponding 2000- and 4000-series nodes. Radiation from the surface of the tile is represented by a radiation conductor between the surface and a node at the deep-space temperature, -460°F . The only parameter which influences this radiation from the surface is the emissivity, which was input as 0.85. Radiation in the gap is considered to be radiation in an enclosure formed by the sides of the tiles, the filler-bar membrane, a surface at the top of the gap which represents deep space, and surfaces at the edge of the gap to bound the model. Figure 29 shows the gap radiation model. Node 8001 is the top boundary and the 7000- and 8000-series nodes are the side boundaries. View factors for elements forming a right angle and having a common edge are calculated using the exact method (ref. 19). Others were calculated using an LaRC view factor program (ref. 20).

Mass Transfer

Mass-transfer heating was of major significance only in the tile-to-tile gap, although it was considered in the filler bar, SIP, and through the bottom corner of the tile where the porous tile is not coated. Mass transfer in the thermal model depends on the mass flows which are calculated by the flow model. The mass transfer is modeled using the fluid flow conductor capability of MITAS. The conductance is the product of mass flow between the nodes and specific heat ($\dot{m}C_p$). The specific heat of the gas is considered to be a function of temperature.

The actual values of mass flow are obtained by multiplying the mass flow per unit area, which is based on input, by the cross-sectional area for flow. For the case of flow in the gap, there is only one mass flow per unit area down the gap and one flow along the gap. These flows are calculated by the flow model, which must be used to estimate the mass flow rates for a finer grid of conductors in the thermal model. Figure 30 shows the method used to obtain the x- and z-components of mass flow per unit area at locations in the gap as needed in the thermal model. Mass-transfer conductors used the appropriate x- or z-components of mass flow per unit area directly, and convective conductors used the resultant mass flow per unit area at the location in the gap of the conductor being modeled. The mass flows of the two models are related as shown in the following equations (see fig. 30):

$$\left. \frac{\dot{m}_{x,i}}{A_{x,i}} \right|_{TH} = \left. \frac{\dot{m}_x}{A_x} \right|_{FL} \quad (33)$$

$$\left. \frac{\dot{m}_{z,i}}{A_{z,i}} \right|_{TH} = \left[\left. \frac{\dot{m}_z}{A_z} \right|_{FL} (L_t - z)/L_t \right] \quad (34)$$

$$\left(\left. \frac{\dot{m}_{x,i}}{A_{x,i}} \right|_{TH_{out}} - \left. \frac{\dot{m}_{x,i}}{A_{x,i}} \right|_{TH_{in}} \right) = \left(\left. \frac{\dot{m}_{z,i}}{A_{z,i}} \right|_{TH_{in}} - \left. \frac{\dot{m}_{z,i}}{A_{z,i}} \right|_{TH_{out}} \right) \quad (35)$$

$$= \left[\left. \frac{\dot{m}_z}{A_z} \right|_{FL} (z_{out} - z_{in})/L_t \right] \quad (36)$$

where the subscript i refers to node i in the thermal model, and the subscripts in and out refer to flow in and out of node i in the thermal model.

The temperature of gas entering the gap from the side is set equal to the temperature of the gas in the gap in the center of the thermal model at the same depth from the surface. This assumption was made because the flow down the gap at the forward-facing step is much larger than the flow entering the gap from the side. The

gas at the center of the tile-to-tile gap in the thermal model is the 3000 series. The temperature of the gas entering the top of the gap is referred to as the gas inlet temperature. Figure 31 shows how mass transfer in the gap is modeled. The gas inlet temperature is calculated using the flow conditions at the surface and is discussed subsequently.

Convection

Convection conductors are represented in the model as the product of heat transfer coefficient h_c and surface area. Convection in the SIP and filler bar is modeled as forced convection through packed beds. For Reynolds numbers less than 50, the following equation (ref. 21) for the heat-transfer coefficient applies:

$$\left(\frac{h_c}{C_m \rho_m u} \right) N_{Pr}^{2/3} = (0.91 N_{Re}^{-0.51}) \Theta \quad (37)$$

where

$$N_{Re} = \frac{\rho u}{a \mu \Theta}$$

A value of 0.91 was the particle shape factor assumed for Θ , which resulted from assuming cylindrical fibers. The parameter a is the solid-particle surface area per unit bed volume. For the gaps, the convection heat-transfer coefficient was calculated as follows assuming Reynolds analogy:

$$N_{St} N_{Pr}^{2/3} = f/8 \quad (38)$$

where

$$N_{St} = \frac{h_c}{\rho C_p u}$$

The friction factor is determined as follows by assuming fully developed laminar flow between flat plates:

$$f = \frac{24}{N_{Re}} \quad (39)$$

where the Reynolds number is based on hydraulic diameter (ref. 22).

Surface Temperature

The tile surface boundary condition was either a specified heat flux or a specified surface temperature. The specified heat-flux condition was obtained from a table in the program of surface heat flux versus time and surface temperature. These data, used for the fuselage location, are shown in table I. The temperature of node 101, the tile surface, was calculated versus time for the specified heat-flux condition. The specified surface temperature condition for the wing location was a table of temperature versus time in the program from which the temperature of node 101 was obtained. Wing surface temperature versus time is shown in table II.

Gas Inlet Temperature

The gas inlet temperature is obtained by considering the flow to be isentropically compressed from the local pressure to the computed pressure on the forward face of the stepped tile:

$$\frac{P_{ff}}{P_{loc}} = \left(\frac{T_{inlet}}{T_{average}} \right)^{\gamma/(\gamma-1)} \quad (40)$$

The gas average static temperature $T_{average}$ is obtained from a mass flow weighted average of the boundary-layer static temperature from the tile surface up to the tile step height h :

$$T_{average} = \frac{\int_0^h \rho u T \, dz}{\int_0^h \rho u \, dz} \quad (41)$$

In order to calculate the average static temperature, velocity and temperature distributions in both compressible laminar and turbulent boundary layers must be obtained. For the compressible laminar boundary layer, a technique developed by Chapman and Rubesin (ref. 23) was used to determine the velocity and temperature distributions at specific times during entry. This technique approximates the temperature dependence of the viscosity of air with the following linear relationship:

$$\frac{\mu_w}{\mu_{loc}} = C \frac{T_w}{T_{loc}} \quad (42)$$

The constant C is evaluated for each set of wall and free-stream temperatures under consideration. Using the viscosity relationship shown in equation (42) allows the boundary-layer momentum and energy equations to be independent of each other so that

they can be solved separately. By using a transformation that replaces the independent variable y with the stream function ψ , by nondimensionalizing all variables, and by applying appropriate boundary conditions, the momentum equation for a compressible laminar boundary layer can be satisfied with the Blasius solution. The energy equation can be written as a linear, second-order differential equation. The tile outer-surface temperature was considered to be uniform in the filler-bar analysis. The solution for the temperature distribution in the boundary layer is

$$\frac{T}{T_{loc}} = 1 + \frac{\gamma - 1}{2} M_{loc}^2 (r(\eta) - r(0) Y_0(\eta)) + Y_0(\eta) \left(\frac{T_w}{T_{loc}} - 1 \right) \quad (43)$$

where $r(\eta)$ is the temperature recovery factor and $Y_0(\eta)$ is the function for $n = 0$ from the set of temperature distribution functions $Y_n(\eta)$ that result from the solution of the homogeneous part of the energy equation in the η - or z -direction. The functions $Y_n(\eta)$ are obtained by integrating the equation

$$Y_n'' + N_{Pr} f Y_n' - 2n N_{Pr} f' Y_n \quad (44)$$

The recovery factor is

$$r(\eta) = \frac{N_{Pr}}{2} \int_{\eta}^{\infty} [f''(\zeta)] N_{Pr} \int_0^{\zeta} [f''(\beta)]^{(2-N_{Pr})} d\beta d\zeta \quad (45)$$

and is derived from a particular solution of the energy equation. The symbols β and ζ are arbitrary variables of integration. The term f'' is one of the Blasius functions. The independent variable η is related to z in the form

$$\frac{z}{2} \left(\frac{\rho U_{loc}}{\mu_{loc} X C_c} \right)^{1/2} = \eta + \frac{\gamma - 1}{2} M_{loc}^2 \bar{r}(\eta) + \left[\frac{T_w}{T_{loc}} - \left(1 + r(0) \frac{\gamma - 1}{2} M_{loc}^2 \right) \right] \bar{Y}_0(\eta) \quad (46)$$

where

$$\bar{r}(\eta) = \int_0^{\eta} r(\eta) d\eta$$

$$\bar{Y}_0(\eta) = \int_0^\eta Y_0(\eta) d\eta$$

Figure 32 shows the variations of the Blasius functions, the recovery factor and integrated recovery factor, and the temperature distribution functions $Y(\eta)$ with the independent variable η . Figure 33 shows the velocity and temperature distribution in the laminar boundary layer on the Shuttle lower fuselage ($X = 750$ in., $Y = -75$ in.) for a local Mach number of 2.83.

Velocity and temperature distributions in the turbulent boundary layer were approximated by using the 1/7-power profiles:

$$\frac{\bar{u}}{U_{loc}} = \left(\frac{z}{\delta}\right)^{1/7} \quad (47)$$

$$\frac{\bar{T}_o - T_w}{T_o - T_w} = \left(\frac{z}{\Delta}\right)^{1/7} \quad (48)$$

where \bar{u} is the local velocity and \bar{T}_o is the stagnation temperature in the boundary layer. The thermal boundary layer thickness Δ was assumed to be equal to the velocity boundary layer thickness in the filler-bar analysis:

$$\Delta = \delta \quad (49)$$

The perfect-gas relationships between the stagnation and static temperatures in the local stream and boundary layer were

$$T_o = T \left[1 + \left(\frac{\gamma - 1}{2}\right) M_{loc}^2 \right] \quad (50)$$

$$\bar{T}_o = \bar{T} \left[1 + \left(\frac{\gamma - 1}{2}\right) \bar{M}^2 \right] \quad (51)$$

where

$$M_{loc} = U_{loc} / (\gamma RT)^{1/2}$$

$$\bar{M} = \bar{u} / (\gamma R \bar{T})^{1/2}$$

In order to define the static-temperature distribution in the boundary layer, equations (50) and (51) were used to obtain the following equation (ref. 24):

$$\frac{T}{T_w} = \frac{T_w}{T} \left[1 + \left(\frac{T_o}{T_w} - 1 \right) \left(\frac{z}{\delta} \right)^{1/7} - \left(\frac{\gamma - 1}{2} \right) M_{loc}^2 \left(\frac{T}{T_w} \right) \left(\frac{z}{\delta} \right)^{2/7} \right] \quad (52)$$

With these definitions of velocity and temperature distributions for laminar and turbulent boundary layers, the inlet gas temperature can be calculated. The density variation through the boundary layer is determined using

$$\rho = \frac{P_{loc}}{ZRT} \quad (53)$$

where Z is the compressibility factor for air. The usual boundary-layer assumption that the static pressure in the boundary layer is the same as the local static pressure is used in the calculation.

FLOW-TO-THERMAL MODEL INTERFACE

Interfacing the flow and thermal models required processing the mass flow rates calculated by the flow model to obtain the mass flow per unit area needed for the thermal model. The flow model represents nine tiles, while the thermal model represents only 3 in. of gap and part of the two tiles adjacent to the gap. Interfacing between the programs is accomplished using two subprograms. The first subprogram selects mass flow data from flow model results which apply to the given location of the smaller thermal model. The second subprogram processes the selected mass flow data to obtain mass flow per unit area for the thermal model (fig. 34). The input to the mass flow selection subprogram is information to identify the location of interest, and the output was the required mass flows for this location. The inputs to the mass flow processing subprogram are the selected mass flows and dimensions which are common to the flow and thermal models. The output of the mass flow processing subprogram is the mass flow per unit area for conductors in the thermal model which require mass flow information to represent convection or mass-transfer type of heat transfer.

The flow model represents steady flow at a point in time, while the thermal model represents a transient which spans a time interval. The thermal model requires flow information as a function of time, so two runs of the flow model were required for one run of the thermal model. One run of the flow model is made for the starting point of the time interval, and another run is made for the stopping point. Mass flow information is transferred to the thermal model for each of the two time points. The thermal model then uses the mass flows per unit area for these two points in time to obtain mass flows by linear interpolation at any time in the time interval and to obtain mass flows for later times by extrapolation. The flow run for the time point at the end of the time interval requires temperature information which must be estimated and later checked against the temperature results of the thermal model at the end of the time interval.

Figure 35 is a flow chart of the tile flow and thermal analysis. Runs of the flow program are indicated by FLOW, and runs of the thermal analysis program are indicated by THERM. THERM uses the steady-state mass flows and other temperature boundary conditions to calculate the transient thermal response of the gap region. The input temperatures are known for the run of FLOW at the start of a time interval, but the input temperatures for the run of FLOW at the end of a time interval must be estimated and later checked against temperatures which are calculated by THERM. If the input temperatures estimated for the last run of FLOW are more than 5 percent different from the calculated temperatures, the last run of FLOW must be repeated with new estimated input temperatures, and the last run of THERM must also be repeated using the new set of mass flows calculated by FLOW. The thermal model THERM calculates for two time intervals per run. The results of the first time interval are saved, and the results of the second time interval are used to estimate input temperatures for the next run of FLOW.

The desired location of the thermal model in the tile array to examine filler-bar charring was the location where the highest gap temperatures would occur. High gap temperatures are caused by large mass flow rates down the gap, and therefore the thermal model location in the tile array was the part of the gap which had the highest calculated mass flow rate down the gap. The calculated mass flow rates down the gap for runs of the flow model with a stepped tile were always greatest at the same gap location, so this location was chosen for the thermal model. The location of the thermal model thus determined is shown in figure 36. The necessary condition for accuracy of the thermal model, that the mass flow rate down the gap be much greater than the mass flow rate along the gap, was satisfied at this location.

CALCULATED FILLER-BAR TEMPERATURES DUE TO STEPPED TILES

A thermal analysis was performed for two locations on the bottom surface of the Shuttle orbiter for the STS-1 entry conditions. The two locations were a fuselage point (500 in. from the nose) at orbiter coordinates of $X = 750$, $Y = -75$, and a wing point (105 in. aft of the local leading edge) at $X = 1220$, $Y = 275$ (fig. 1(b)). These two points were selected because (1) filler-bar charring occurred, (2) they are in regions where the local aerodynamic surface flow conditions could be computed, and (3) they represent two extremes in terms of location relative to the leading edge. Table III shows the extremes in step and gap dimensions of STS-1 postflight ground measurements made at damaged filler-bar locations. The table also shows definitions of filler-bar charring categories. This information was supplied by the Johnson Space Center (JSC). The gap heating analysis model was based upon the STS-1 entry trajectory for various step heights and nominal gaps, starting from an initial temperature of 40°F.

Results were obtained for tile steps of 0.1 in. and 0.04 in. at the fuselage location. Figure 37 shows how the ratio of step height to boundary-layer thickness h/δ varies at the fuselage location $X = 750$, $Y = -75$ for a constant step height of 0.1 in. The thickness of the tile at this location was 1.41 in., and the initial tile-to-tile gap size was 0.05 in. Figure 38 shows the forward and aft face pressures for the 0.1-in. stepped tile along with the local static pressure used in the analysis. Figure 39 shows the temperature response of the filler bar at the fuselage location, along with the local static gas temperature, the inlet gas temperature, and the tile surface temperature. Flight data indicated that boundary-layer transition from laminar to turbulent flow starts at 1235 sec. The inlet gas temperature increases at this time due to the change in boundary-layer temperature profile. A peak filler-bar temperature of 1502°F occurred at $t = 1285$ sec. Figures 40 and 41 give a similar set of results for 0.04-in. tile step height. The calculated temperatures for the filler-bar membrane node which reaches the highest temperature (node 4022) are given in figure 42 for the fuselage location. For this case, the filler-bar temperature peaks at 969°F. These two step height runs at the fuselage location represent category 3 and category 1 charring conditions (table III). The filler-bar temperature distribution at the time when the peak temperature occurs is given in table IV.

Results were obtained for three tile steps at the wing location $X = 1220$, $Y = 275$. The tile thickness at this location is 2.25 in. The step heights which were run are 0.017 in., 0.03 in., and 0.06 in. The 0.017-in. step height case was run because 0.017 in. is the maximum design step height allowed at this wing location. The 0.03-in. and 0.06-in. step height cases were run to represent category 1 and category 3 filler-bar charring, respectively. Figures 43 through 48 show the pressures and calculated temperatures for the wing location. The peak filler-bar temperatures calculated for the three step heights were 849°F for the 0.017-in. step, 1284°F for the 0.03-in. step, and 1748°F for the 0.06-in. step. The calculated temperatures for filler-bar membrane node 4022 are given in figure 49 for the wing location. The calculated peak temperatures and temperature distribution for the filler-bar membrane are given in table IV. The calculated gap-width variation during entry for representative cases is given in table V. The results indicate that filler-bar temperature is strongly dependent on step height.

The effect of early boundary-layer transition on peak filler-bar temperature was studied by assuming transition at 1225 sec (10 sec earlier) for the 0.1-in. step case at the fuselage location. The calculated filler-bar temperature peaked at 1578°F, compared with 1502°F for transition at 1235 sec.

POTENTIAL SOLUTION TO THE PROBLEM OF FILLER-BAR CHARRING

The previous analyses have shown that filler-bar charring can be caused by the flow of hot gases in the tile-to-tile gaps as a result of forward-facing and rearward-facing steps at the surface. The flow of hot gases in the gap can be reduced by installation of gap fillers between the tiles with excessive steps. Many ceramic fiber products have the combination of high flow resistance and high temperature capability, which is needed for a gap filler.

The thermal model was used to estimate the performance of a half-height gap filler. A sketch of the gap filler is shown in figure 50. The material chosen for the gap filler was Carborundum Fiberfrax 880JH. The density of this material is 6 lbm/ft³. The permeability was measured experimentally and found to be 3.66×10^{-10} ft² at a pressure of 142 psf (pounds per square foot). The pressure

gradient was 1114 psf per foot. (See table VI for test results.) This gap-filler material has a temperature capability of 2600°F. The adjustment to the model to represent the gap filler was to set the tile-to-tile gap such that the flow resistance of the gap was equivalent to the flow resistance of a 0.05-in. gap with a half-height ceramic fiber gap filler installed. First, the size gap which is equivalent to a 0.05-in. gap with a full gap filler installed was determined. Based on a gap-filler permeability of $3.66 \times 10^{-10} \text{ ft}^2$, the equivalent gap width is 0.00316 in. An approximation for the equivalent gap width for a half-height gap filler of this type is obtained by multiplying the full gap-filler equivalent gap width by the cube root of 2. The half-height gap-filler equivalent gap thus obtained is 0.00398 in. The thermal model was run with an initial gap width of 0.004 in. to represent the installation of this half-height gap filler in the 0.05-in. tile-to-tile gap. The wing location with a 0.06-in. tile-to-tile step was chosen for the gap-filler run analysis. The pressure boundary conditions used for this run are the same as for the analysis without the gap filler and are given in figure 31. The temperature results of the gap-filler analysis are given in figure 51. The results show that the addition of the gap filler protected the filler bar, so that charring would not occur. The maximum calculated temperature of the filler-bar membrane was only 450°F, while 970°F is required to start the charring process. The calculated filler-bar temperature for the same case, but with a 0.05-in. gap without a gap filler, was 1748°F. The gap filler reduced the filler-bar temperature by 1298°F.

CONCLUDING REMARKS

An analysis of the heating that occurs during entry in the tile-to-tile gap due to uneven tile heights in the Shuttle orbiter thermal protection system has been performed. In order to conduct the analysis, a technique was developed for predicting the local pressure disturbance caused by a stepped tile. In addition, a method was developed for calculating the airflow rates in the tile-to-tile gaps, and for predicting the temperature level of the gas ingested from the boundary layer. A thermal analysis was conducted on the stepped-tile configuration to determine the extent of heating on the tile sidewalls, the filler bar, and the SIP due to the hot-air flow in the gap. Combinations of tile step heights and resulting tile-to-tile gaps that could cause varying degrees of damage to the filler bar on the lower fuselage and wing were determined. The magnitudes of the predicted step heights and gaps were comparable to the step heights and gaps that were observed in damaged regions after the initial flights of the Shuttle. Filler-bar charring may be prevented by controlling steps within tight tolerances during installation and maintaining these tolerances in flight. The acceptable in-flight steps were 0.04 in. at the fuselage location and 0.017 in. at the wing location. If the tolerances cannot be maintained, tile-to-tile gap filler would be an alternative. A ceramic fiber gap filler was investigated analytically using the techniques described in the paper. The results indicate that the gap filler would reduce the airflow rates sufficiently to prevent damage to the filler bar.

Langley Research Center
National Aeronautics and Space Administration
Hampton, VA 23665
July 27, 1983

REFERENCES

1. Compton, Harold R.; Findlay, John T.; Kelly, George M.; and Heck, Michael L.: Shuttle (STS-1) Entry Trajectory Reconstruction. AIAA-81-2459, Nov. 1981.
2. Tannehill, J. C.; and Mugge, P. H.: Improved Curve Fits for the Thermodynamic Properties of Equilibrium Air Suitable for Numerical Computation Using Time-Dependent or Shock-Capturing Methods. NASA CR-2470, 1974.
3. Adams, John C., Jr.; and Martindale, William R.: Hypersonic Lifting Body Windward Surface Flow-Field Analysis for High Angles of Incidence. AEDC-TR-73-2, U.S. Air Force, Feb. 1973. (Available from DTIC as AD 756 499.)
4. Hamilton, H. Harris, II: Approximate Method of Predicting Heating on the Windward Side of Space Shuttle Orbiter and Comparisons with Flight Data. AIAA-82-0823, June 1982.
5. Wu, Jain-Ming; Su, Michael W.; and Moulden, Trevor H.: On the Near Flow Field Generated by the Supersonic Flow Over Rearward Facing Steps. ARL 71-0243, U.S. Air Force, Nov. 1971. (Available from DTIC as AD 736 770.)
6. Zukoski, Edward E.: Turbulent Boundary-Layer Separation in Front of a Forward-Facing Step. AIAA J., vol. 5, no. 10., Oct. 1967, pp. 1746-1753.
7. Uebelhack, H. T.: Turbulent Flow Separation Ahead of Forward Facing Steps in Supersonic Two-Dimensional and Axisymmetric Flows. VKI-TN-54, Von Karman Inst. Fluid Dyn., July 1969.
8. Bobbitt, P. J.; Edwards, C. L. W.; and Barnwell, R. W.: The Simulation of Time Varying Ascent Loads on Arrays of Shuttle Tiles in a Large Transonic Tunnel. AIAA-82-0566, Mar. 1982.
9. Wu, J. M.; Vakili-Dastjerd, A.; Collins, F. G.; Reddy, K. C.; Moulden, T. H.; Bhat, M. K.; and Dowgwillo, R. M.: Fundamental Studies of Subsonic and Transonic Flow Separation, Part III. Third Phase Summary Report. Rep. No. AEDC-TR-79-48, U.S. Air Force, Oct. 1979. (Available from DTIC as AD A074 868.)
10. Ames Research Staff: Equations, Tables, and Charts for Compressible Flow. NACA Rep. 1135, 1953. (Supersedes NACA TN 1428.)
11. Bogdonoff, Seymour M.: Some Experimental Studies of the Separation of Supersonic Turbulent Boundary Layers. Rep. No. 336 (Contract No. AF 18(600)-498), Dept. Aeronaut. Eng., Princeton Univ., June 1955.
12. Czarnecki, K. R.; and Jackson, Mary W.: Turbulent Boundary-Layer Separation Due to a Forward-Facing Step. AIAA J., vol. 13, no. 13, Dec. 1975, pp. 1585-1591.
13. Driftmyer, Richard T.: A Forward Facing Step Study: The Step Height Less Than the Boundary-Layer Thickness. NOLTR 73-98, U.S. Navy, May 11, 1973. (Available from DTIC as AD 764 512.)
14. Lord, Douglas R.; and Czarnecki, K. R.: Aerodynamic Loadings Associated With Swept and Unswept Spoilers on a Flat Plate at Mach Numbers of 1.61 and 2.01. NACA RM L55L12, 1956.

15. Martin Marietta Interactive Thermal Analysis System - MITAS-II-NOS-FTN Version. User's Manual. Martin Marietta Data Systems, Apr. 1977.
16. Sawyer, James Wayne; and Waters, William Allen, Jr.: Room Temperature Shear Properties of the Strain Isolator Pad for the Shuttle Thermal Protection System. NASA TM-81900, 1981.
17. Schlichting, Hermann (J. Kestin, transl.): Boundary-Layer Theory, Sixth ed. McGraw-Hill Book Co., Inc., c.1968.
18. White, Frank M.: Viscous Fluid Flow. McGraw-Hill, Inc., c.1974.
19. Wiebelt, John A.: Engineering Radiation Heat Transfer. Holt, Rinehart and Winston, Inc., c.1966.
20. Swofford, Doyle P.: A Method for the Thermal Analysis of Spacecraft, Including All Multiple Reflections and Shading Among Diffuse, Gray Surfaces. NACA TN D-5910, 1970.
21. Bird, R. Byron; Stewart, Warren E.; and Lightfoot, Edwin N.: Transport Phenomena. John Wiley & Sons, Inc., c.1960.
22. Scott, Carl D.; and Maraia, Robert J.: Gap Heating With Pressure Gradients. AIAA Paper 79-1043, June 1979.
23. Chapman, Dean R.; and Rubesin, Morris W.: Temperature and Velocity Profiles in the Compressible Laminar Boundary Layer With Arbitrary Distribution of Surface Temperature. J. Aeronaut. Sci., vol. 16, no. 9, Sept. 1949, pp. 547-565.
24. Elliott, David G.; Bartz, Donald R.; and Silver, Sidney: Calculation of Turbulent Boundary-Layer Growth and Heat Transfer in Axi-Symmetric Nozzles. Tech. Rep. No. 32-387 (Contract No. NAS 7-100), Jet Propulsion Lab., California Inst. Technol., Feb. 15, 1963.

TABLE I.- SURFACE HEAT-FLUX DATA USED FOR FUSELAGE POINT
X = 750, Y = -75

[From Space Shuttle Orbiter Entry Aerodynamic Heating
Data Book, Rockwell Publication SD73-SH-0184,
Revision C, October 1978]

Time, sec	Convective heating, btu/ft ² -sec, for wall temperature of -			
	0°F	650°F	2000°F	3500°F
0	0	0	0	0
100	.56	.54	.52	.50
260	3.80	3.63	3.29	2.90
340	8.80	8.54	8.00	7.40
460	9.40	9.18	8.71	8.20
840	9.05	8.80	8.28	7.70
940	8.60	8.28	7.63	6.90
1060	6.25	5.97	5.39	4.75
1250	2.00	1.74	1.20	.60
1300	5.90	4.80	2.30	0
1500	1.20	.216	-1.83	4.10
1660	0	-1.30	-3.75	-5.80
1900	.75	-4.10	-11.20	-17.25

TABLE II.- SURFACE TEMPERATURE DATA USED FOR WING POINT
X = 1220, Y = 275

[From Space Shuttle Orbiter Entry Aerodynamic Heating
Data Book, Rockwell Publication SD73-SH-0184,
Revision C, October 1978]

Time, sec	Wall temperature, °F
0	40
505	1830
634	1820
811	1815
915	1805
1013	1720
1104	1540
1200	1478
1298	1630
1335	1542
1375	1423

TABLE III.- STS-1 MEASUREMENTS IN DAMAGED FILLER-BAR AREAS

STS-1 Postflight measurements in damaged filler-bar areas

Tile-to-tile steps	-0.099 in. to 0.12 in.
Tile-to-tile gaps	0.010 in. to 0.13 in.

Categorization of damaged filler bar

Category	Temperature	Damage
1	970°F	Silicone-rubber membrane discolored
2	1100°F	Silicone-rubber membrane charred
3	1375°F	Silicone-rubber membrane and filler bar charred

Approximately 600 damaged filler bars on STS-1

TABLE IV.- CALCULATED PEAK TEMPERATURES AND TEMPERATURE DISTRIBUTION FOR FILLER-BAR MEMBRANE

Step height, in.	Temperature, °F, at filler-bar node location -			Time, sec
	2022	3022	4022	
Fuselage				
0.1	1420	1480	1502	1285
.04	895	944	969	1375
Wing				
0.06	1555	1725	1748	1280
.03	1262	1258	1284	1300
.017	813	815	849	1448

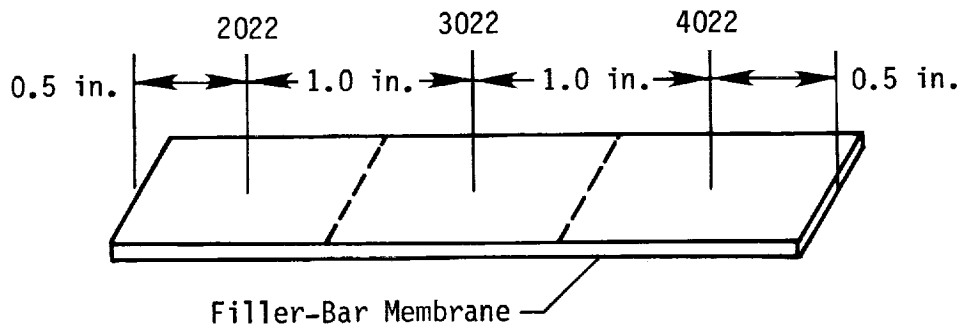


TABLE V.- CALCULATED GAP WIDTH VARIATION
DURING STS-1 ENTRY

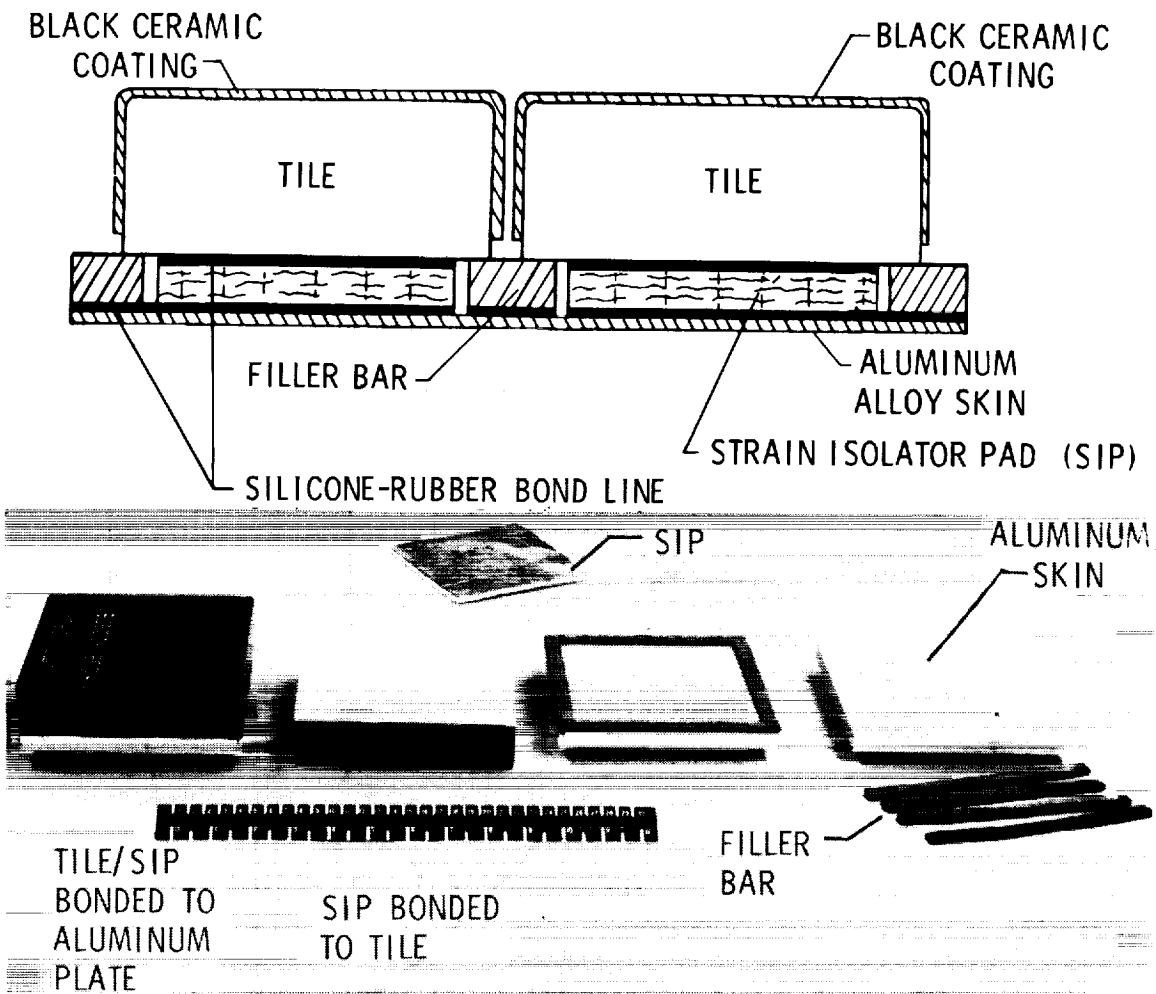
Fuselage		
Time, sec	Gap, in., with -	
	0.1-in. step	0.04-in. step
0	0.05	0.05
634	.053	.05
811	.056	.051
1013	.071	.055
1235	.081	.063
1298	.092	.067

Wing		
Time, sec	Gap, in., with -	
	0.06-in. step	0.017-in. step
0	0.05	0.05
634	.053	.05
811	.058	.051
1013	.089	.053
1200	.102	.064
1298	.103	.063

TABLE VI.- PERMEABILITY TEST RESULTS FOR CARBORUNDUM FIBERFRAX 880JH
CERAMIC FIBER BLANKET

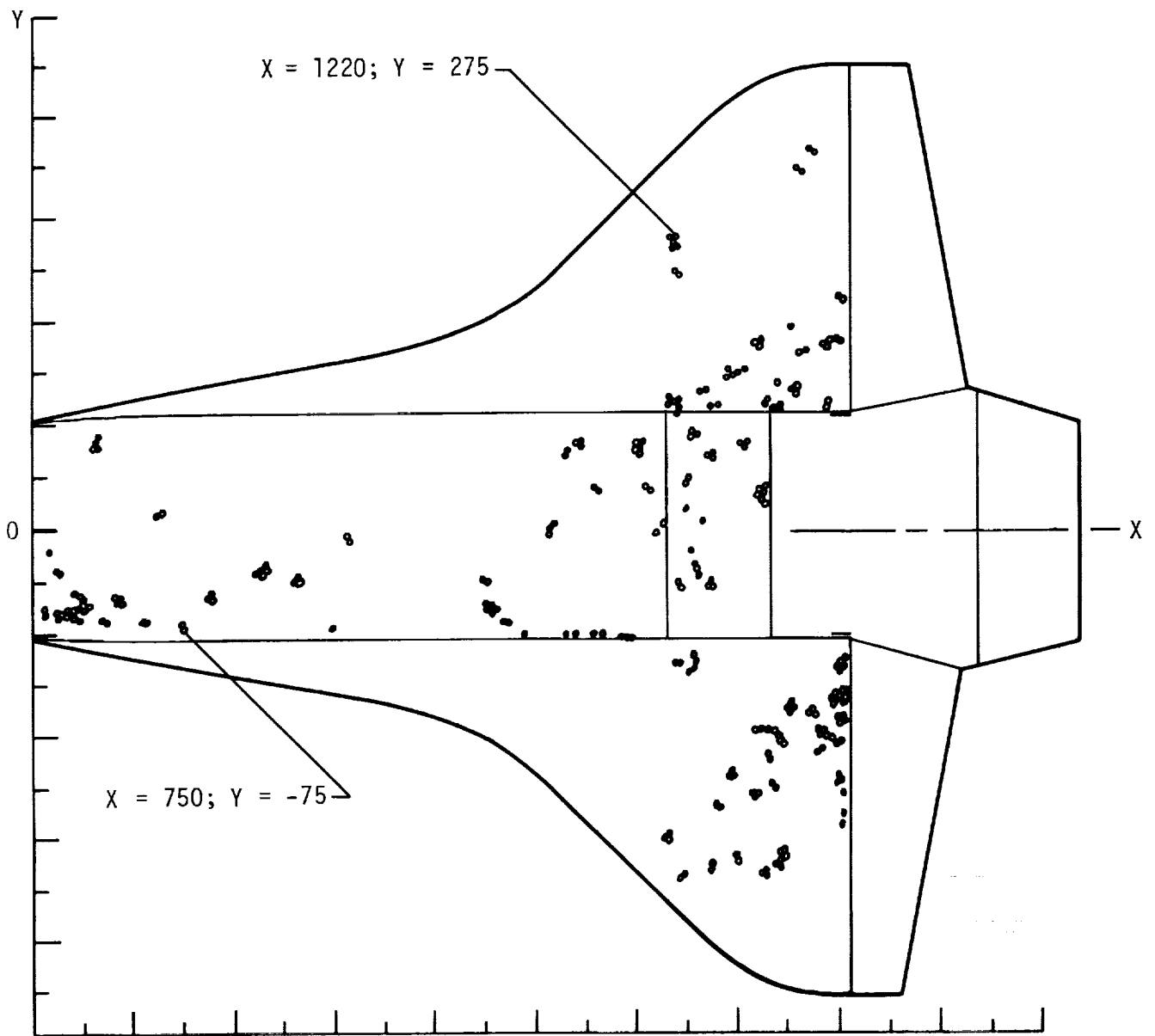
Sample thickness = 0.093 in.
 Sample width = 1.26 in.
 Sample length = 1.26 in.
 Sample frontal area = 0.1172 in²
 Standard temperature = 70°F
 Standard pressure = 2116 psf

Flow, standard ft ³ /min	P ₁ , psf	P ₂ , psf	\dot{m} , lbm/sec	$-\frac{dp}{ds}$, psf/ft	K _p , ft ²
3.53 × 10 ⁻³	200.5	83.5	4.409 × 10 ⁻⁶	1114	3.66 × 10 ⁻¹⁰
7.06	273.4	83.5	8.818 × 10 ⁻⁶	1816	3.57
10.6	338.3	83.5	1.323 × 10 ⁻⁵	2426	3.40
14.1	396.8	83.5	1.764	2893	3.24
17.6	448.3	83.5	2.205	3474	3.14
14.1	398.5	83.5	1.764	2999	3.21
10.6	342.5	83.5	1.323	2466	3.31
7.06	278.5	83.5	8.818 × 10 ⁻⁶	1856	3.45
3.53	203.3	83.5	4.409 × 10 ⁻⁶	1141	3.54



(a) Tile configuration on lower surface of orbiter.

Figure 1.- Thermal protection system design and char pattern.



(b) Charred filler-bar locations on lower surface of orbiter.

Figure 1.- Concluded.

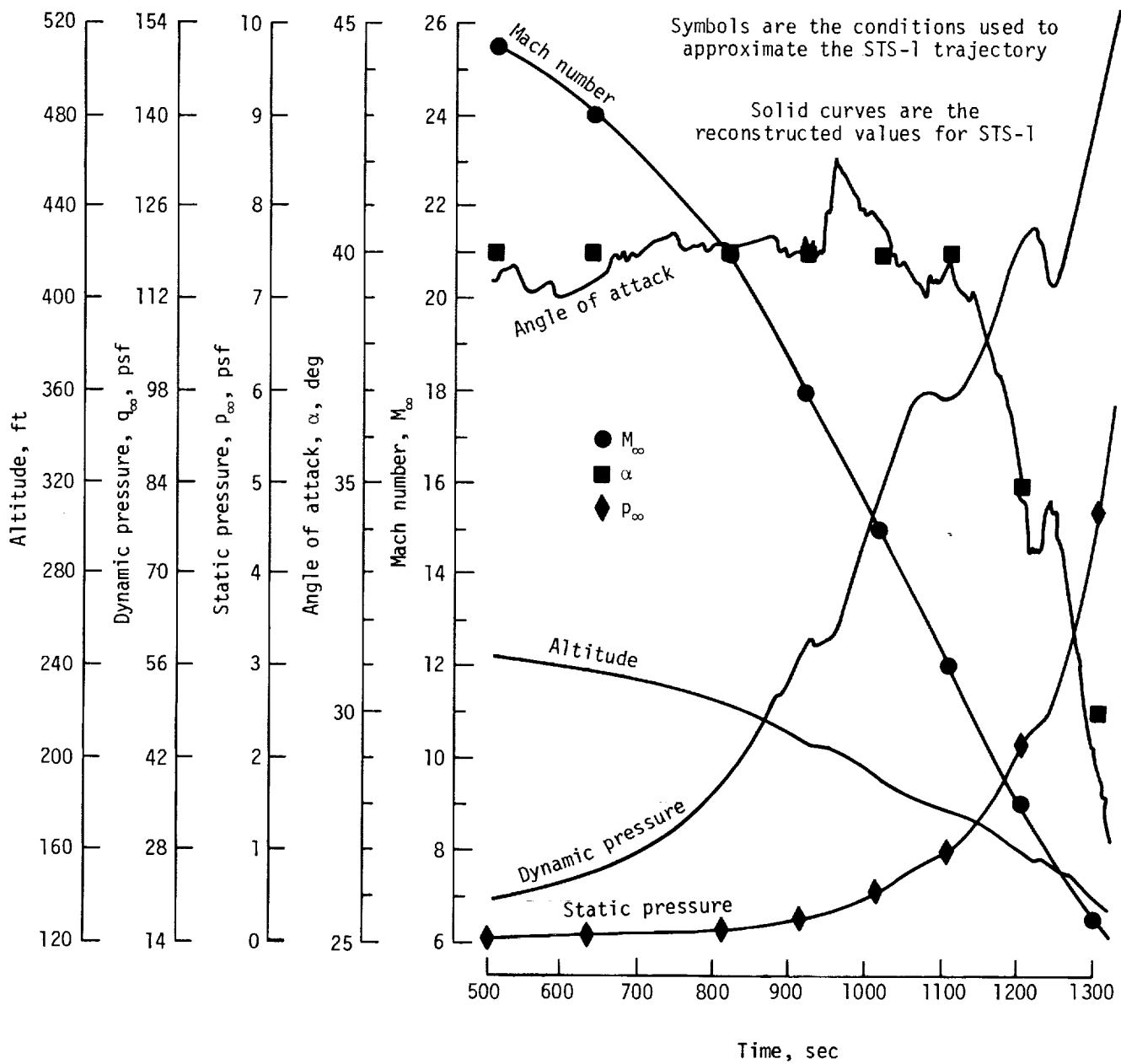


Figure 2.- Reconstructed STS-1 entry trajectory and approximated values used in filler-bar charring analysis.

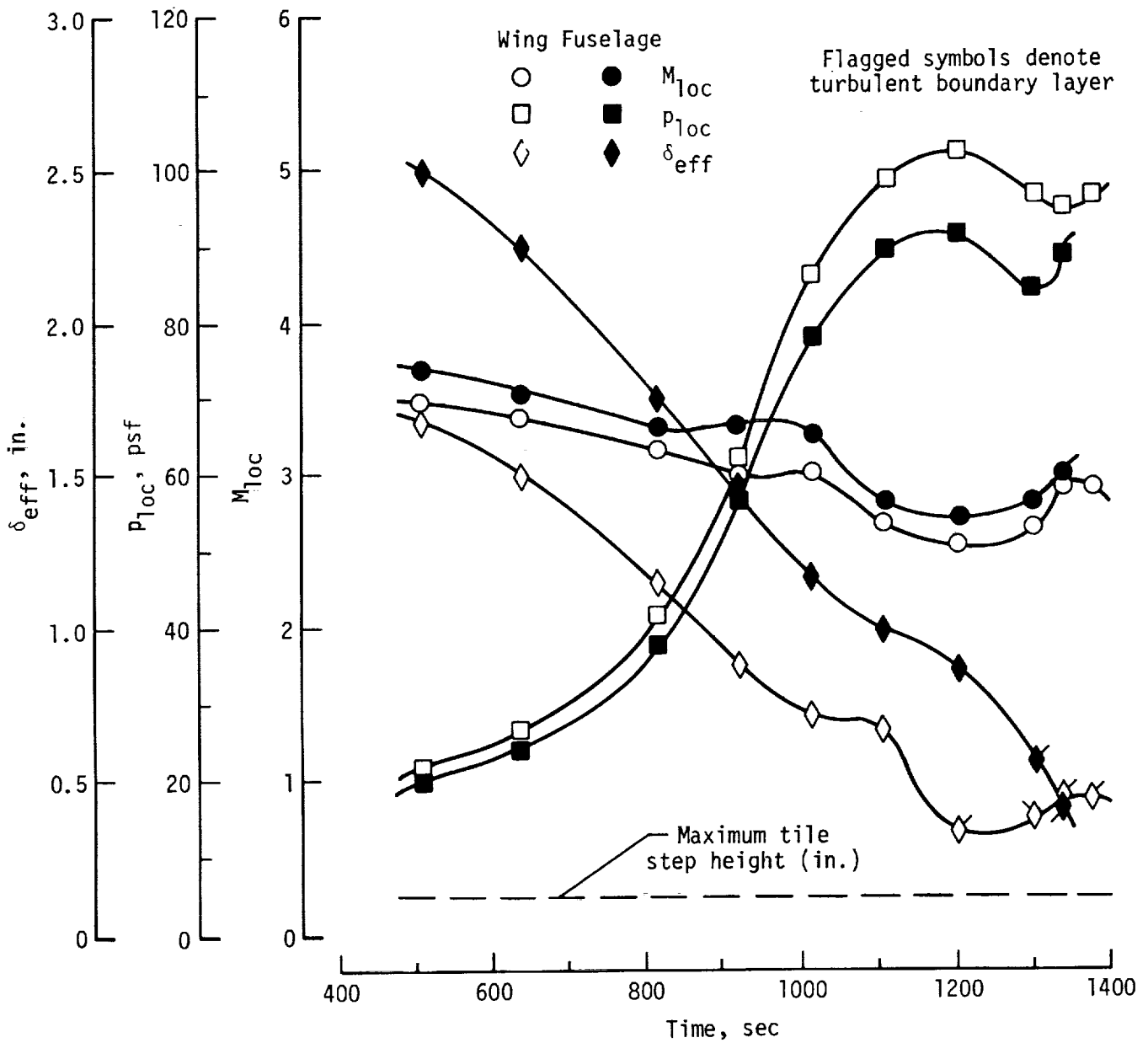


Figure 3.- Local flow conditions.

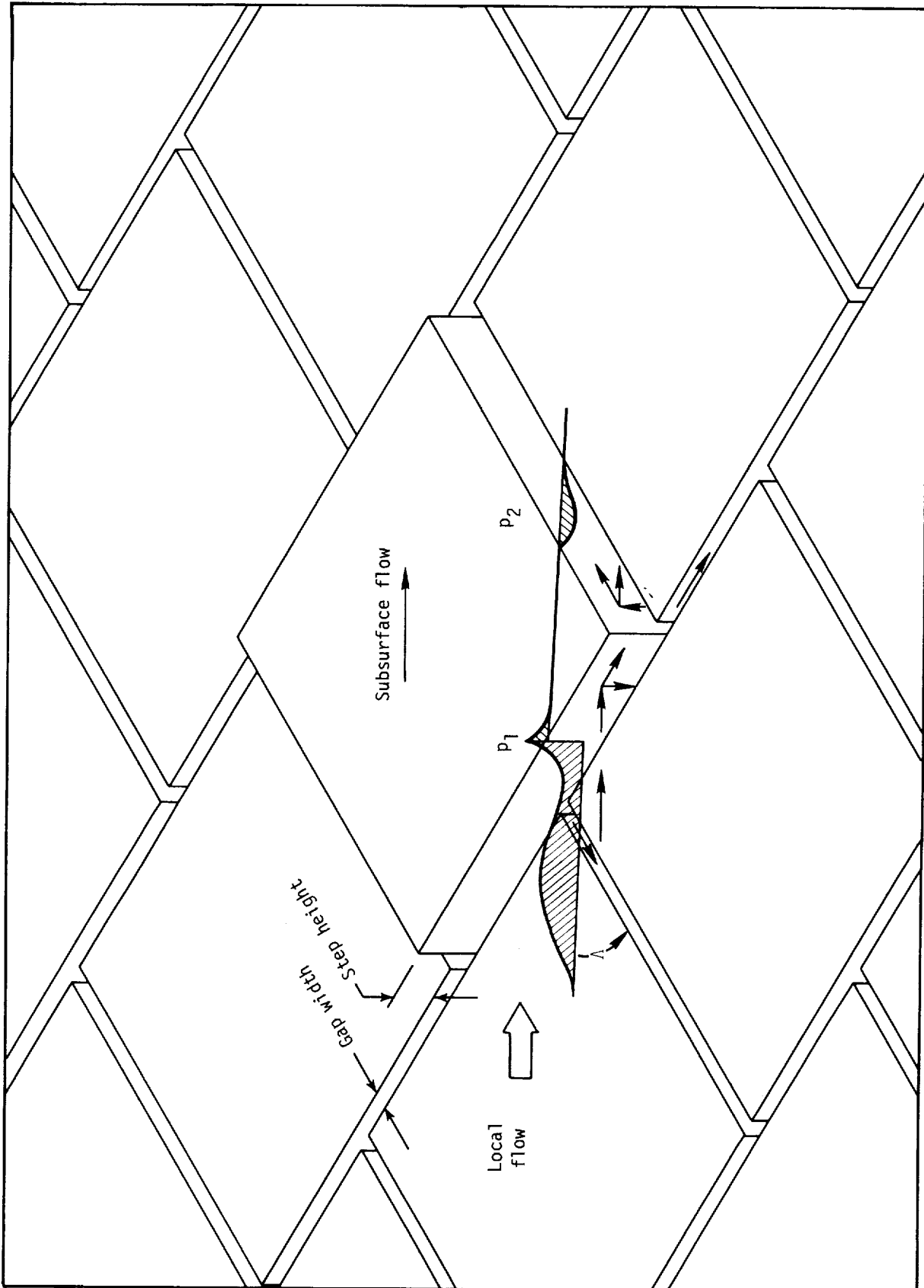


Figure 4.- Schematic of flow patterns and key parameters associated with a vertically displaced tile.

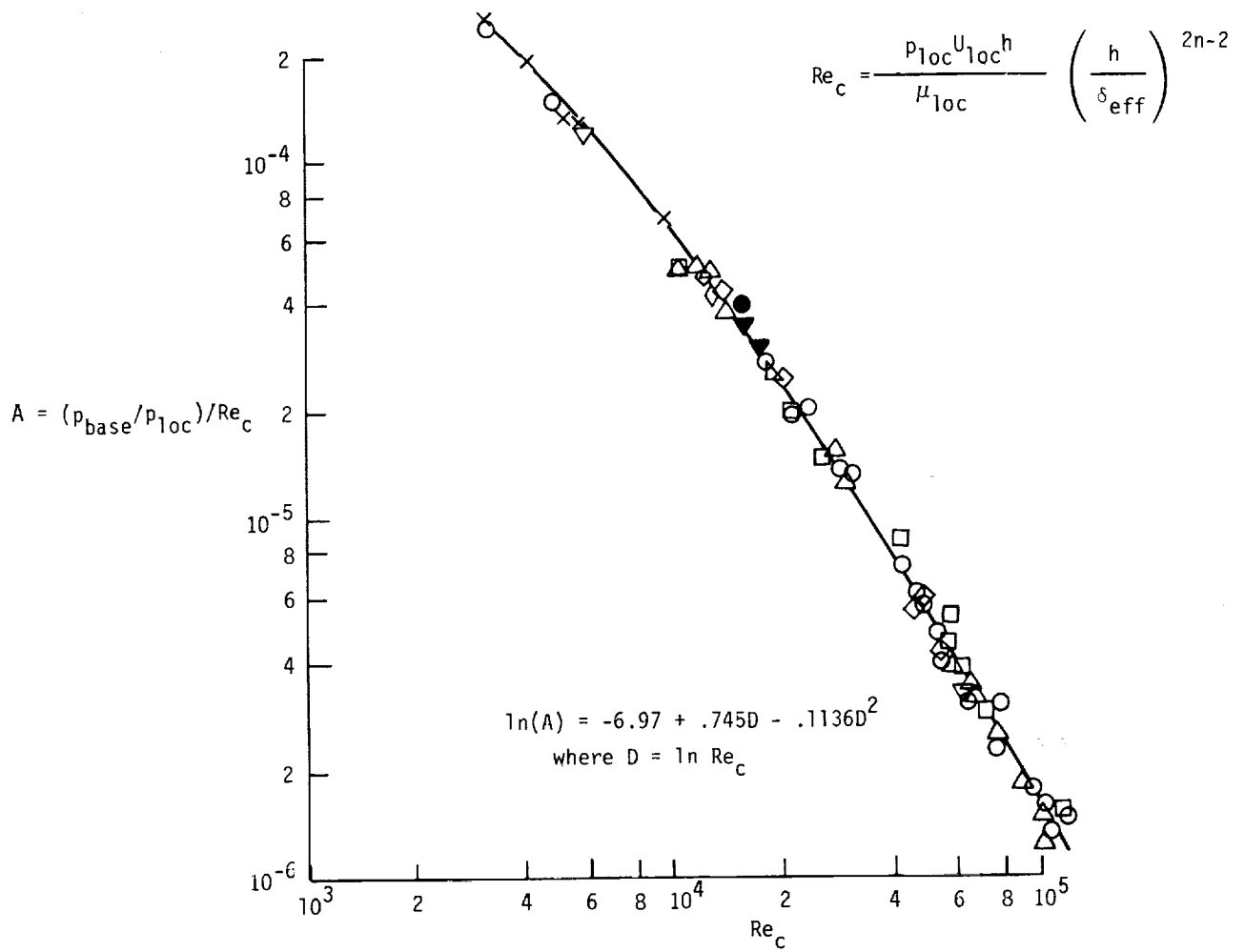


Figure 5.- Base pressure correlation as presented in reference 5.

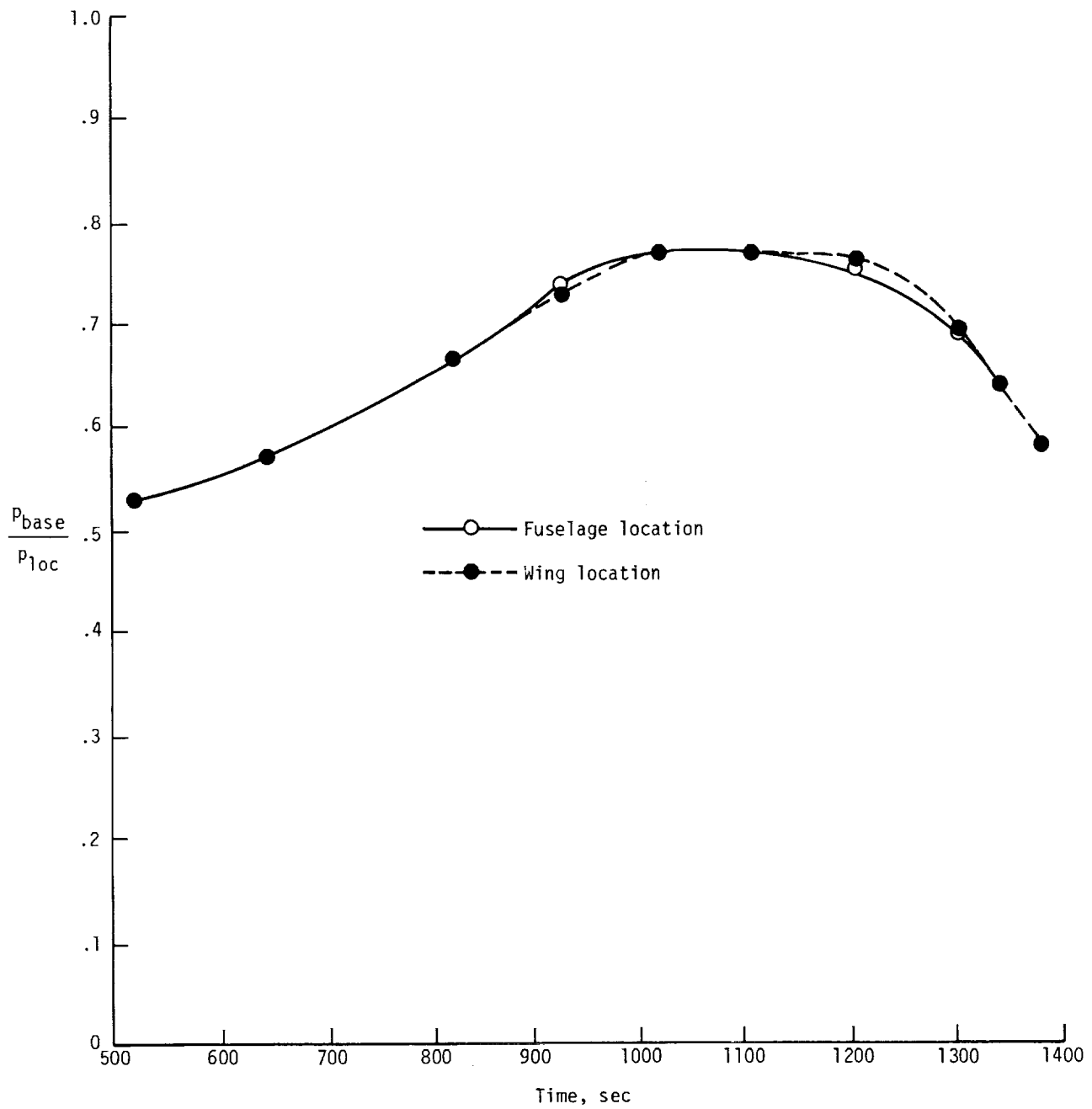


Figure 6.- Base pressure histories for fuselage and wing locations during STS-1 entry.

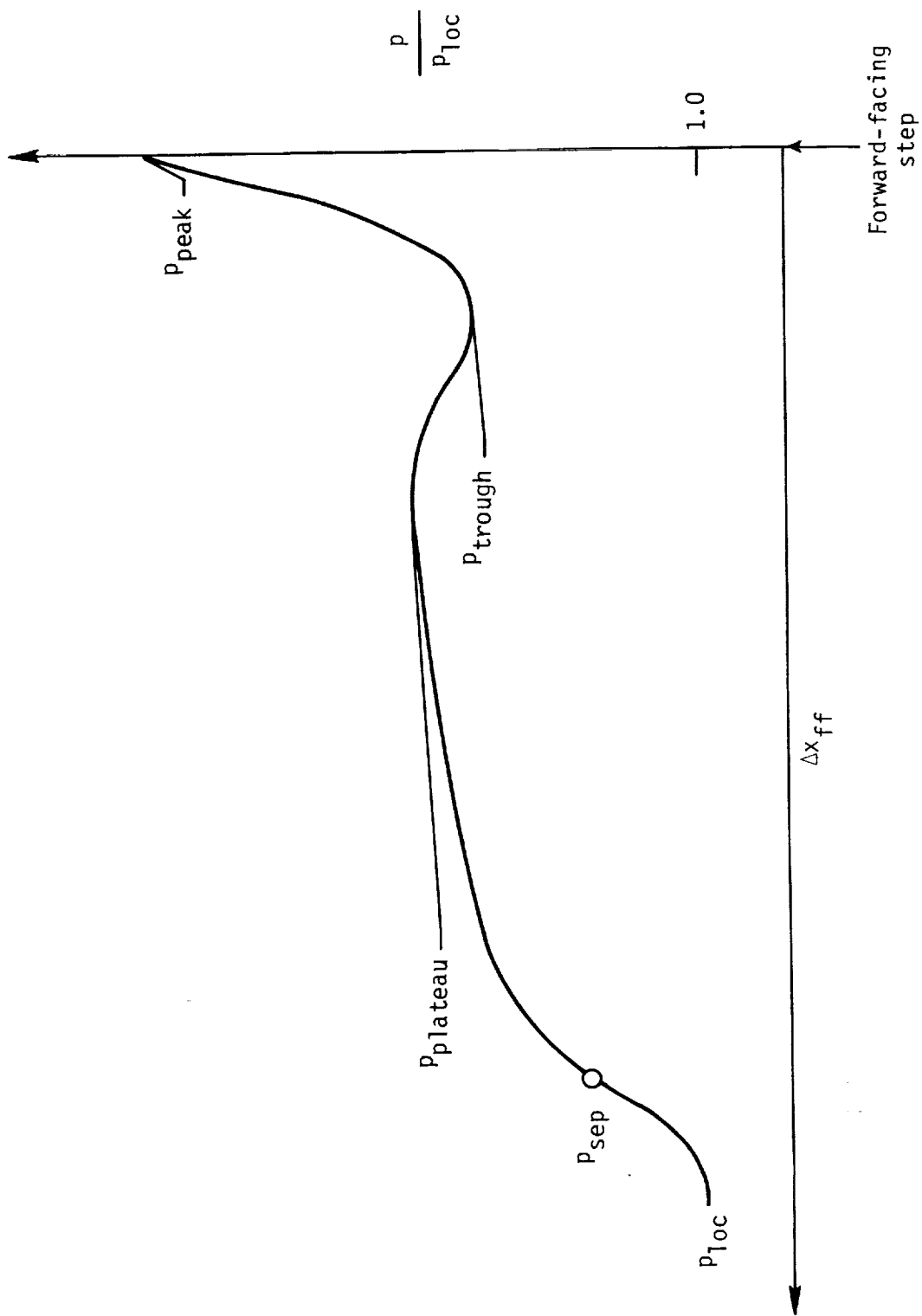


Figure 7.- Typical separated-flow pressure profile ahead of a forward-facing step.

$$\frac{P_{plateau}}{P_{1oc}} = 0.56M_{1oc} + 0.80$$

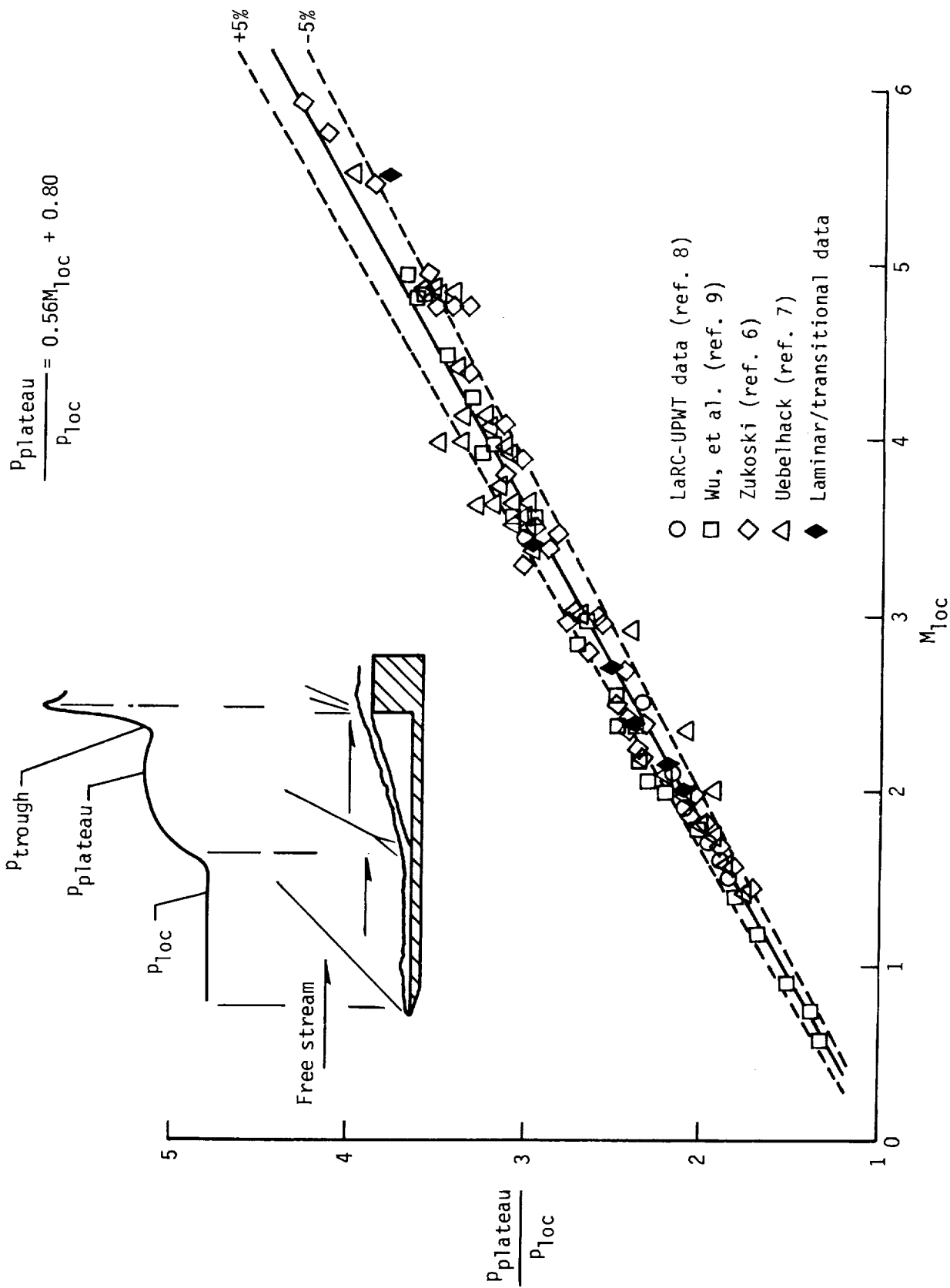


Figure 8.- Plateau pressure correlation.

$$x_{sep} = h \cot \phi$$

$$\cot \phi = \left[\frac{\gamma M_{loc}^2 - \xi_p + 1}{\xi_p - 1} \right] \sqrt{\frac{2\gamma M_{loc}^2 - (\gamma - 1) - (\gamma + 1)\xi_p}{(\gamma + 1)\xi_p + (\gamma - 1)}}$$

$$\xi_p = 0.56M_{loc} + 0.80$$

γ = effective γ for real gas effects when the free stream Mach number is high

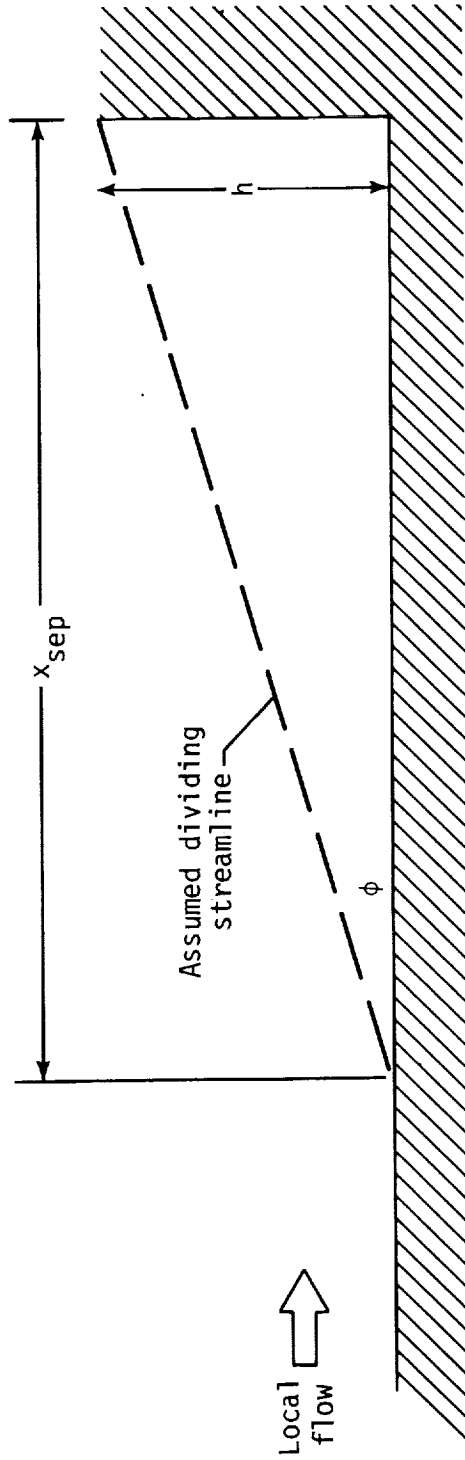


Figure 9.- Method for estimating length of separation.

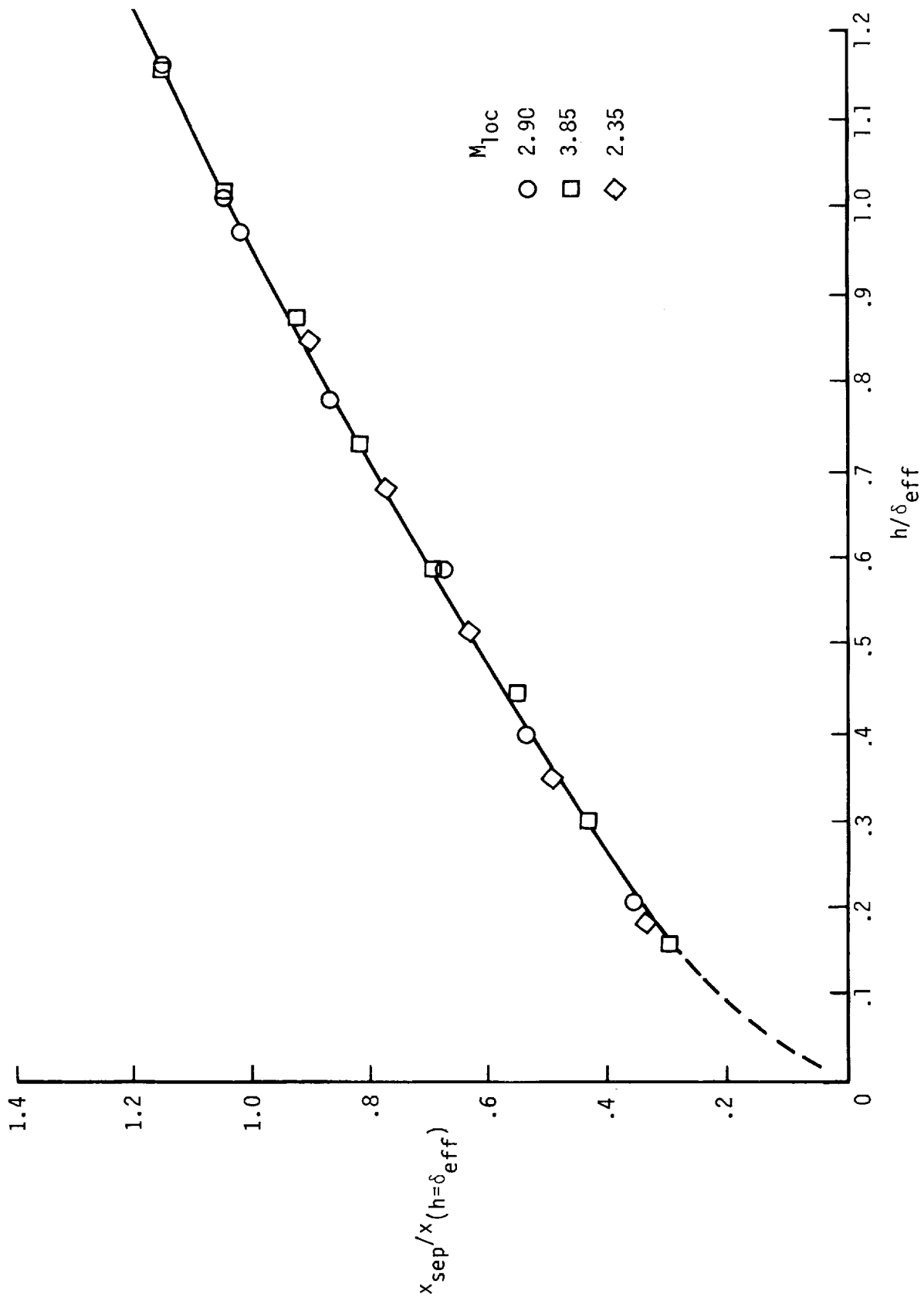
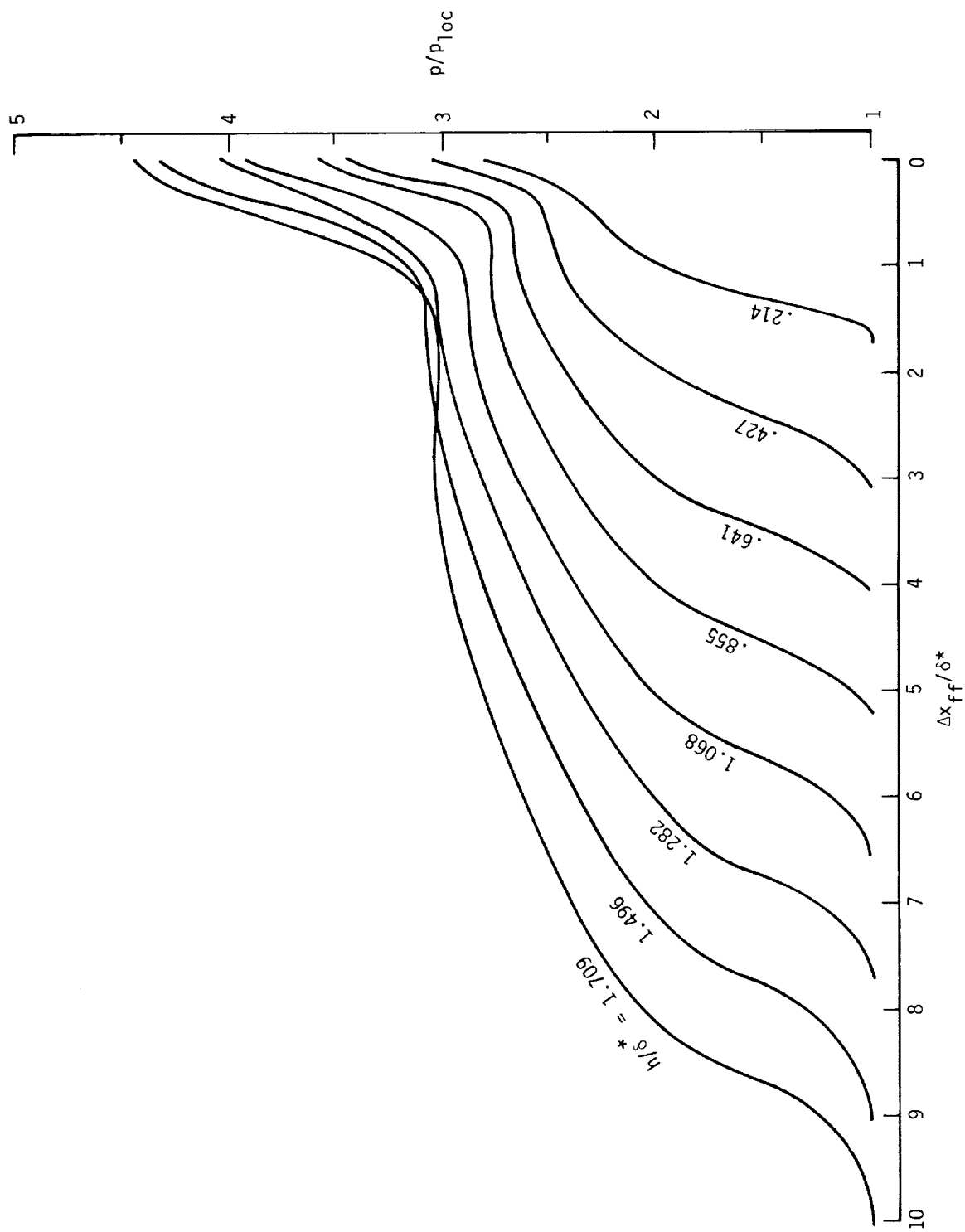
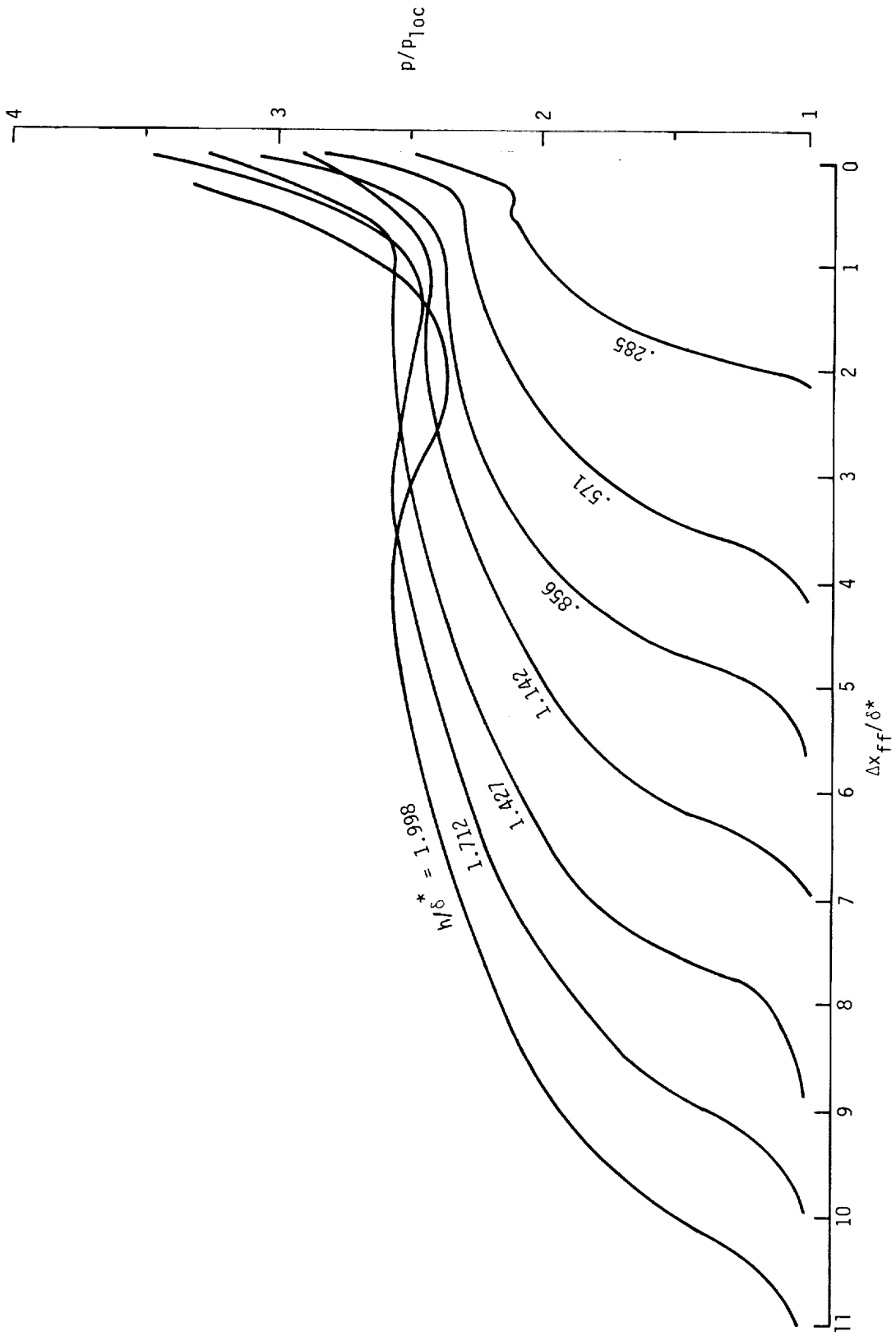


Figure 10.- Truncation correlation for separated-flow curve ahead of forward-facing steps whose heights are fractions of boundary-layer thickness.



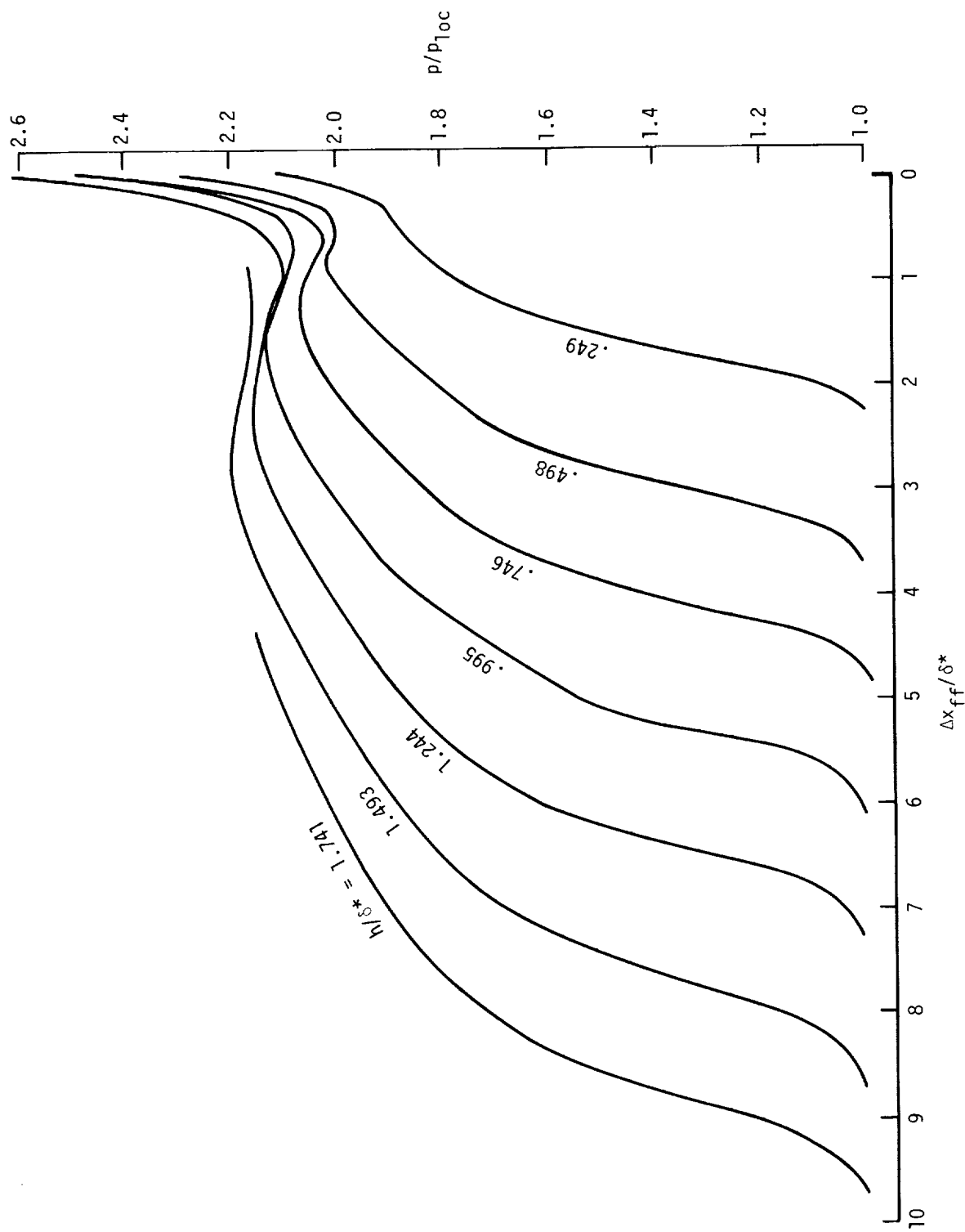
(a) $M_{1oc} = 3.85$; $\delta^* = 0.234$ in.

Figure 11.- Experimental separated-flow pressure distributions for turbulent flow ahead of forward-facing steps whose heights are fractions of boundary-layer thickness.



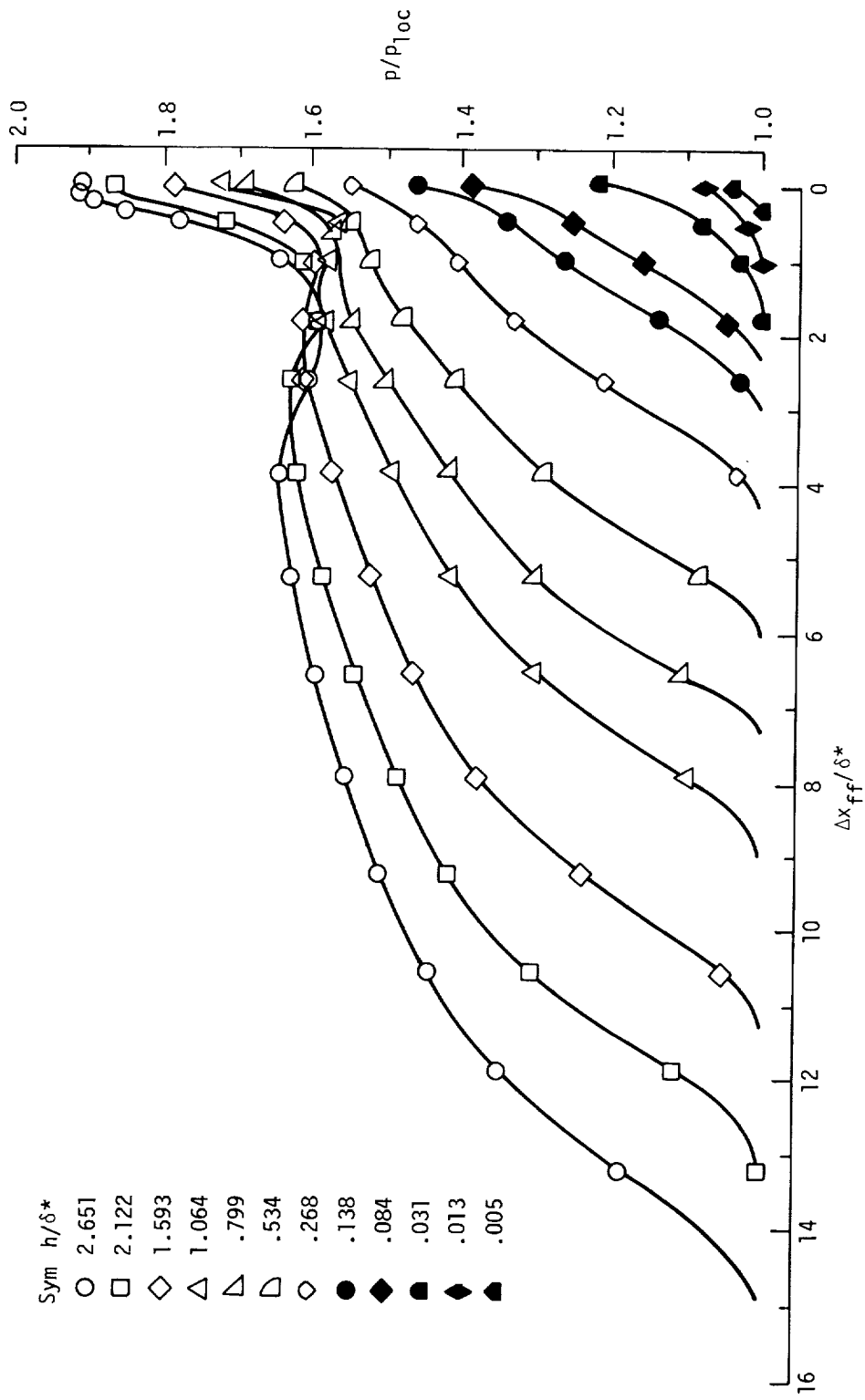
(b) $M_{1oc} = 2.90$; $\delta^* = 0.175$ in.

Figure 11.- Continued.



(c) $M_{10c} = 2.35$; $\delta^* = 0.201$ in.

Figure 11.- Continued.



(d) $M_{loc} = 1.61$; $\delta^* = 0.378$ in.

Figure 11.- Concluded.

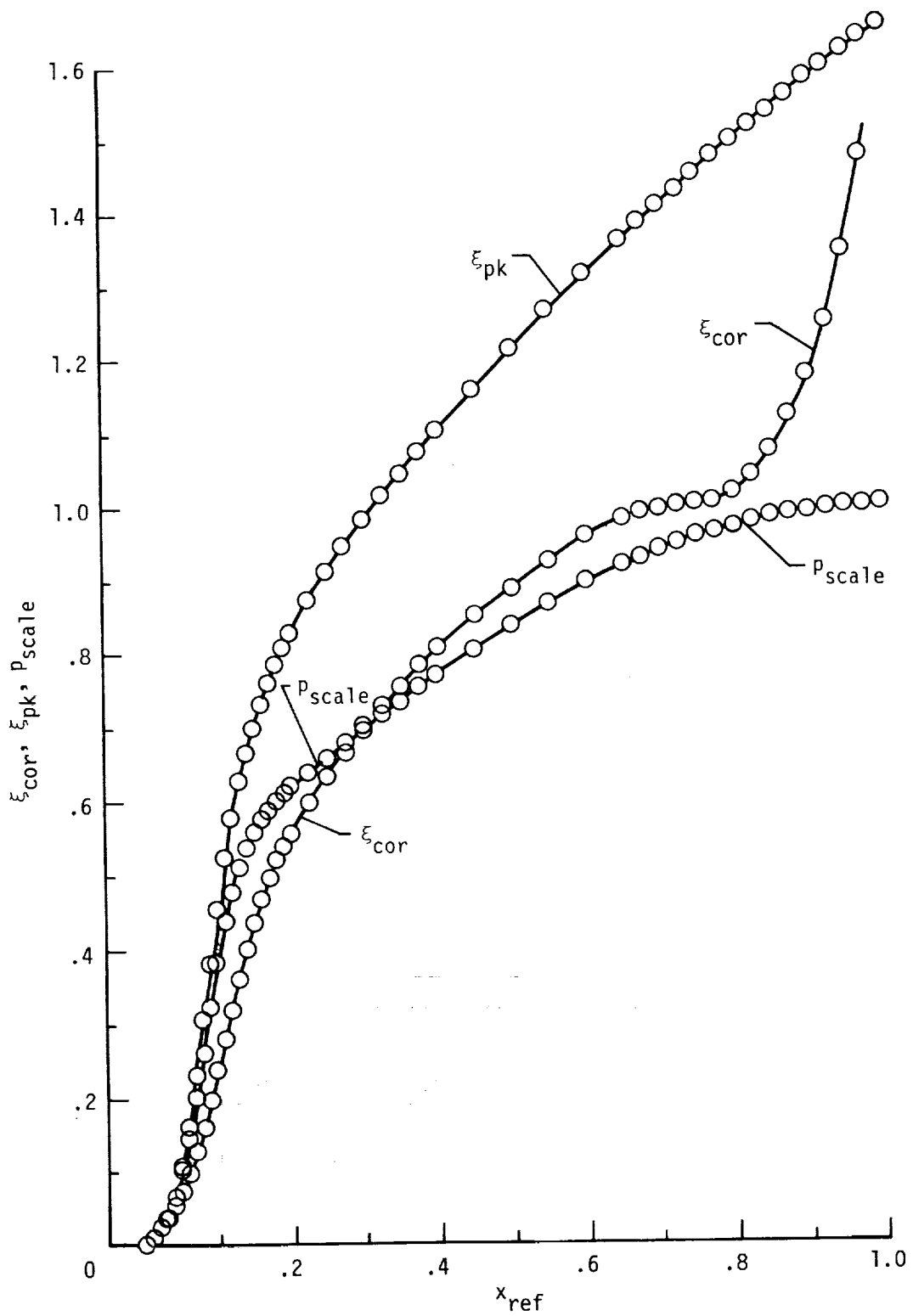
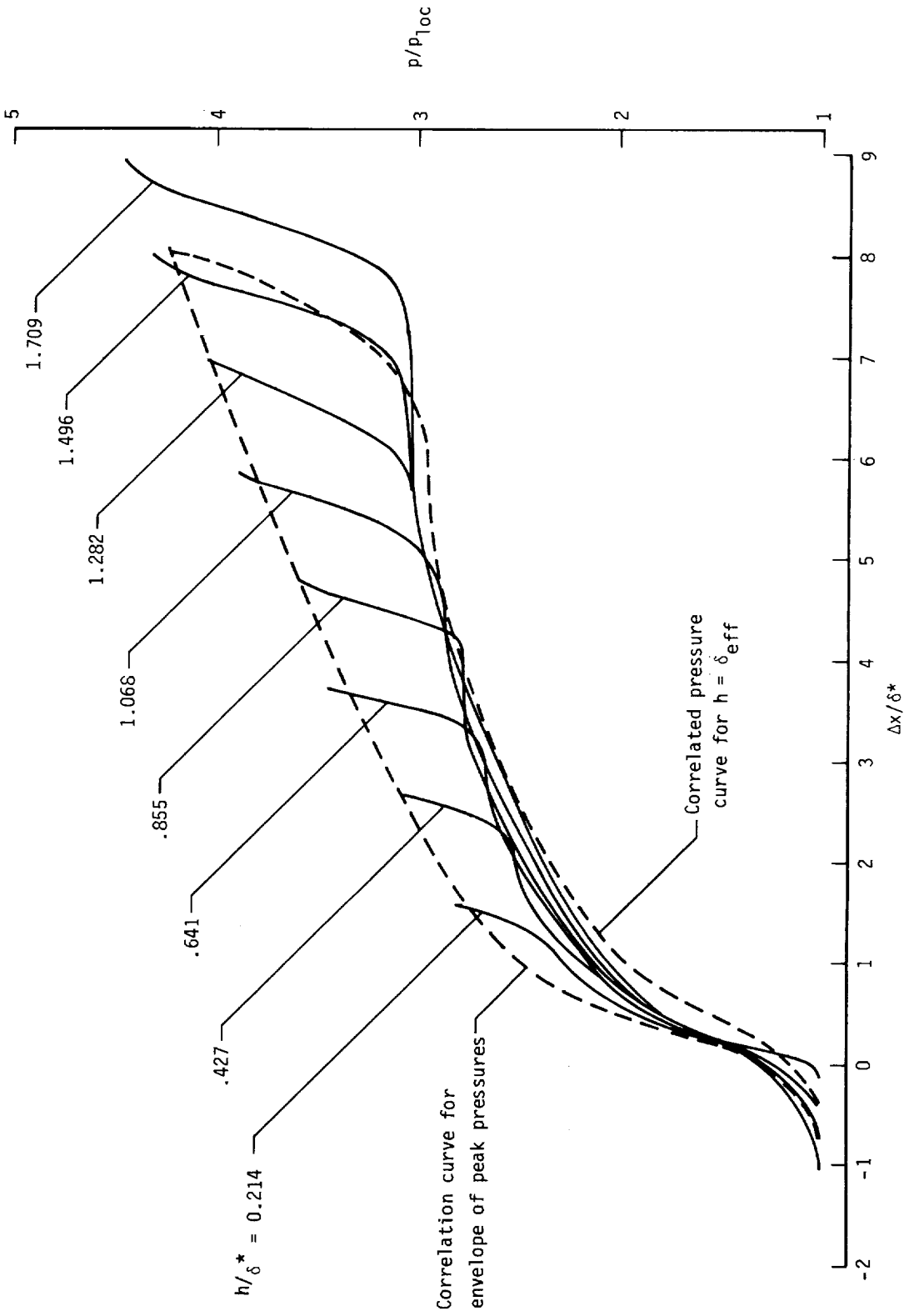
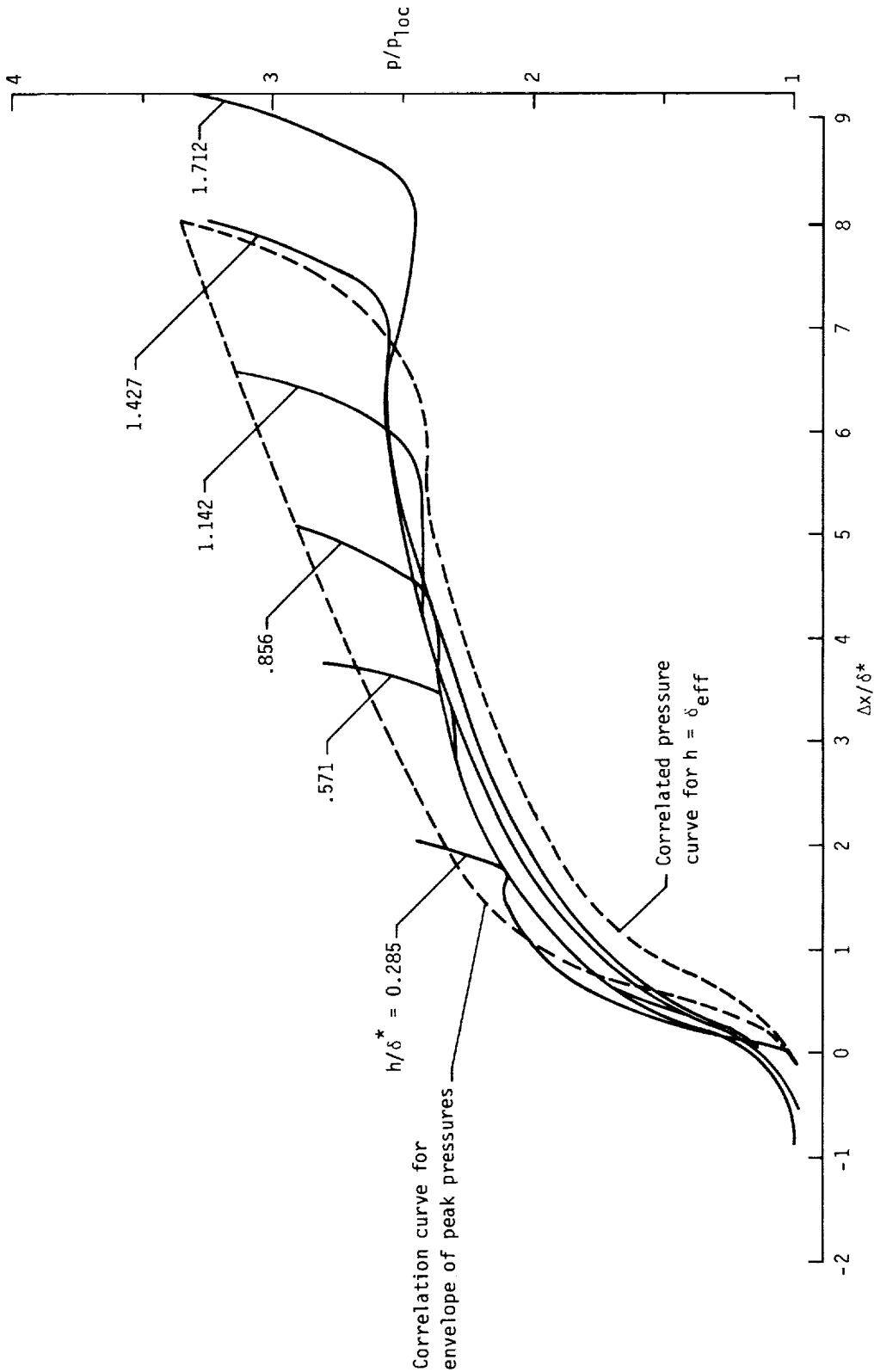


Figure 12.- Correlations of separated-flow pressure-ratio distributions ahead of forward-facing steps.



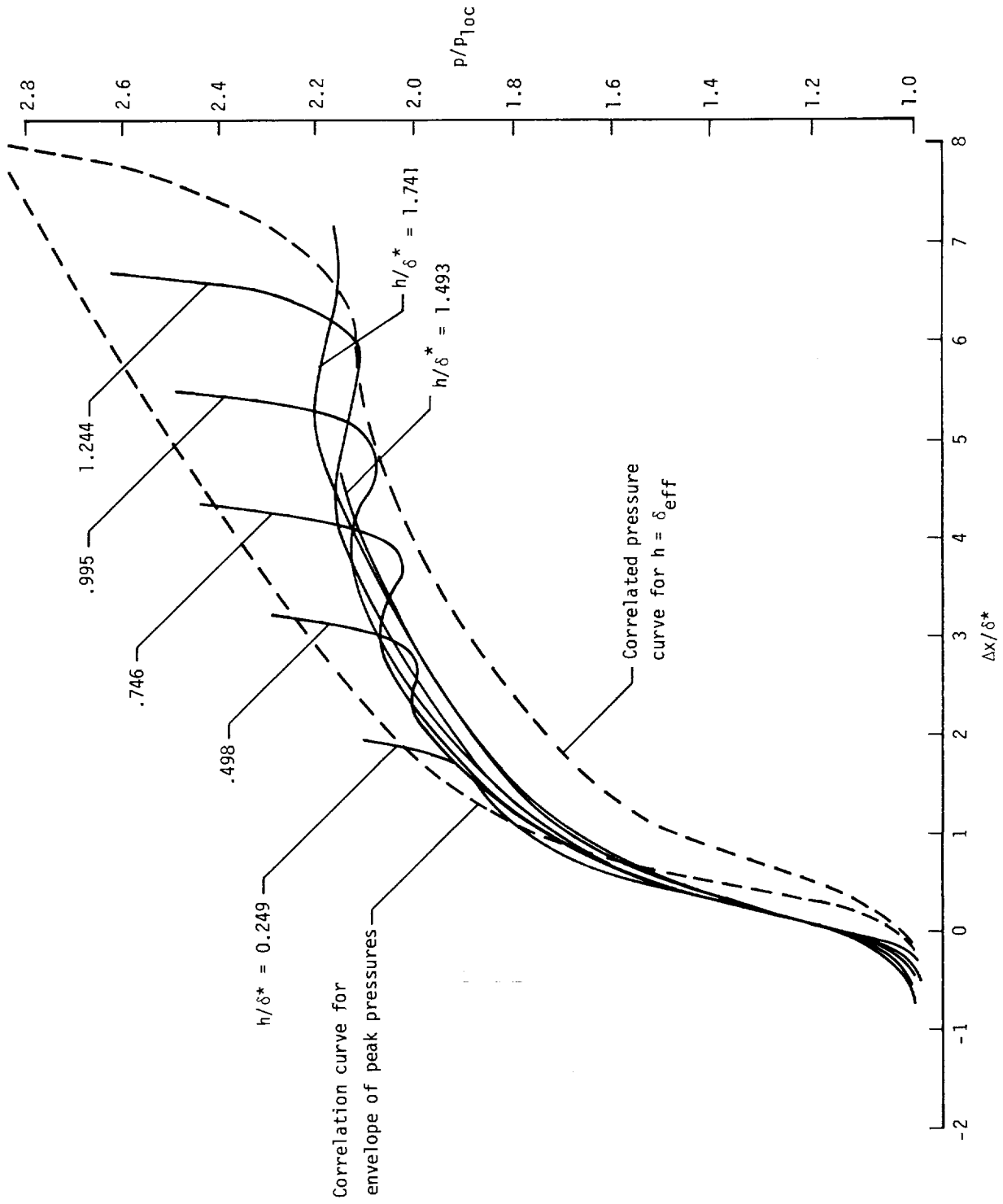
(a) $M_{loc} = 3.85$.

Figure 13.- Comparison of correlation and experimental pressure-profile data for separated flows ahead of forward-facing steps.



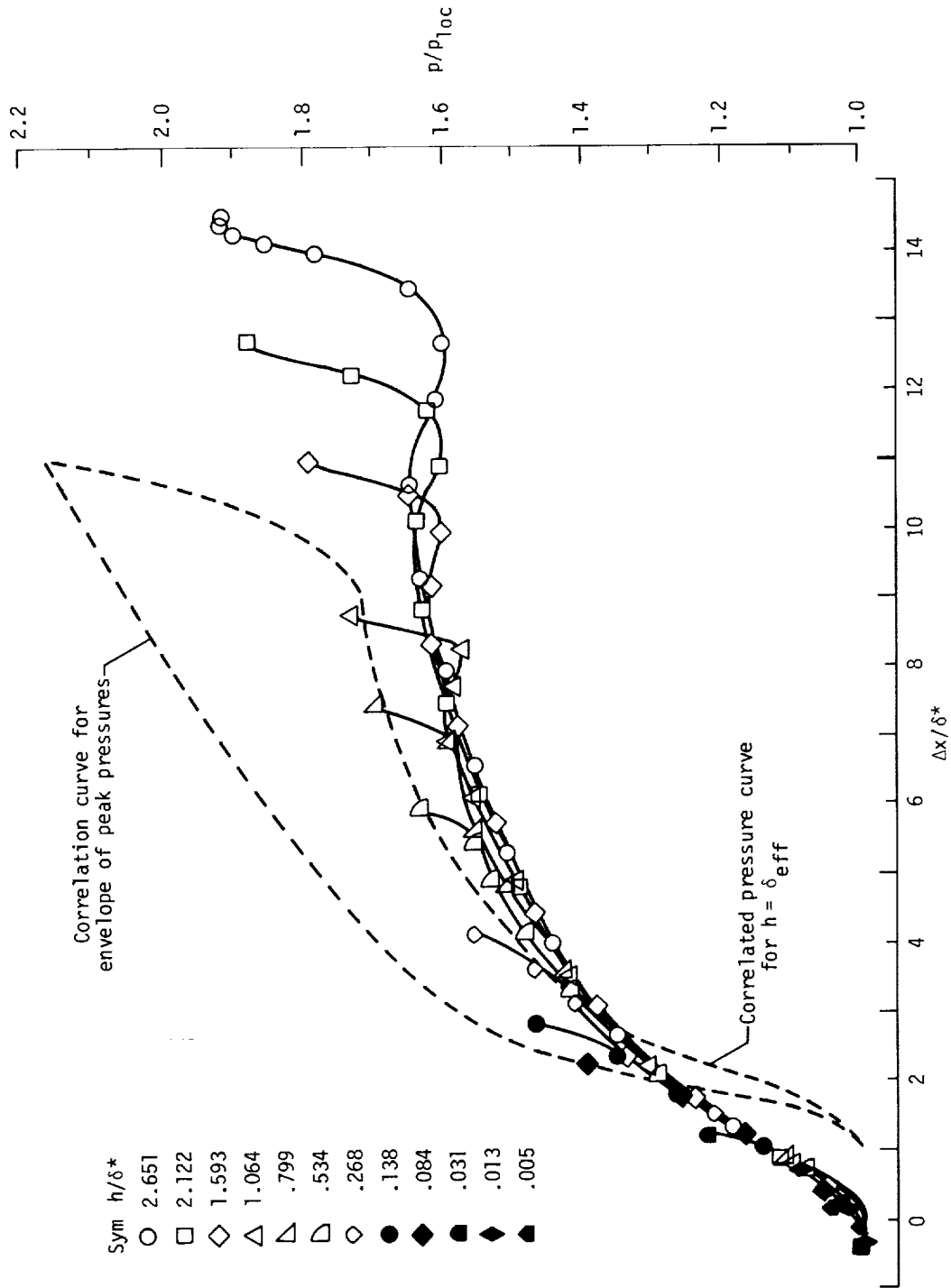
(b) $M_{1loc} = 2.90$.

Figure 13.- Continued.



(c) $M_{1loc} = 2.35$.

Figure 13.- Continued.



(d) $M_{Loc} = 1.61$.

Figure 13.- Concluded.

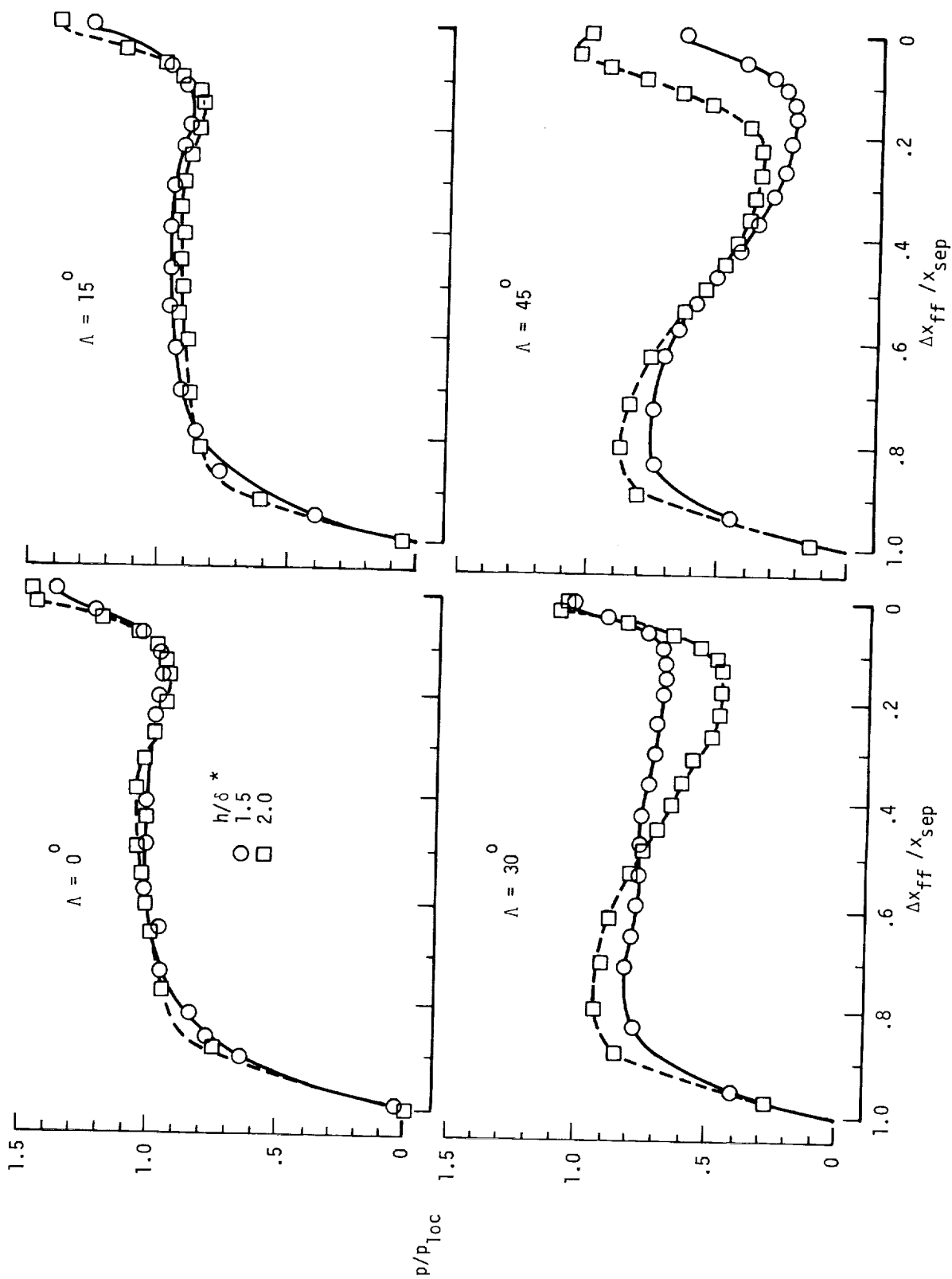


Figure 14.- Separated-flow pressure distributions for yawed forward-facing steps at $M_{loc} = 2.01$.

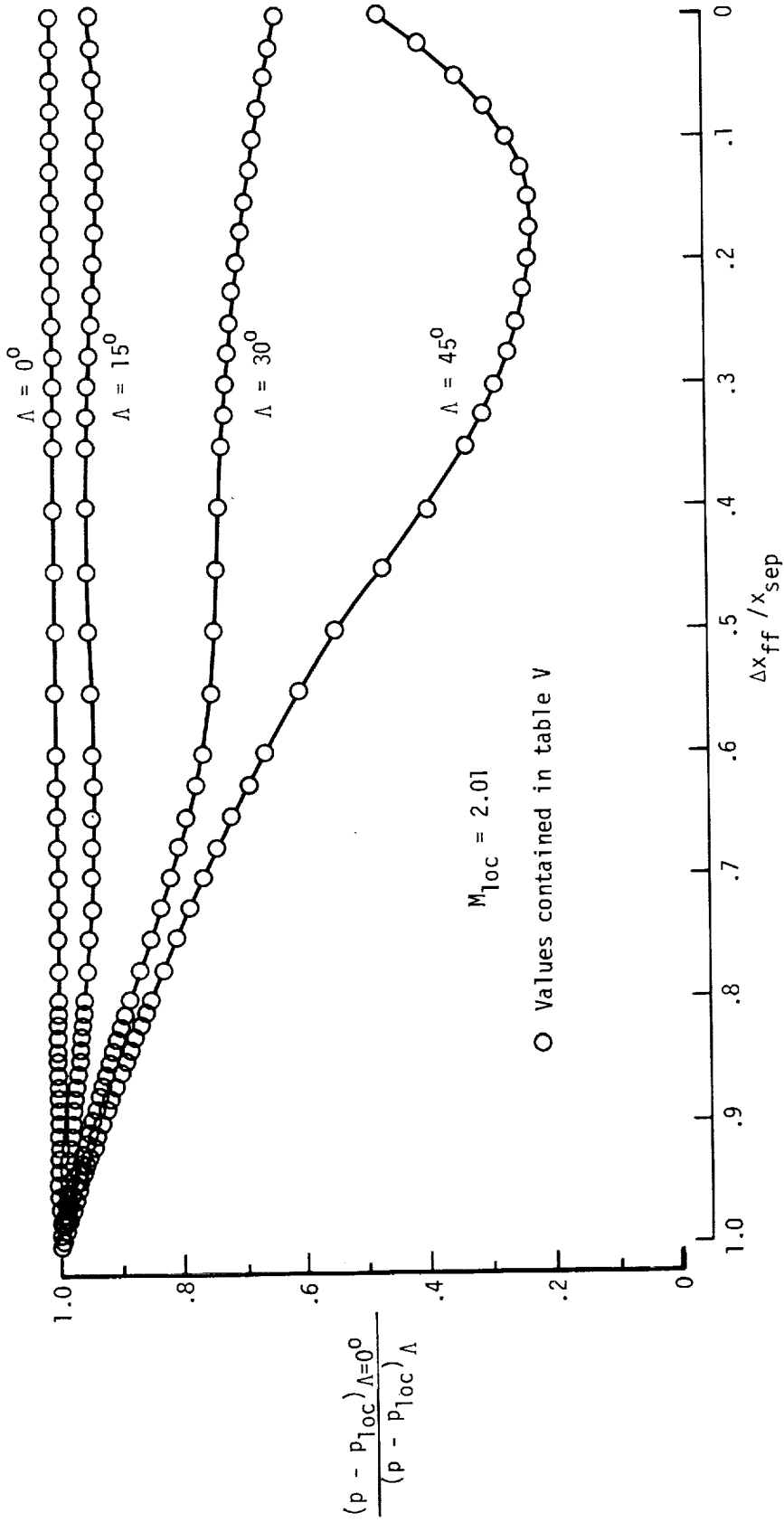


Figure 15.- Ratios of pressure for swept forward-facing steps to separated flow ahead of unswept forward-facing steps.

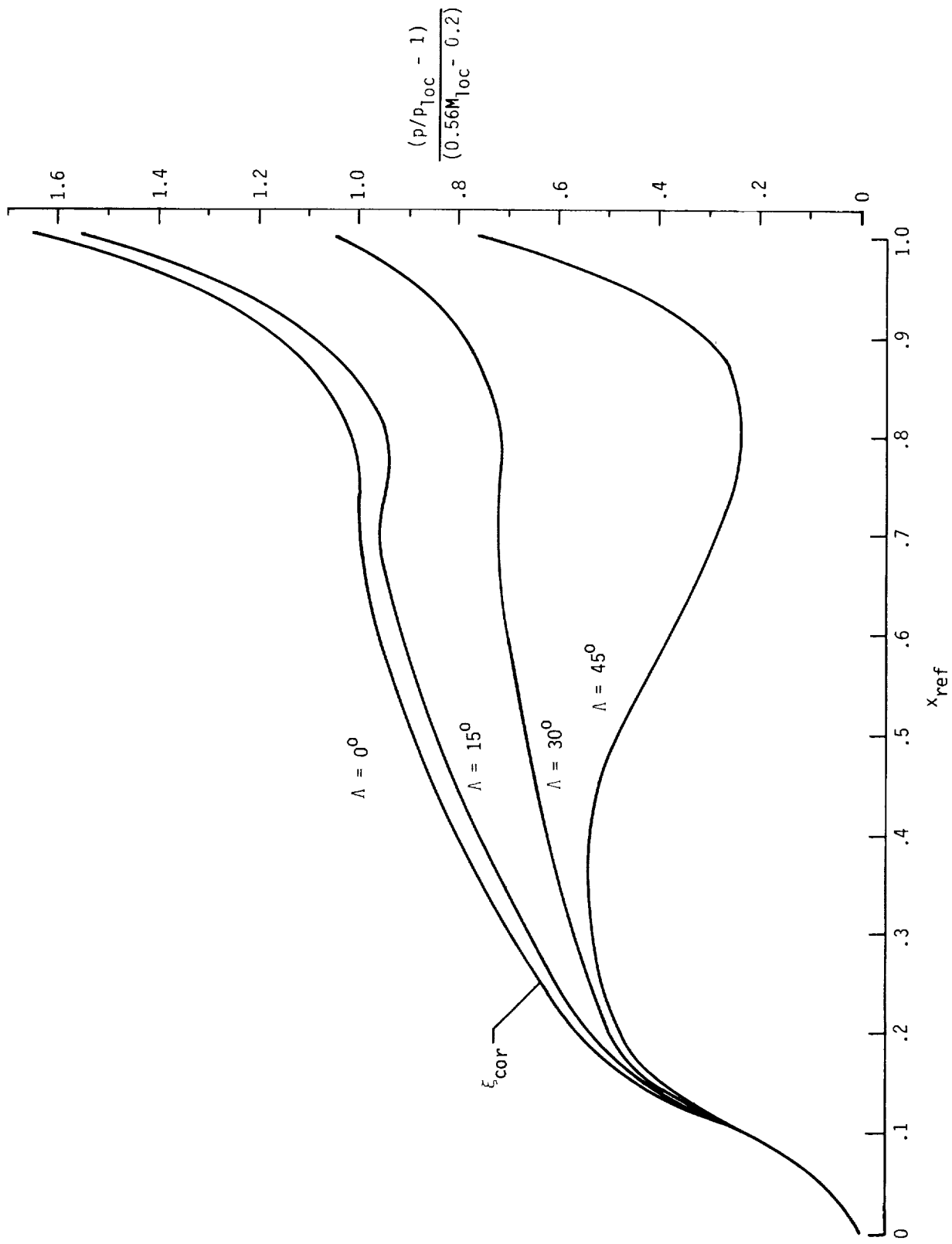


Figure 16.- Correlations of separated-flow pressure distributions ahead of unswept and swept forward-facing steps.

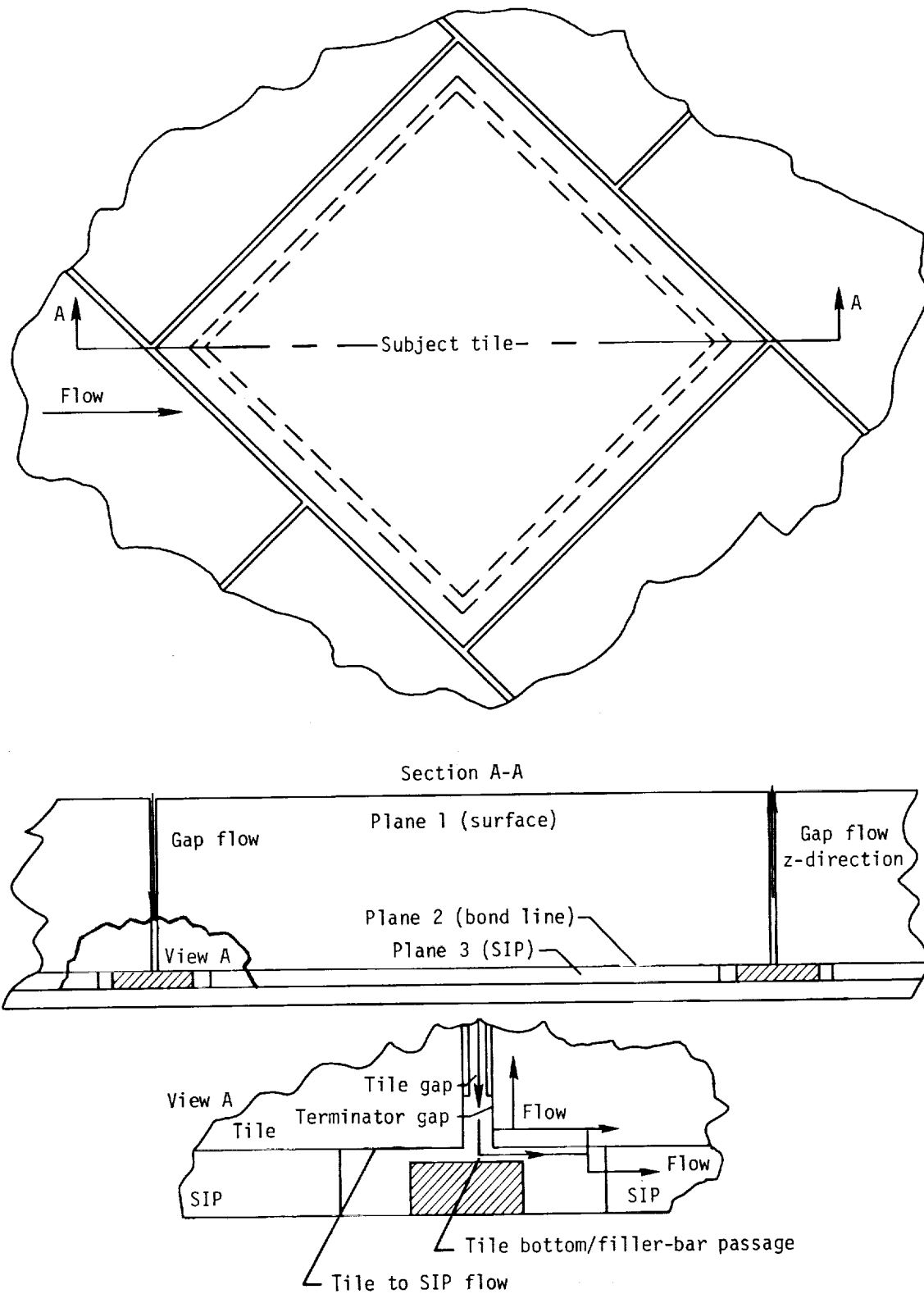


Figure 17.- Shuttle single-tile flow model.

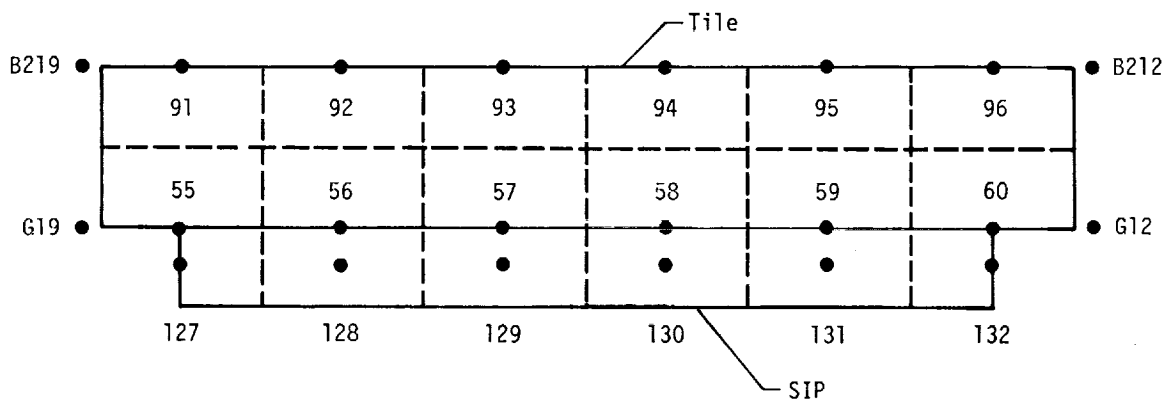
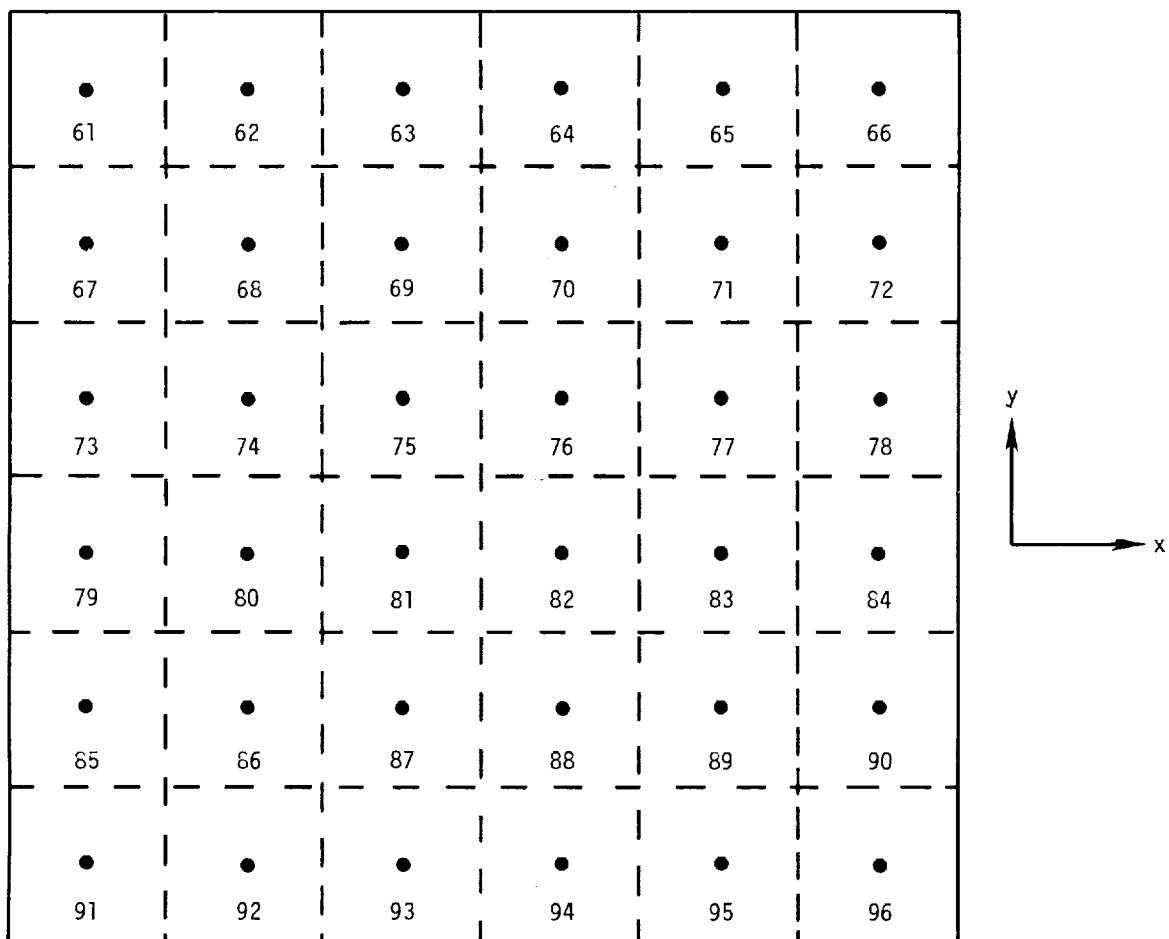


Figure 18.- Subject tile showing nodes inside tile at surface (flow model).

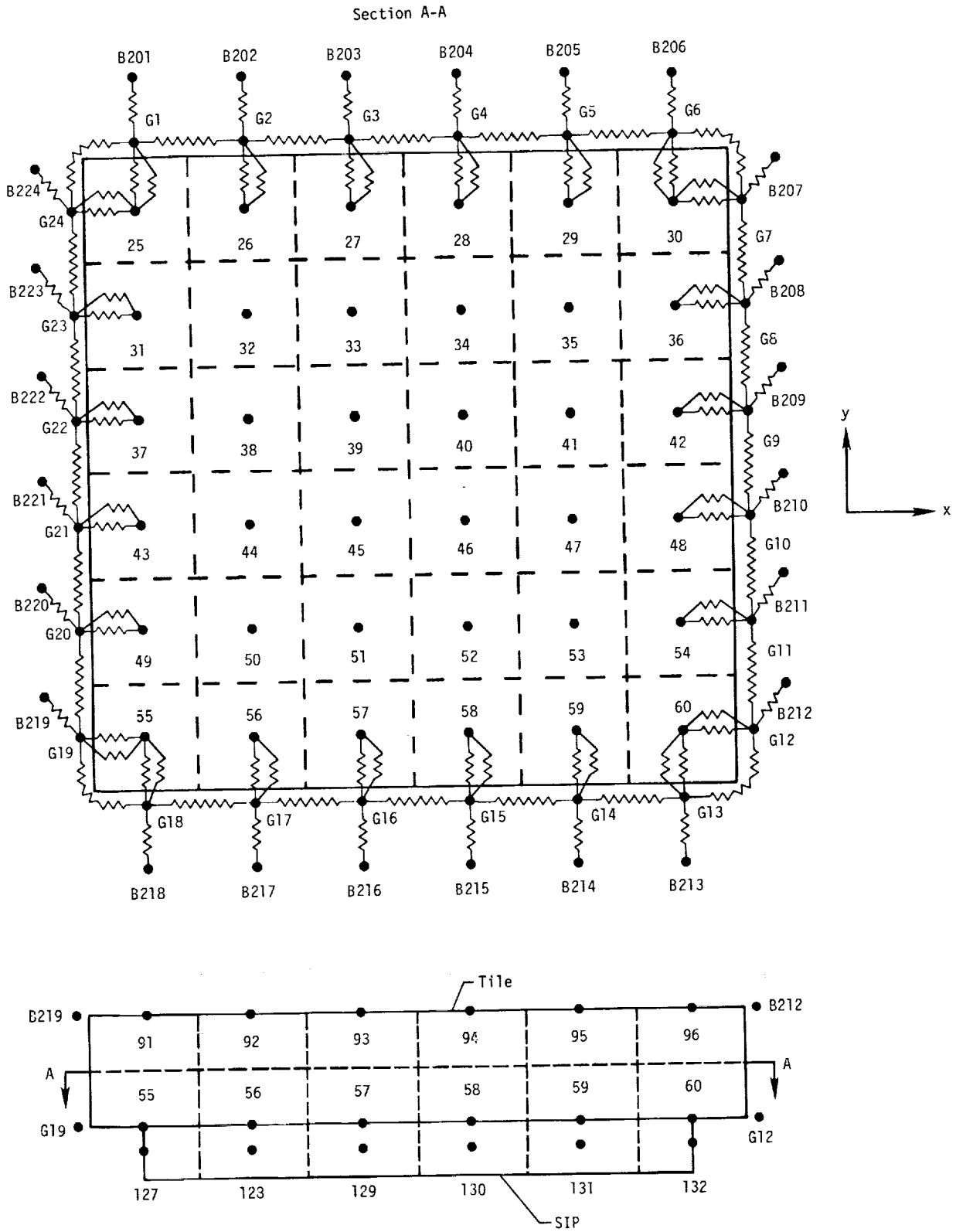


Figure 19.- Subject tile showing nodes at tile bond line (flow model).

Section A-A

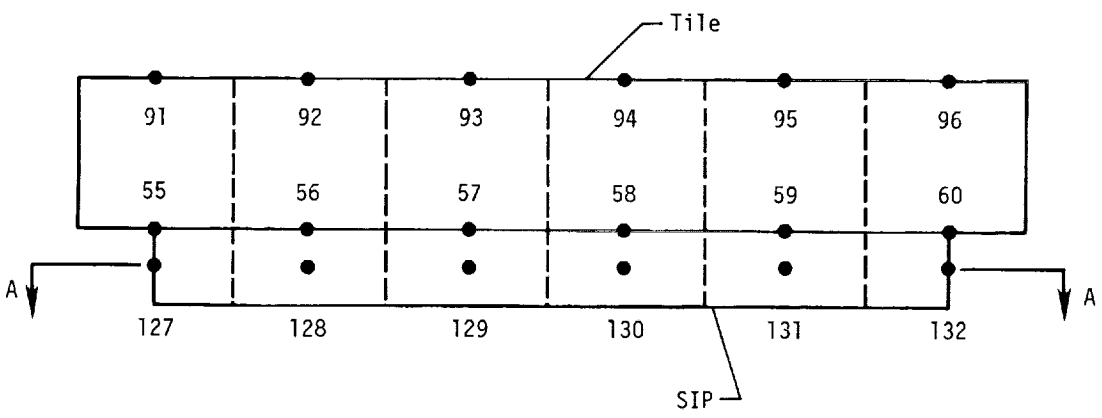
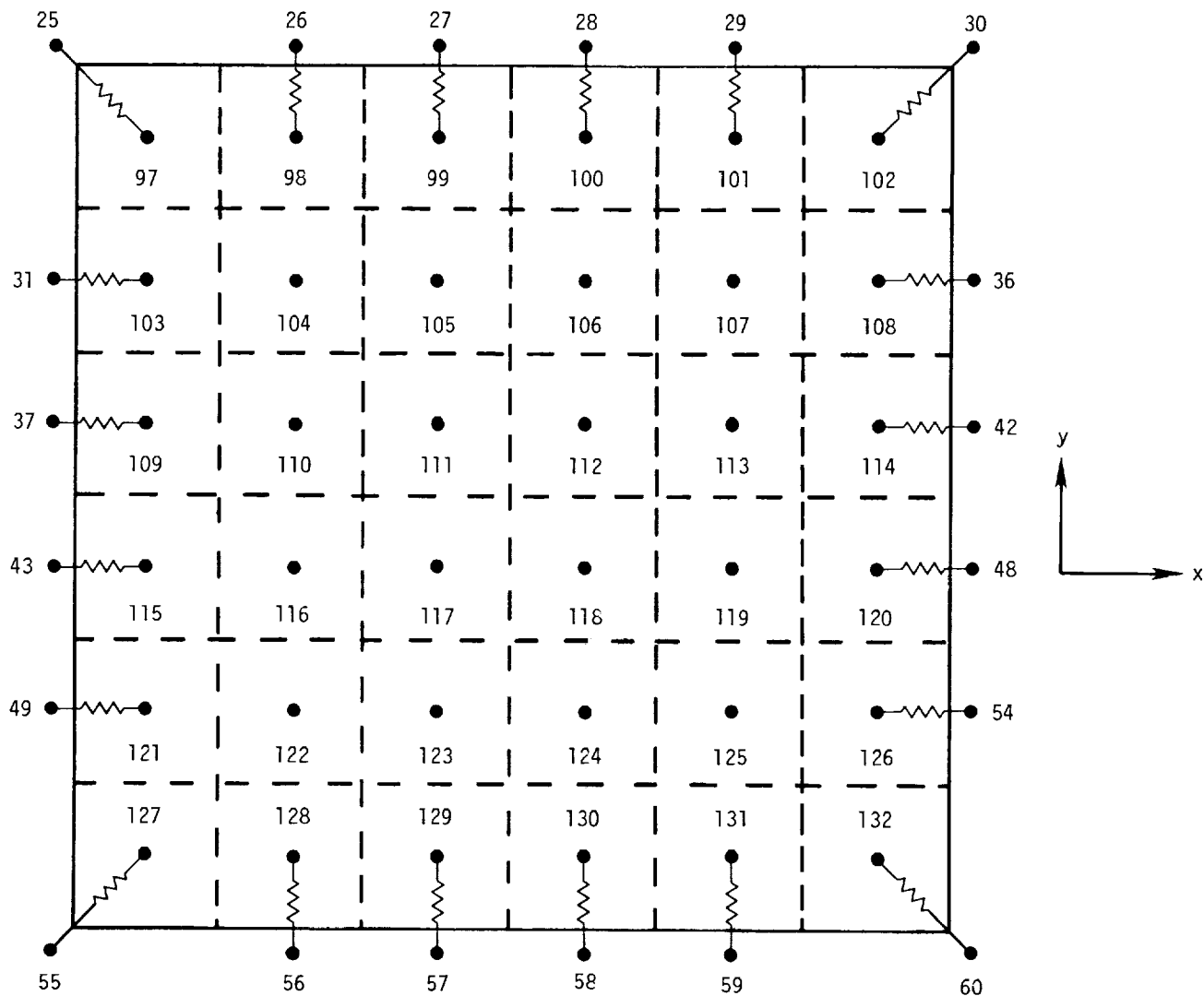


Figure 20.- Subject tile showing nodes in SIP (flow model).

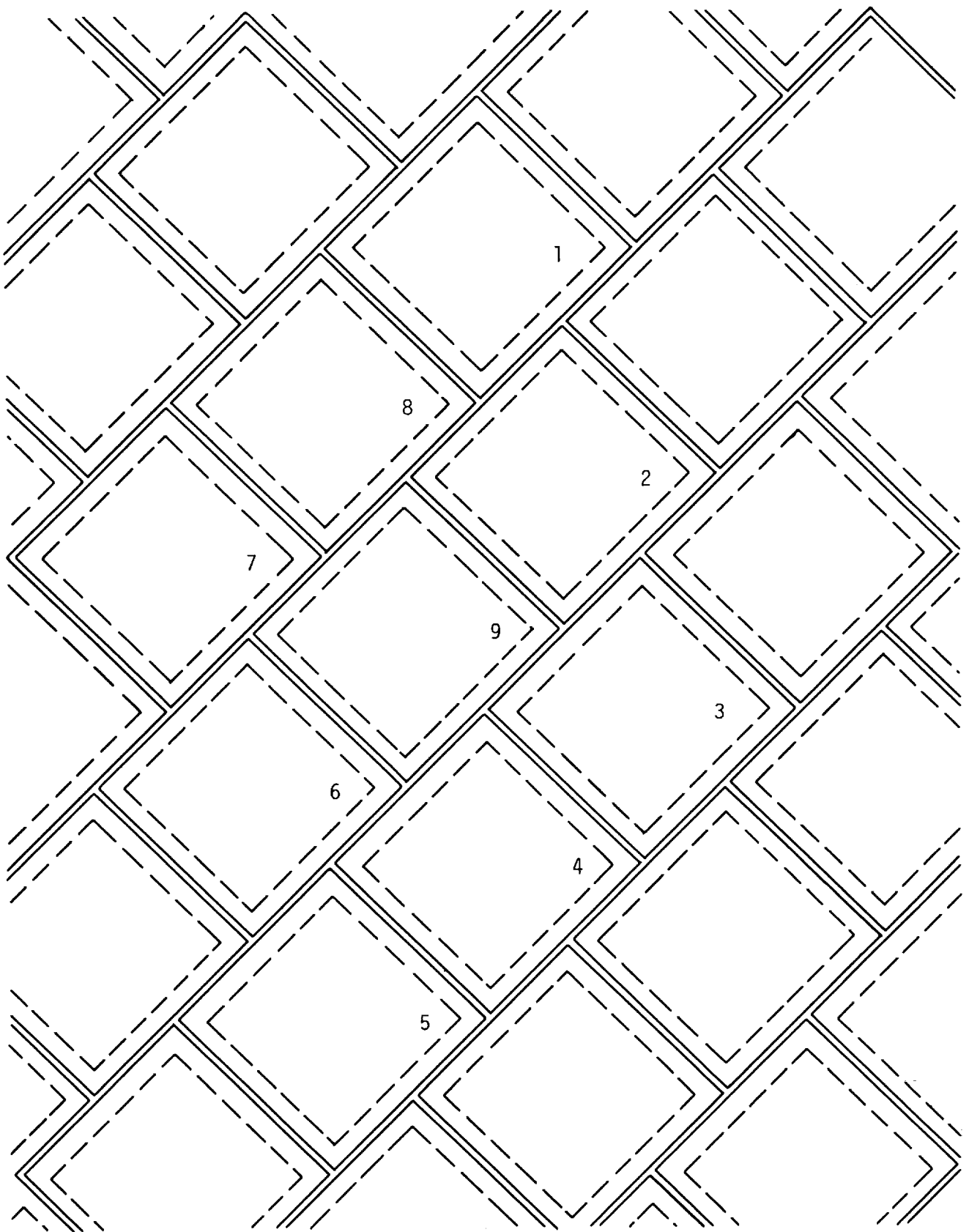


Figure 21.- Nine-tile array (flow model).

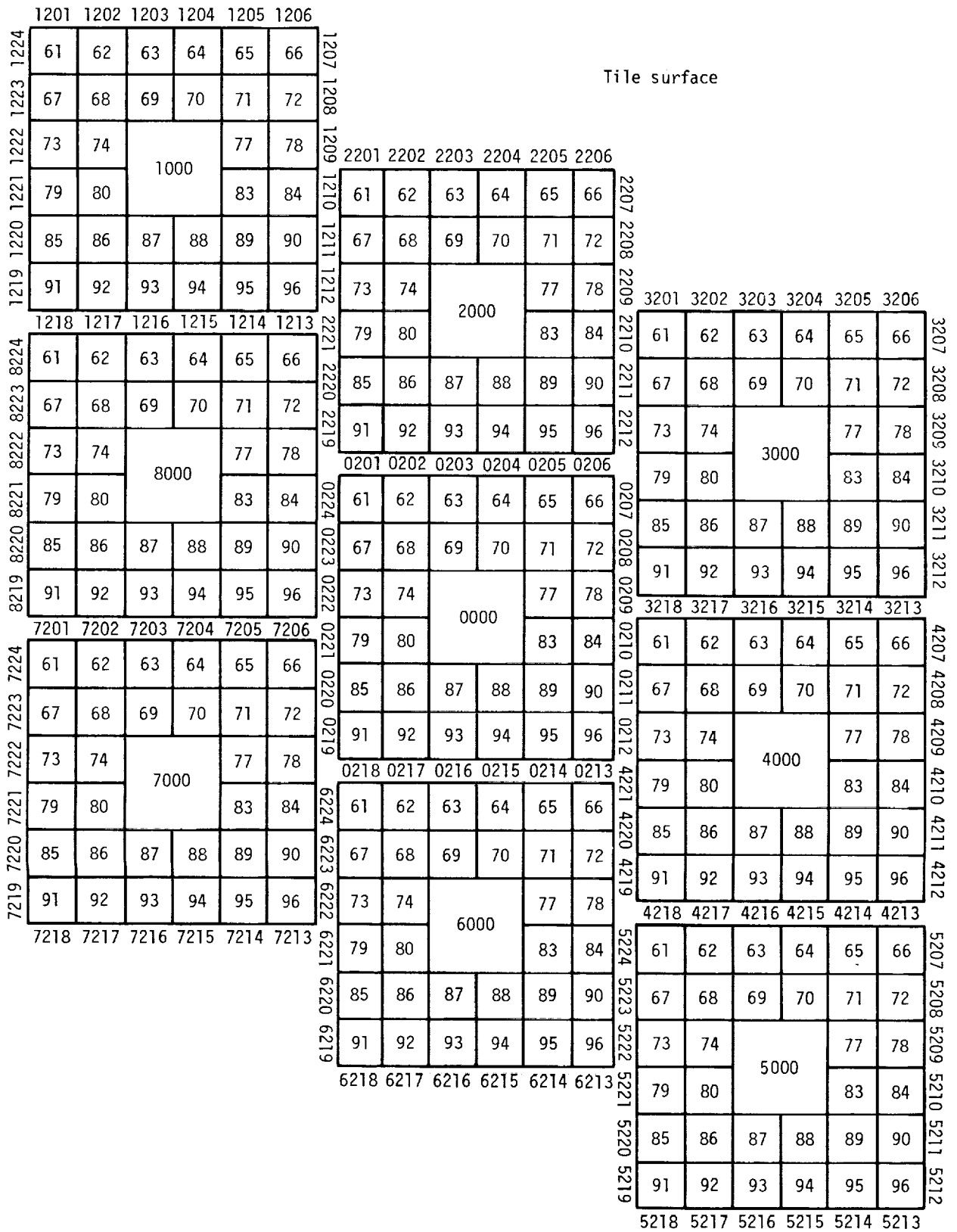


Figure 22.- Tile array showing surface nodes (flow model).

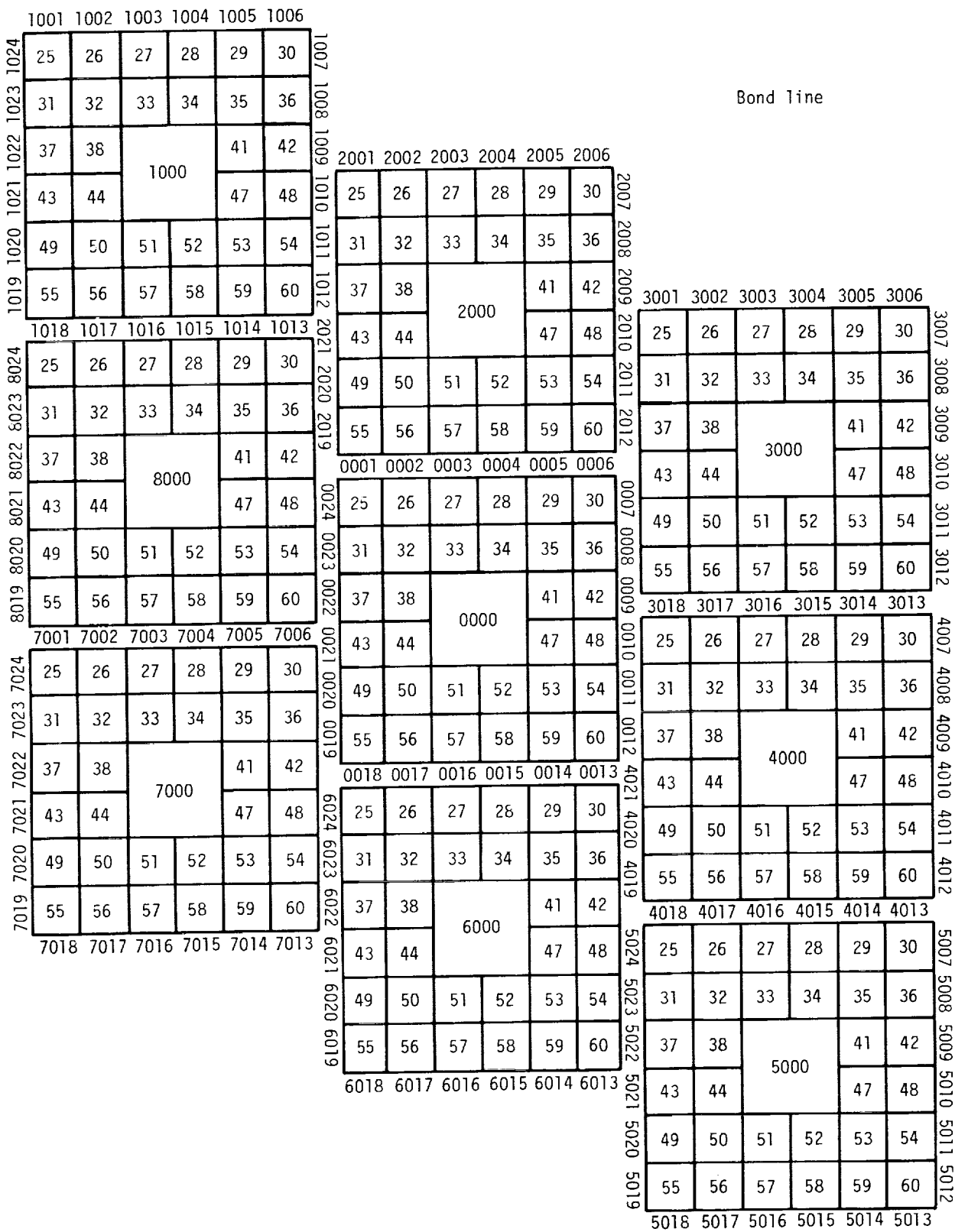


Figure 23.- Tile array showing bond-line nodes (flow model).

97	98	99	100	101	102
103	104	105	106	107	108
109	110	1000		113	114
115	116	1000		119	120
121	122	123	124	125	126
127	128	129	130	131	132

SIP

97	98	99	100	101	102
103	104	105	106	107	108
109	110	2000		113	114
115	116	2000		119	120
121	122	123	124	125	126
127	128	129	130	131	132

97	98	99	100	101	102
103	104	105	106	107	108
109	110	8000		113	114
115	116	8000		119	120
121	122	123	124	125	126
127	128	129	130	131	132

97	98	99	100	101	102
103	104	105	106	107	108
109	110	3000		113	114
115	116	3000		119	120
121	122	123	124	125	126
127	128	129	130	131	132

97	98	99	100	101	102
103	104	105	106	107	108
109	110	0000		113	114
115	116	0000		119	120
121	122	123	124	125	126
127	128	129	130	131	132

97	98	99	100	101	102
103	104	105	106	107	108
109	110	4000		113	114
115	116	4000		119	120
121	122	123	124	125	126
127	128	129	130	131	132

97	98	99	100	101	102
103	104	105	106	107	108
109	110	7000		113	114
115	116	7000		119	120
121	122	123	124	125	126
127	128	129	130	131	132

97	98	99	100	101	102
103	104	105	106	107	108
109	110	6000		113	114
115	116	6000		119	120
121	122	123	124	125	126
127	128	129	130	131	132

97	98	99	100	101	102
103	104	105	106	107	108
109	110	5000		113	114
115	116	5000		119	120
121	122	123	124	125	126
127	128	129	130	131	132

Figure 24.- Tile array showing SIP nodes (flow model).

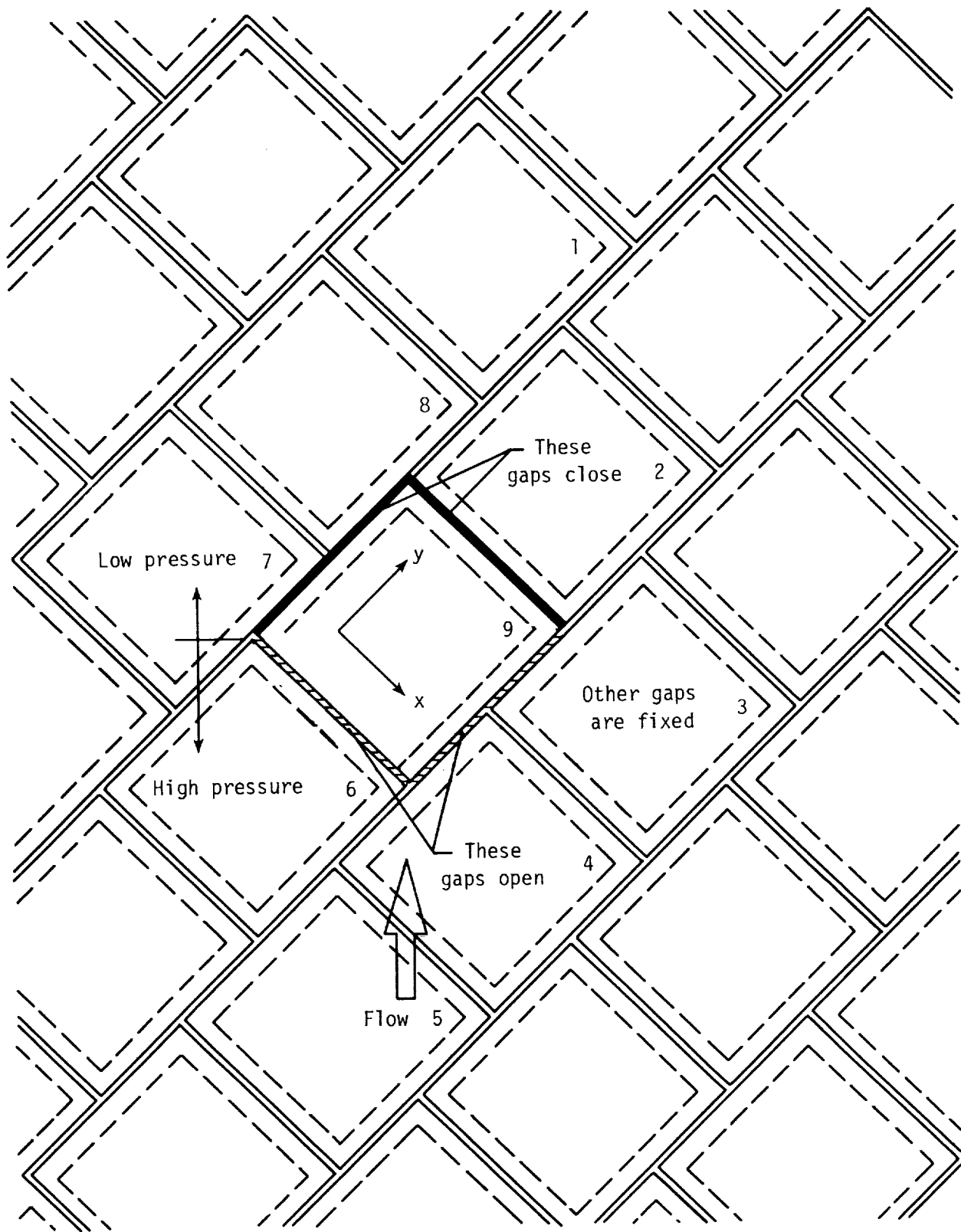


Figure 25.- Nine-tile array showing gap changes due to x- and y-deflections of subject tile, tile 9 (flow model).

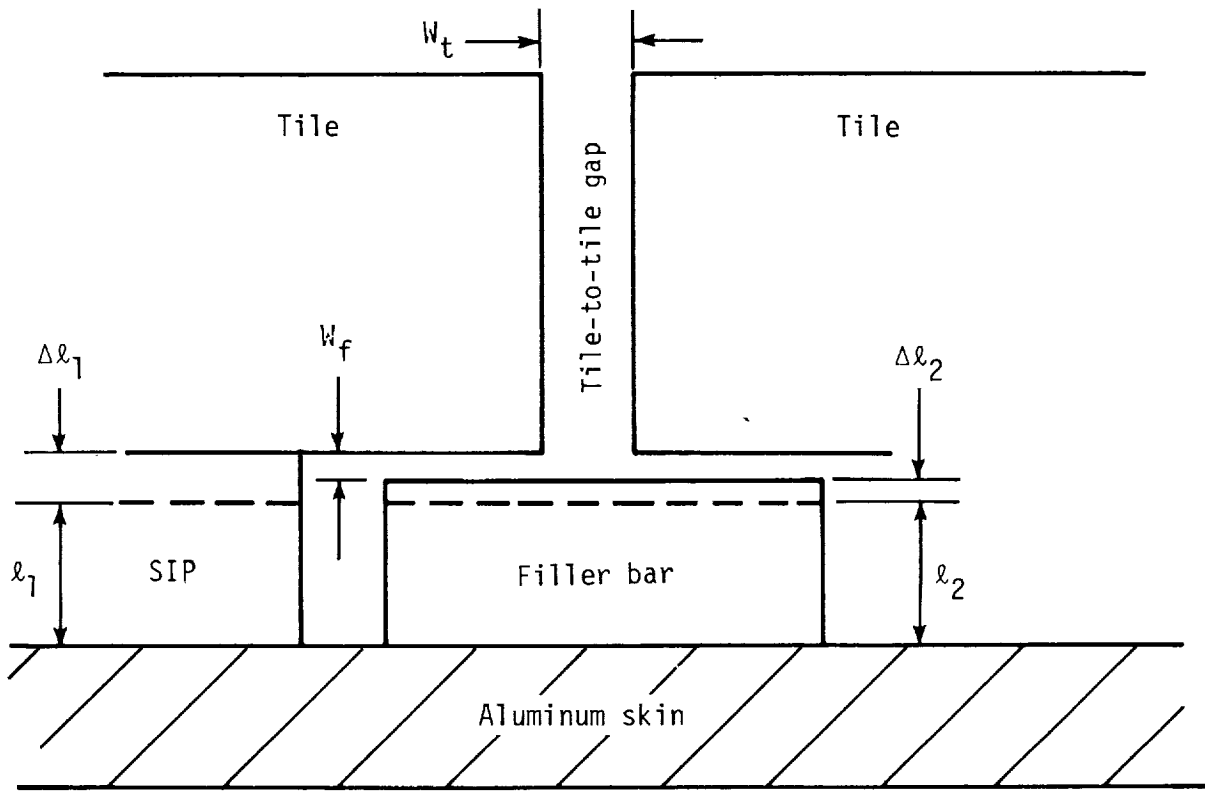


Figure 26.- TPS vertical dimensions and deflections due to pressure loads.

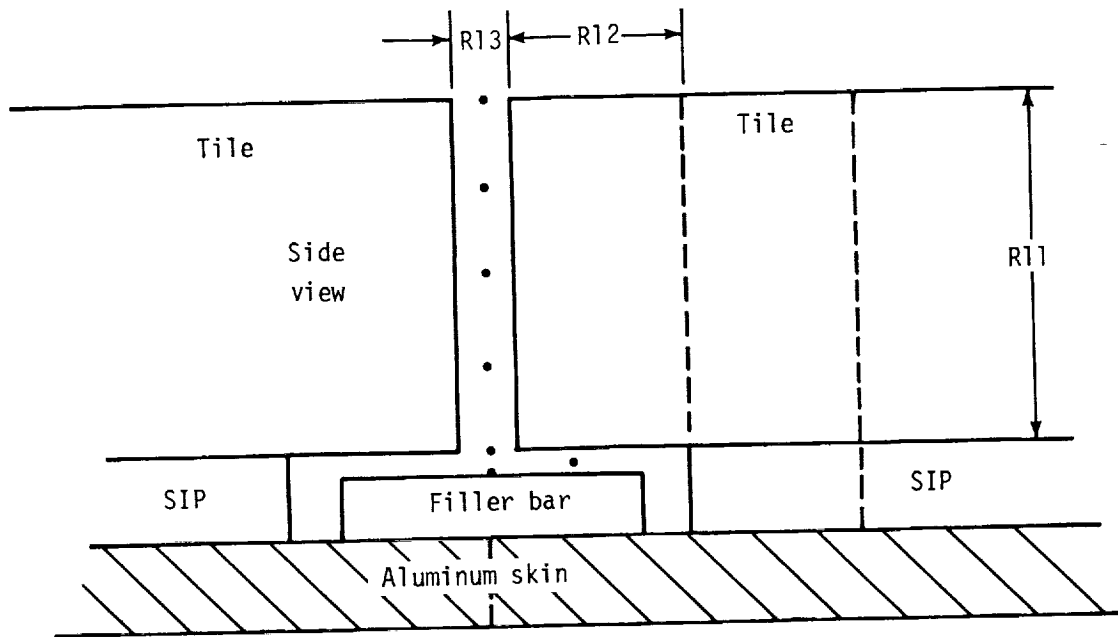
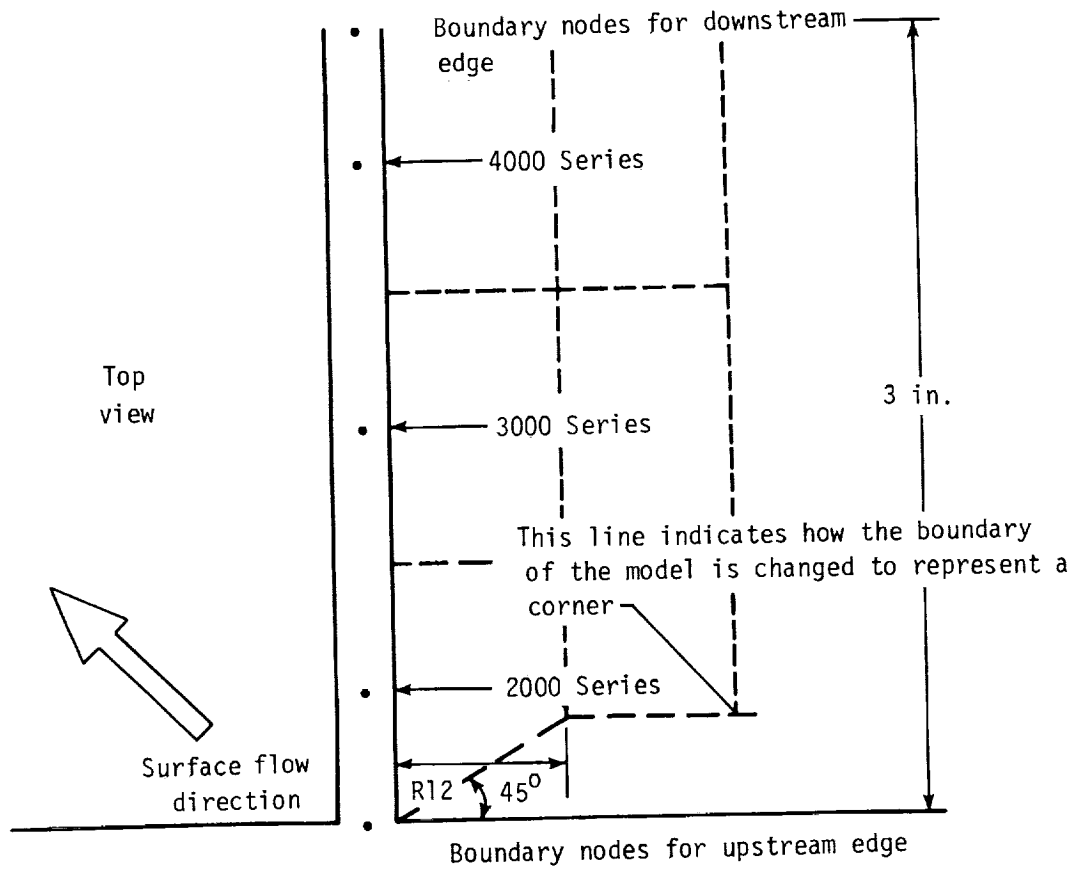


Figure 27.- Top and side views of tile thermal model.

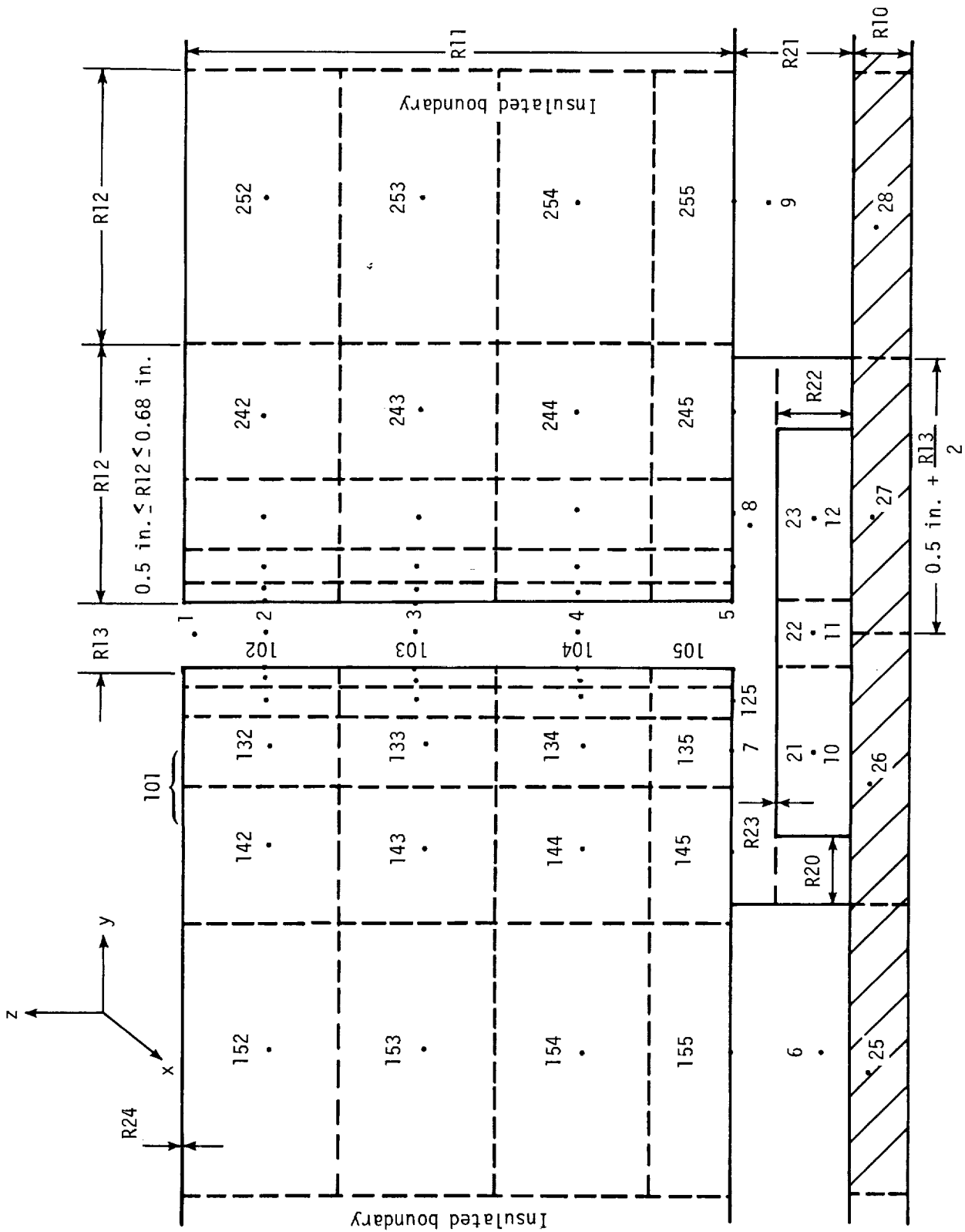
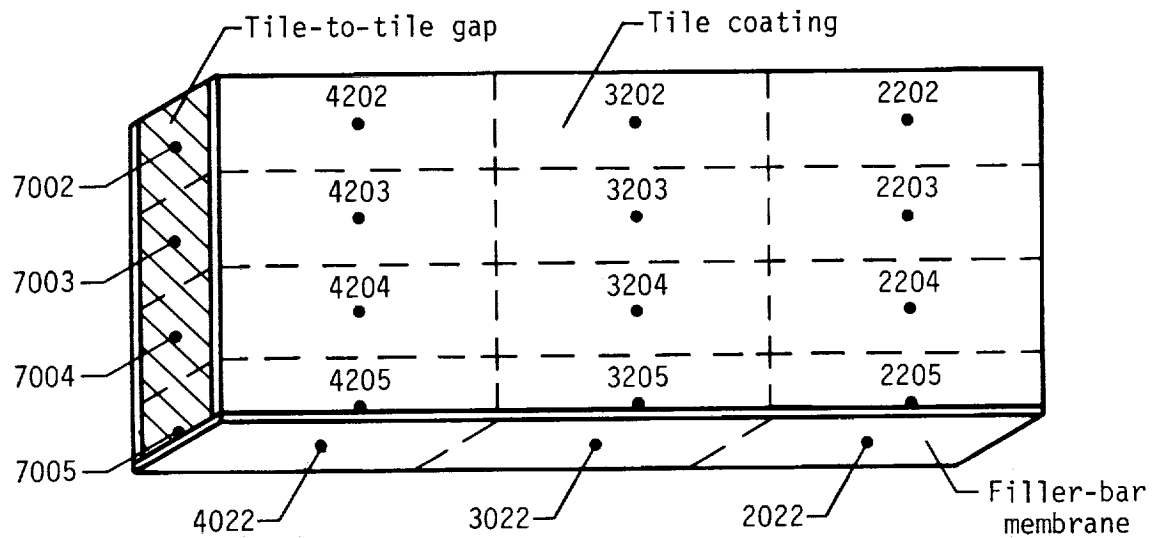
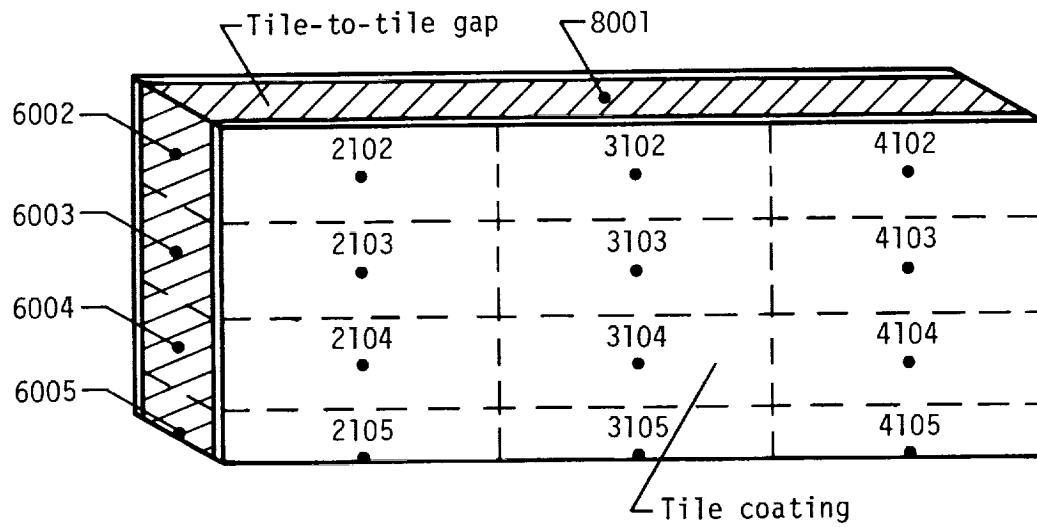


Figure 28.- Enlarged side view of tile thermal model.



Boundary conditions

$$T_{8001} = -460^{\circ}\text{F}$$

$$T_{6002} = T_{2102}$$

$$T_{7002} = T_{4102}$$

$$T_{6003} = T_{2103}$$

$$T_{7003} = T_{4103}$$

$$T_{6004} = T_{2104}$$

$$T_{7004} = T_{4104}$$

$$T_{6005} = T_{2105}$$

$$T_{7005} = T_{4105}$$

Figure 29.- Radiation in gap.

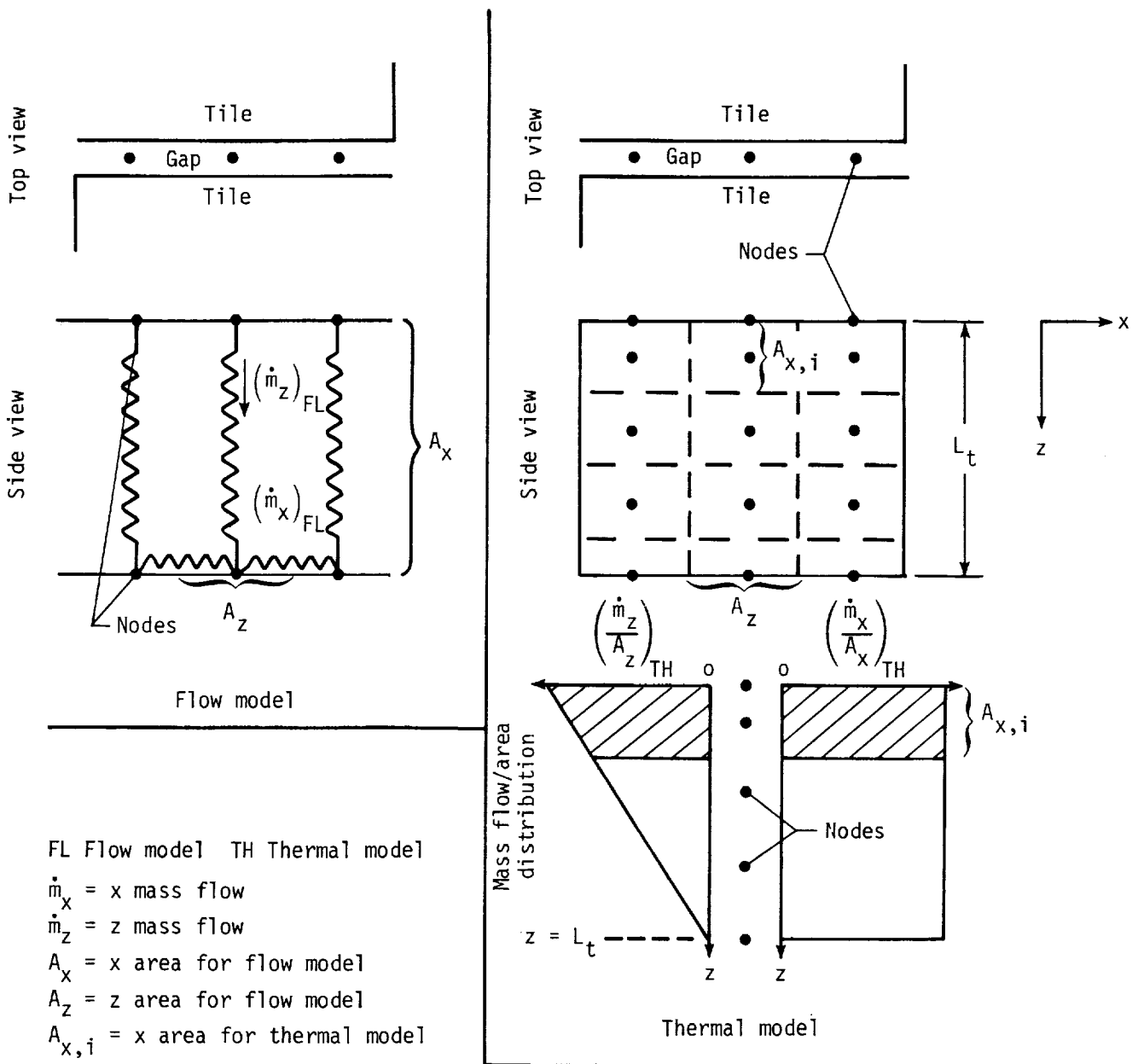
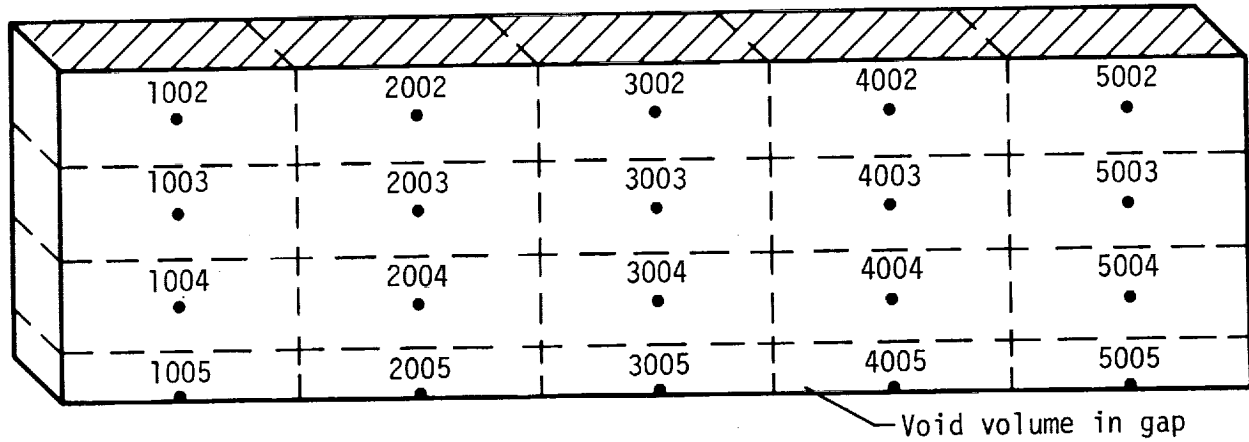


Figure 30.- Mass flow per unit area in gap.

Node 1 at surface



Boundary conditions

T_1 = gas inlet temperature

$$\begin{aligned} T_{1002} &= T_{3002} & T_{5002} &= T_{3002} \\ T_{1003} &= T_{3003} & T_{5003} &= T_{3003} \\ T_{1004} &= T_{3004} & T_{5004} &= T_{3004} \\ T_{1005} &= T_{3005} & T_{5005} &= T_{3005} \end{aligned}$$

Figure 31.- Control volume nodes for mass transfer in gap.

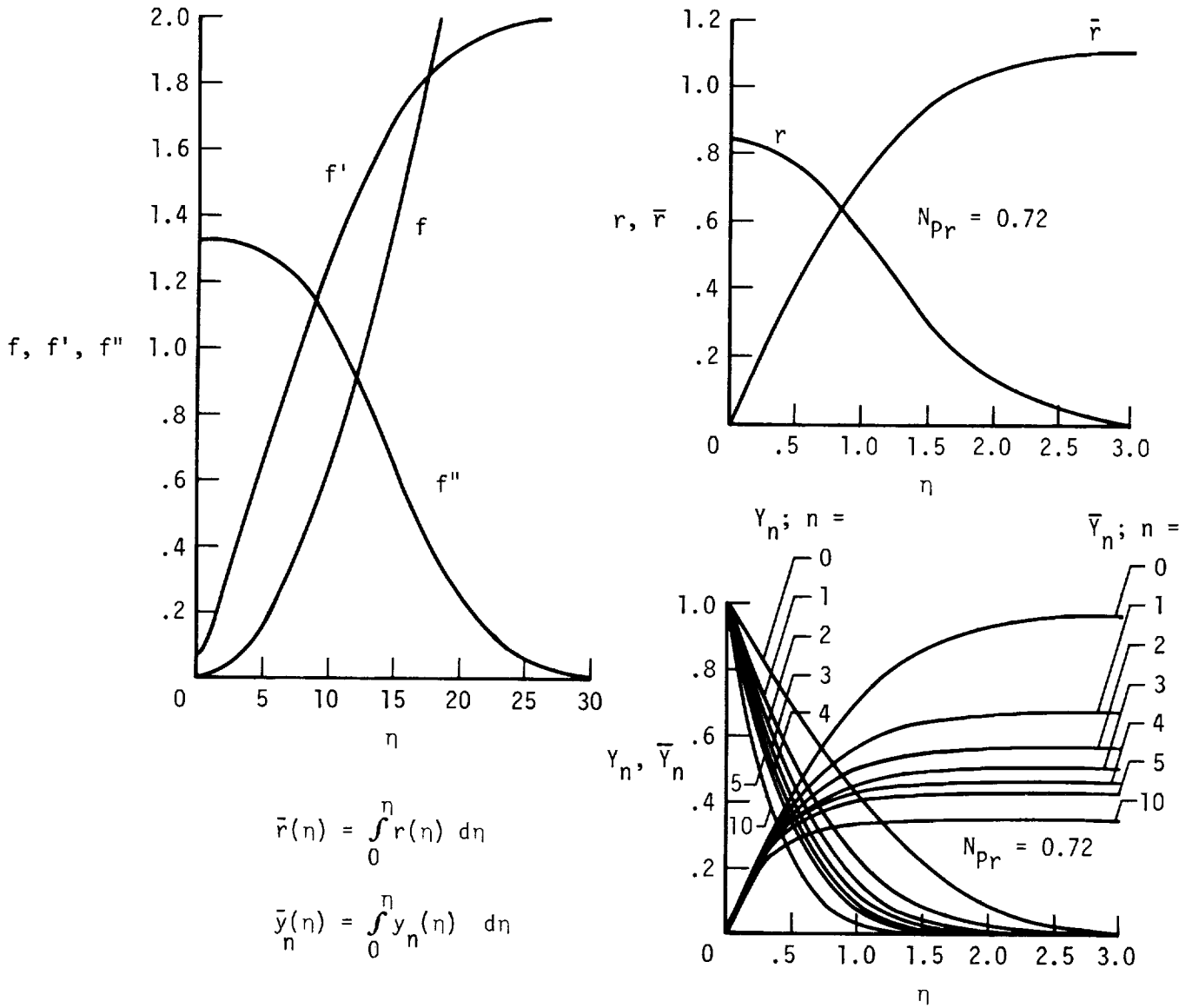


Figure 32.- Parameters used in determining temperature distribution in a laminar boundary layer. (From ref. 22.)

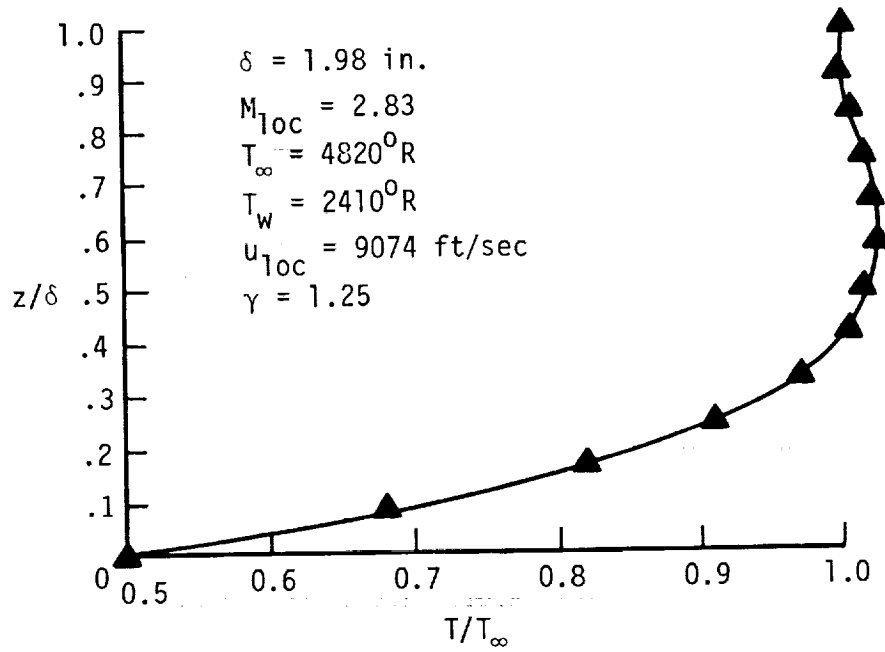
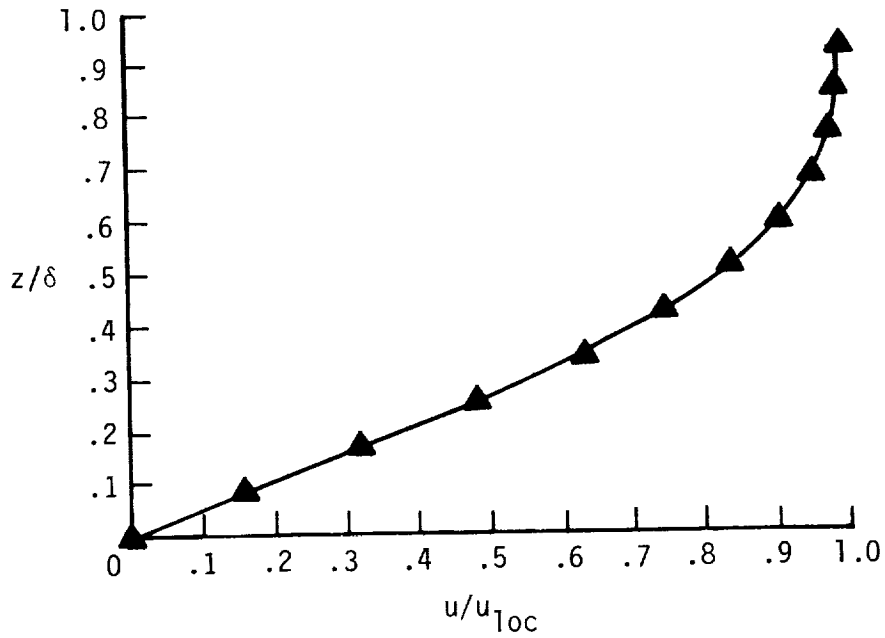


Figure 33.- Velocity and temperature distributions in laminar boundary layer on orbiter fuselage at location $X = 750 \text{ in.}$, $Y = -75 \text{ in.}$

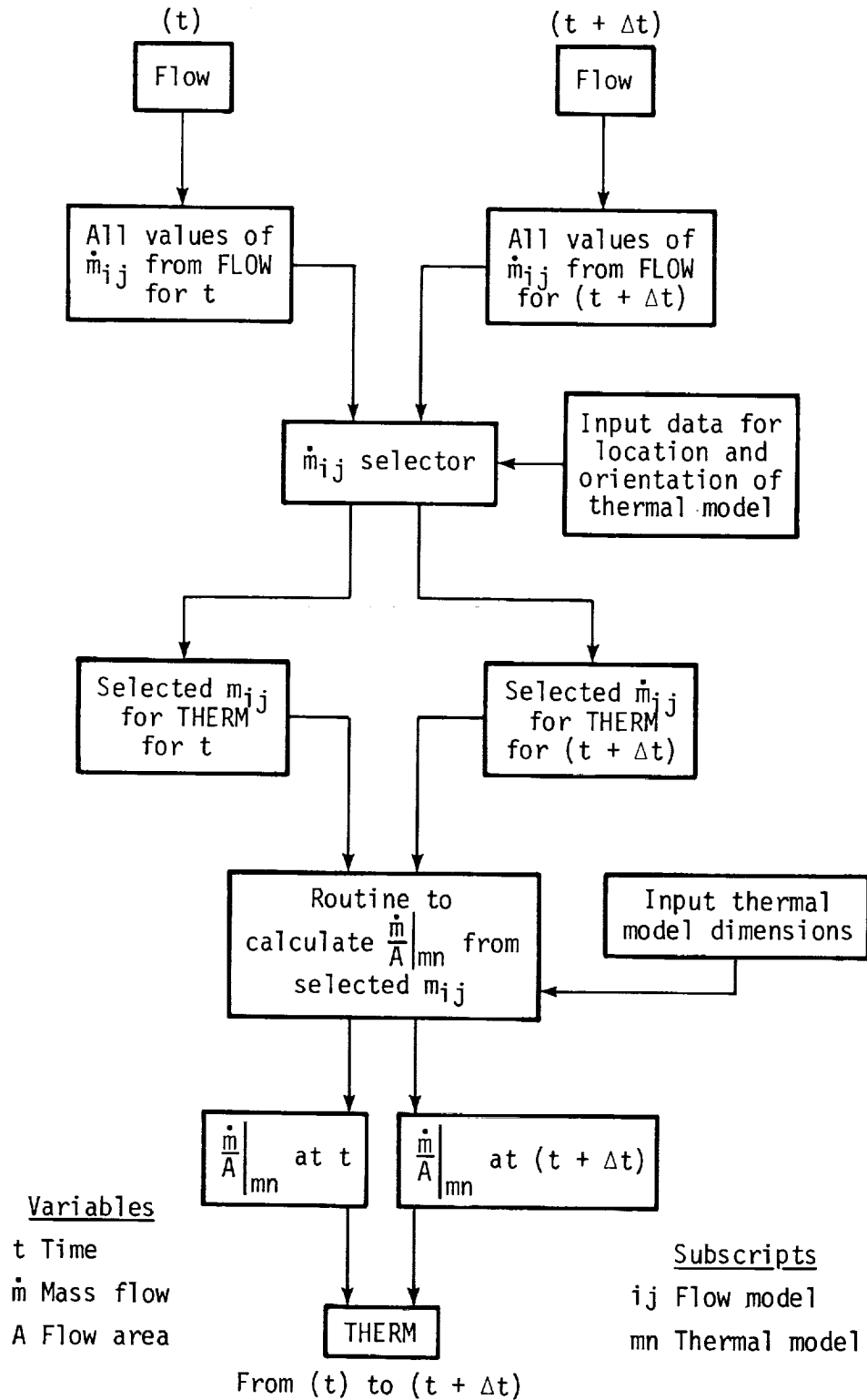
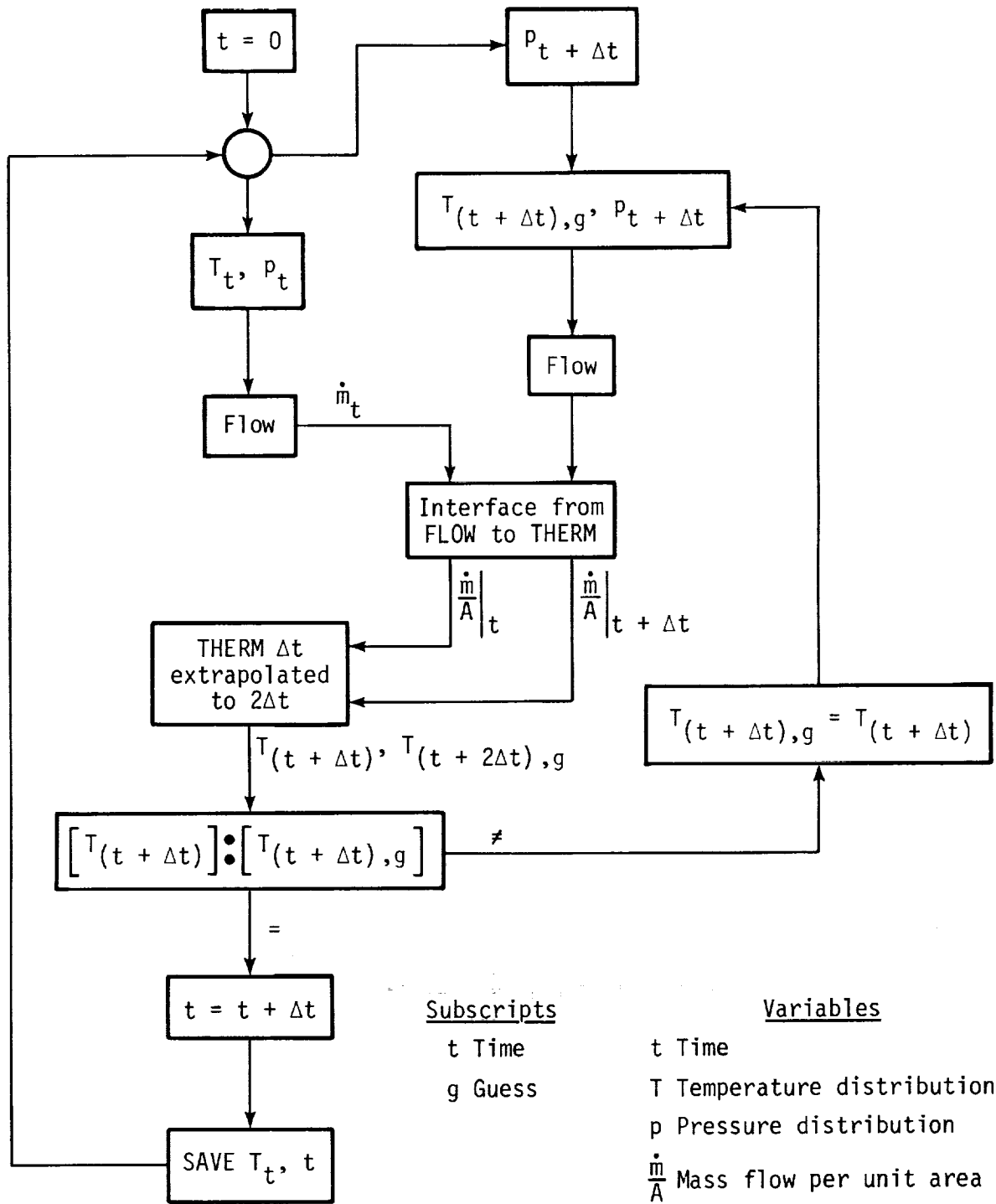


Figure 34.- Flow chart for interface from FLOW to THERM.



<u>Subscripts</u>	<u>Variables</u>
t Time	t Time
g Guess	T Temperature distribution
	p Pressure distribution
	$\frac{\dot{m}}{A}$ Mass flow per unit area

Figure 35.- Flow chart of run stream.

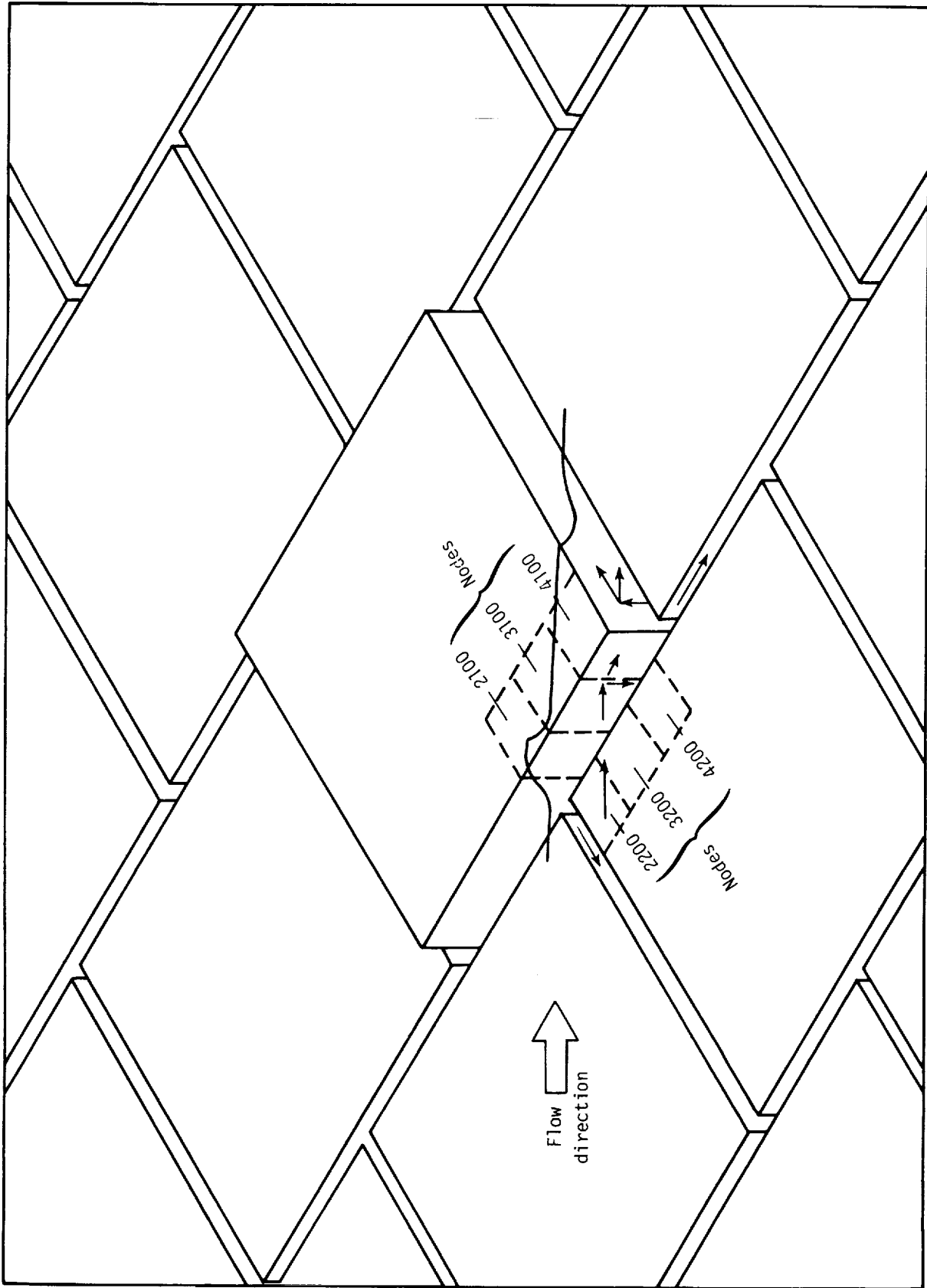


Figure 36.- Location of thermal model boundaries.

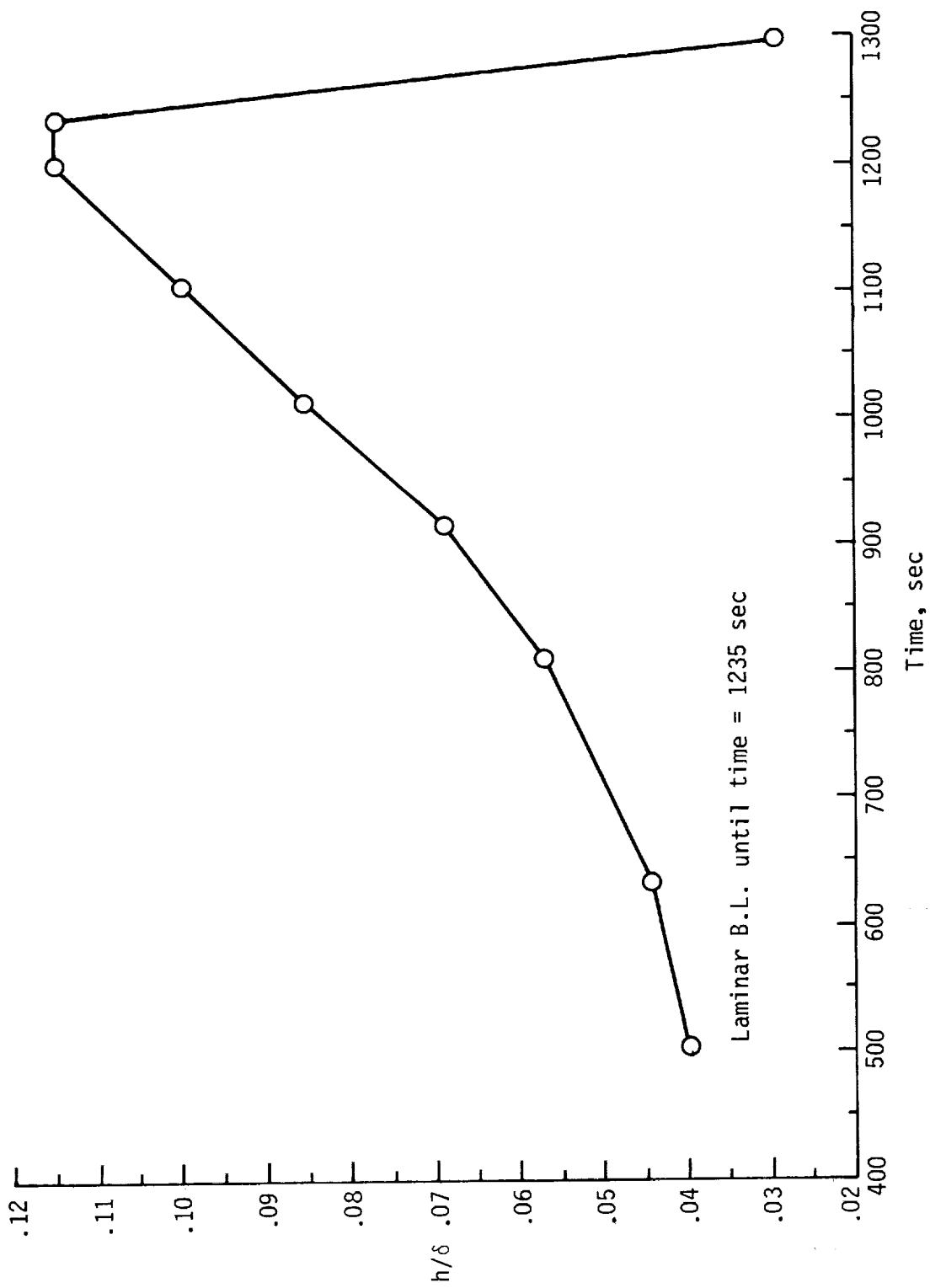


Figure 37.- Ratio of step height to boundary-layer thickness at fuselage location for 0.1-in. step.

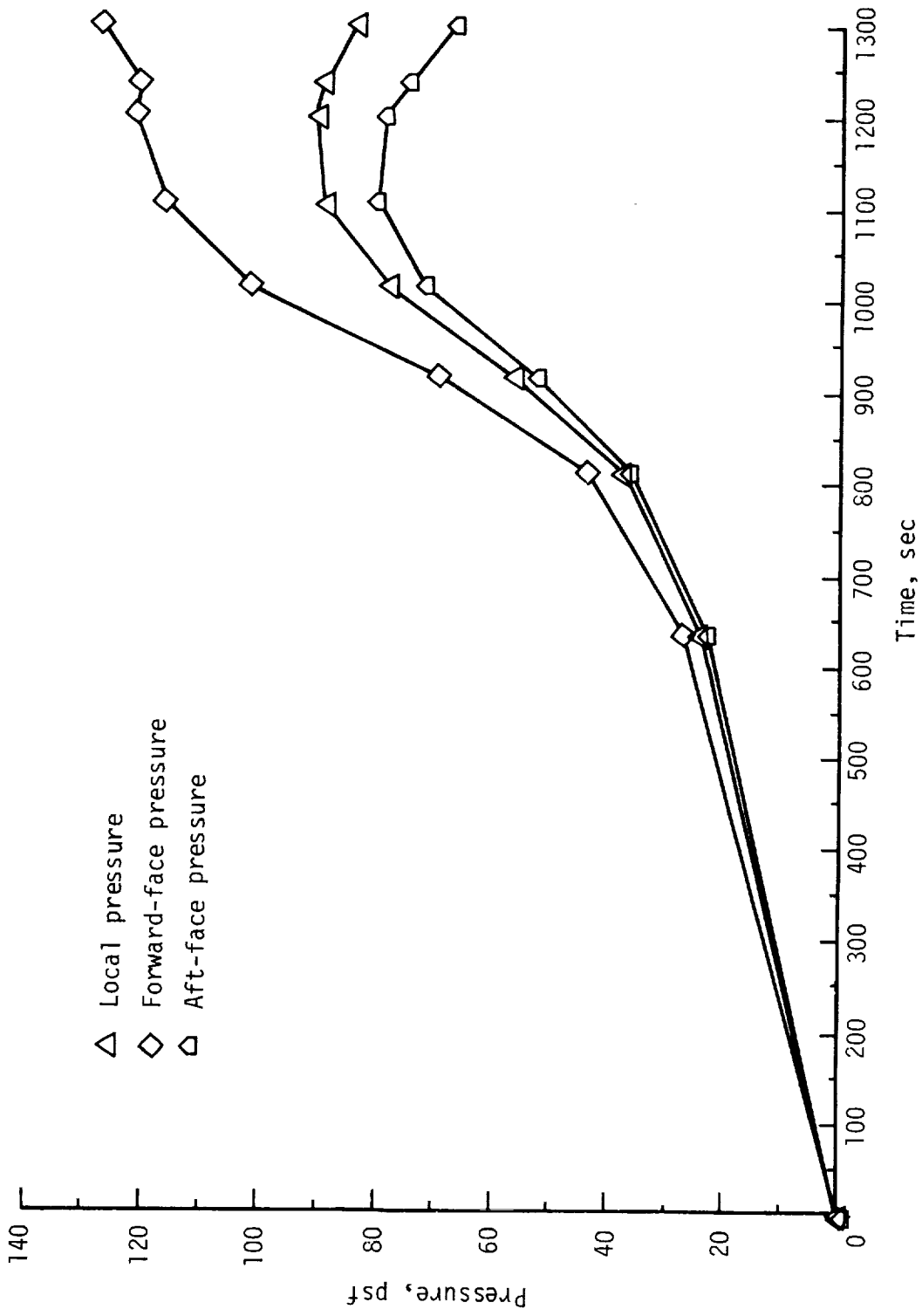


Figure 38.- Pressures at fuselage location for 0.1-in. step.

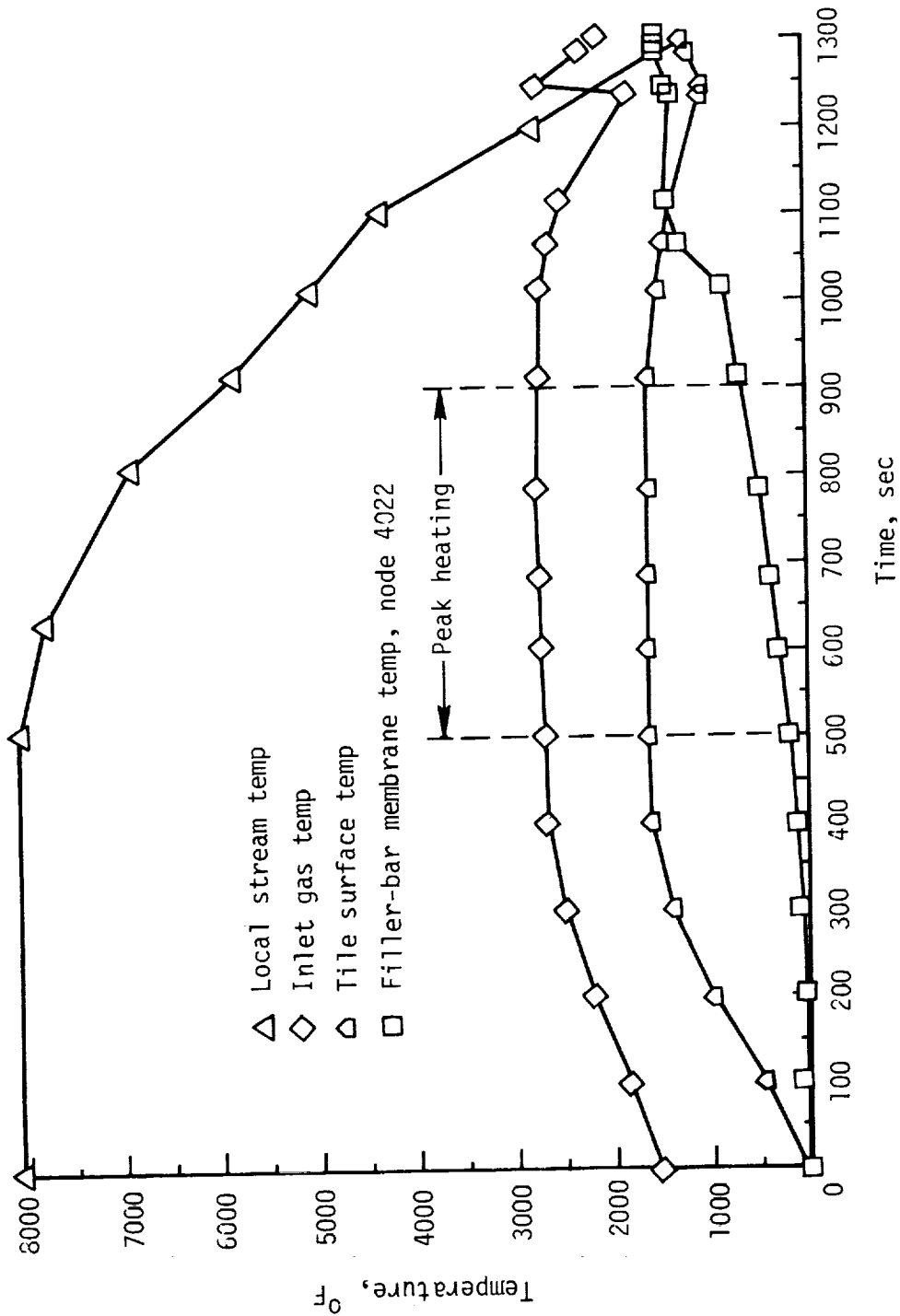


Figure 39.- Gap temperatures at fuselage location for 0.1-in. step and 0.05-in. initial gap.

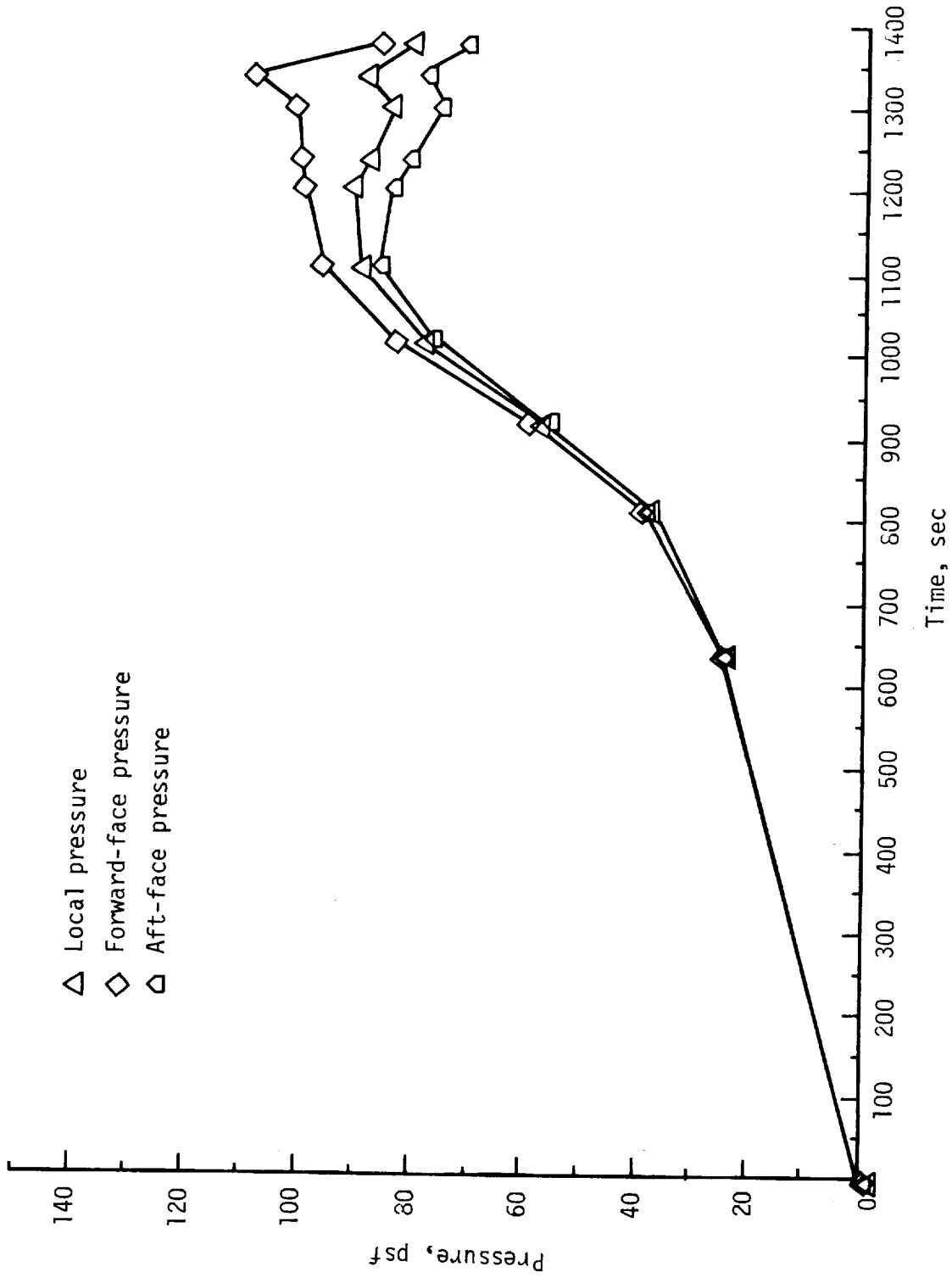


Figure 40.- Pressures at fuselage location for 0.04-in. step.

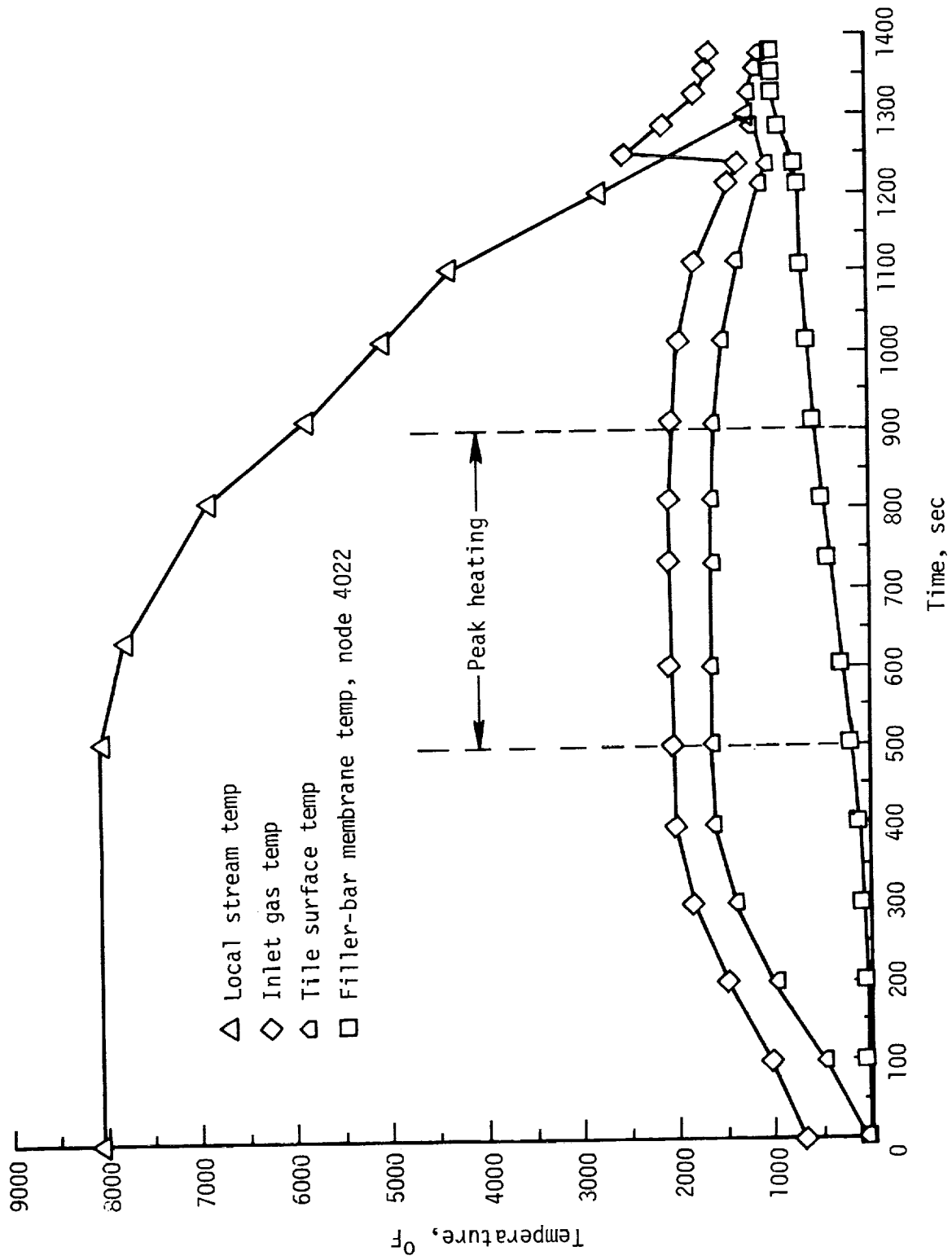


Figure 41.- Gap temperatures at fuselage location for 0.04-in. step and 0.05-in. initial gap.

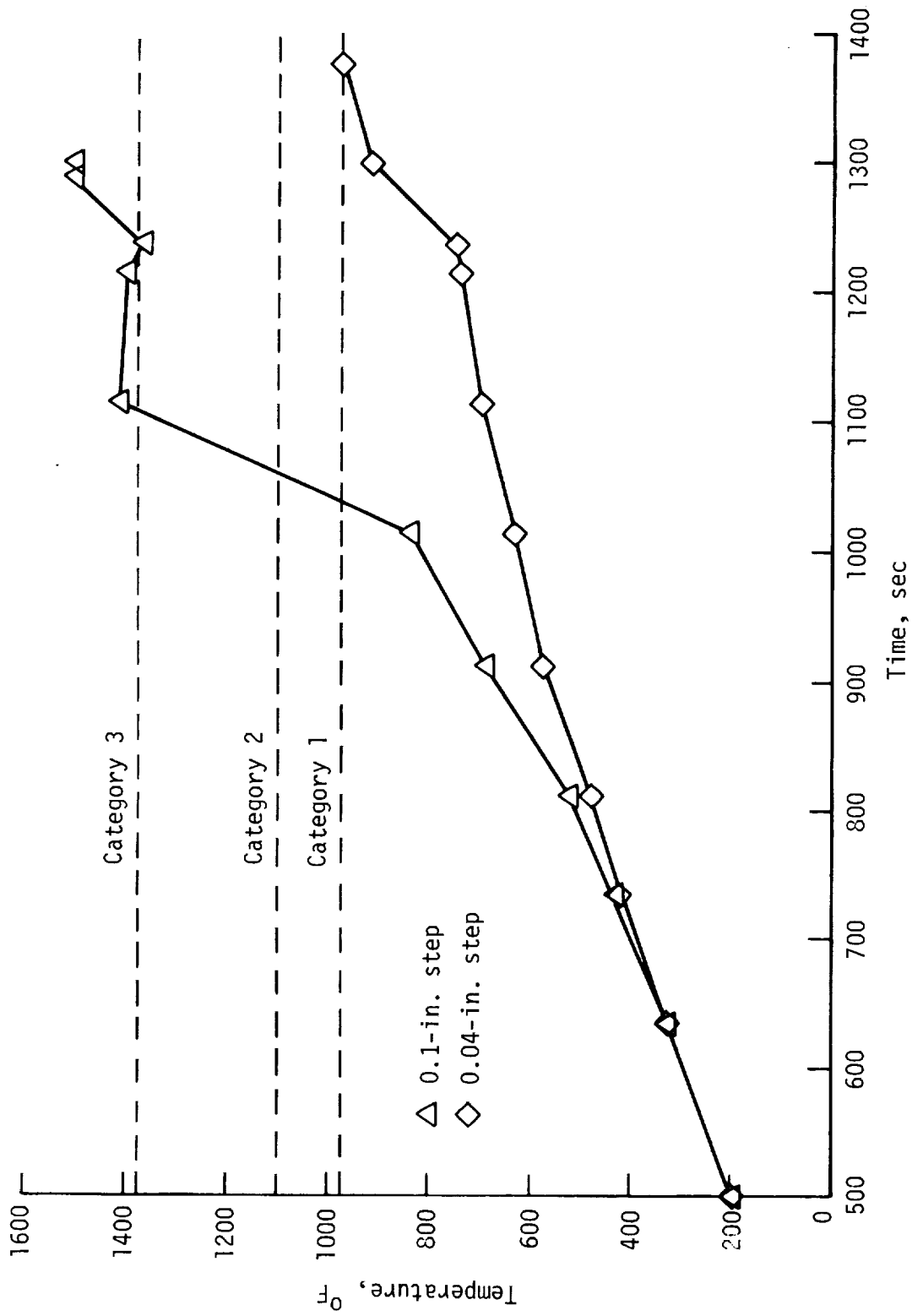


Figure 42.- Calculated temperatures at fuselage location for filler-bar membrane node of highest peak temperature, node 4022.

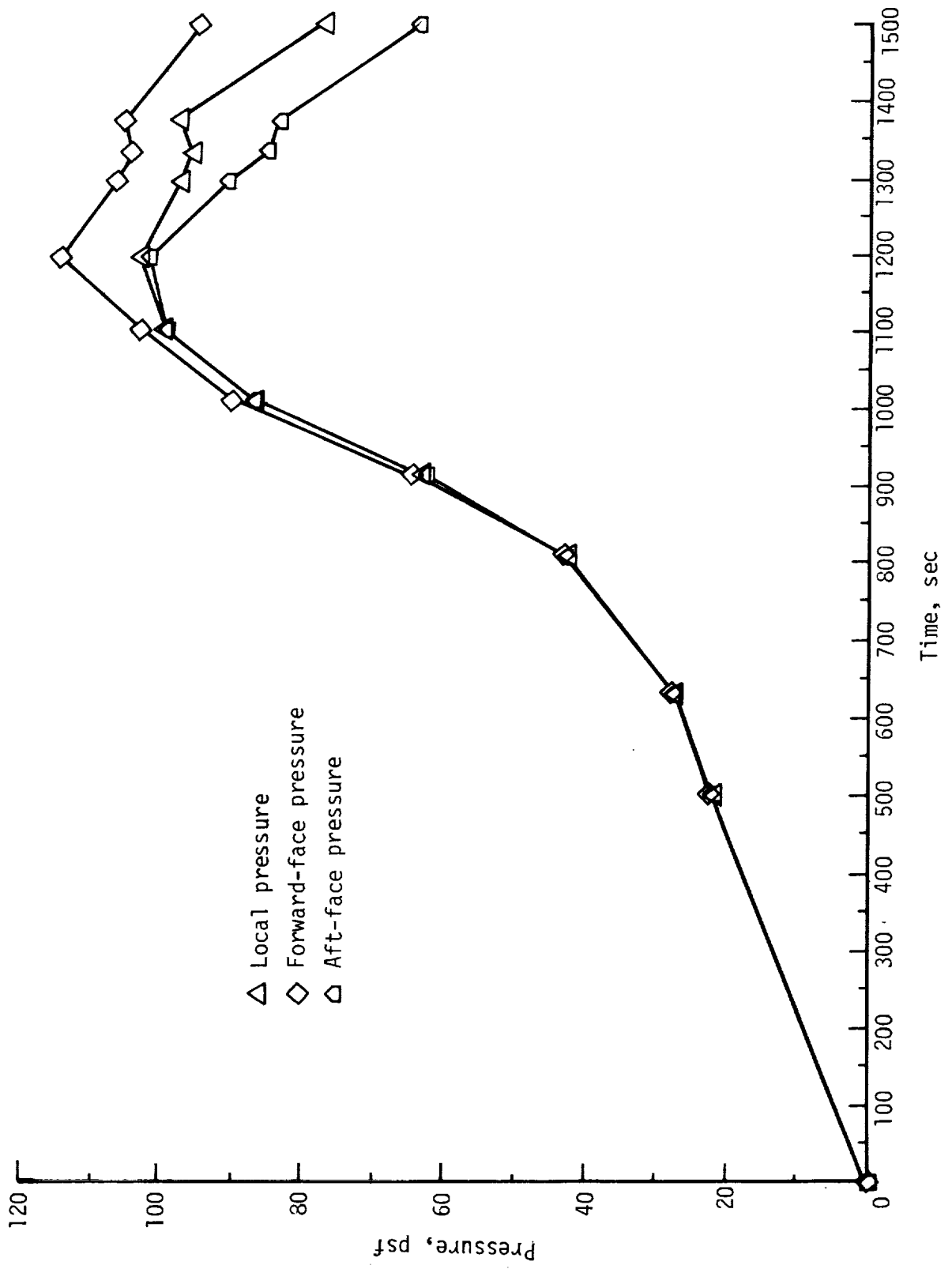


Figure 43.- Pressures at wing location for 0.017-in. step.

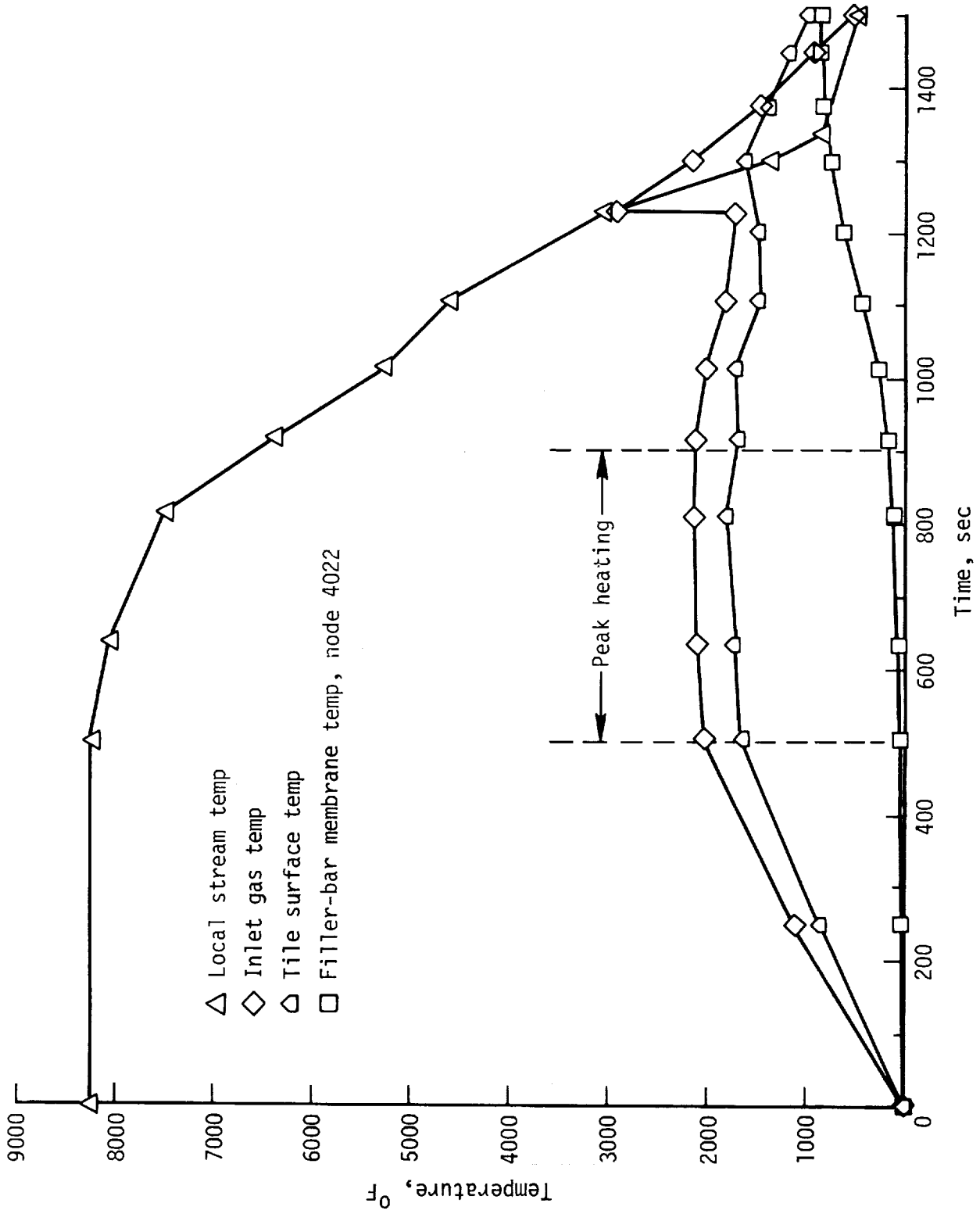


Figure 44.- Gap temperatures at wing location for 0.017-in. step and 0.05-in. initial gap.

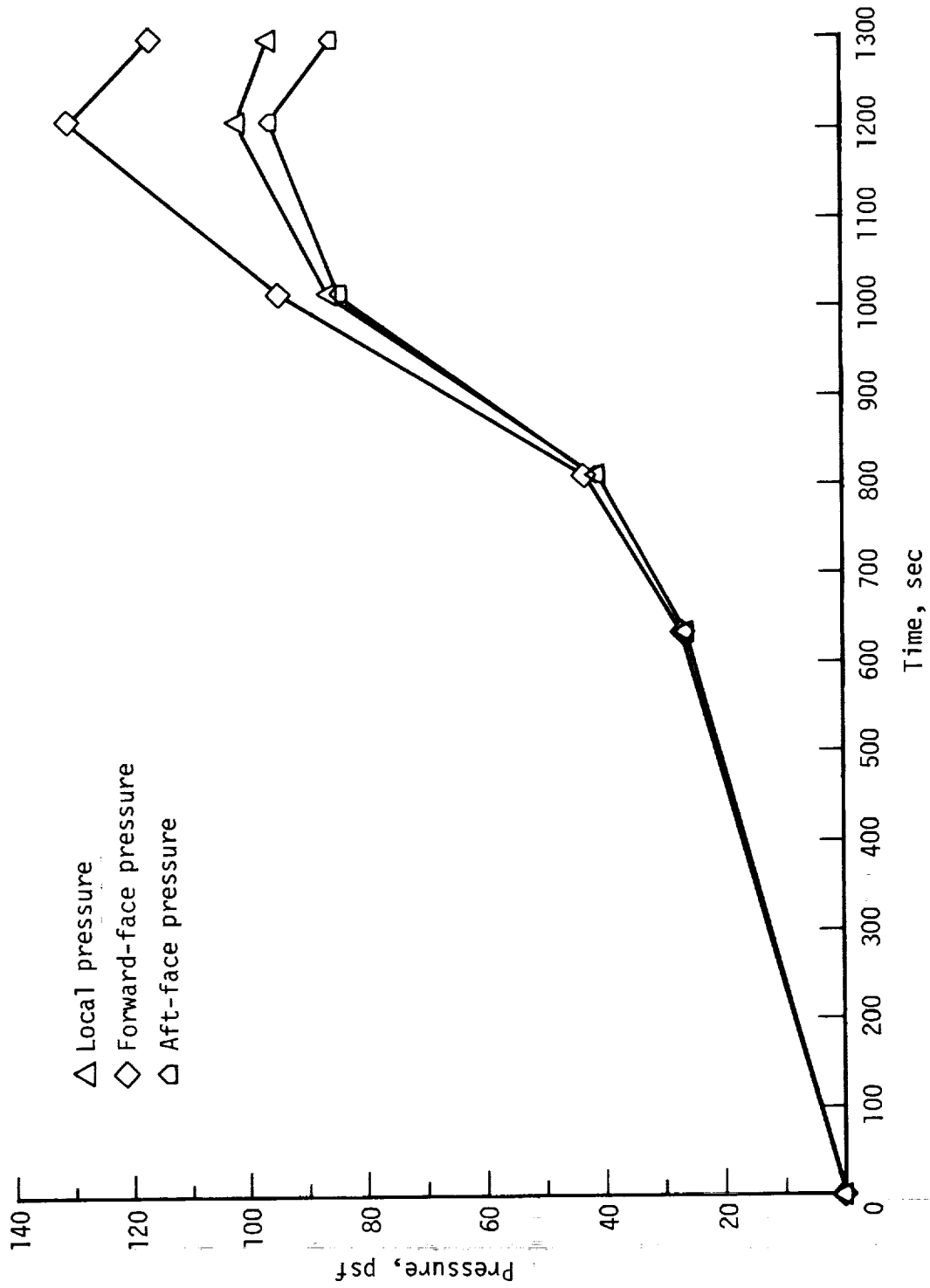


Figure 45.- Pressures at wing location for 0.03-in. step.

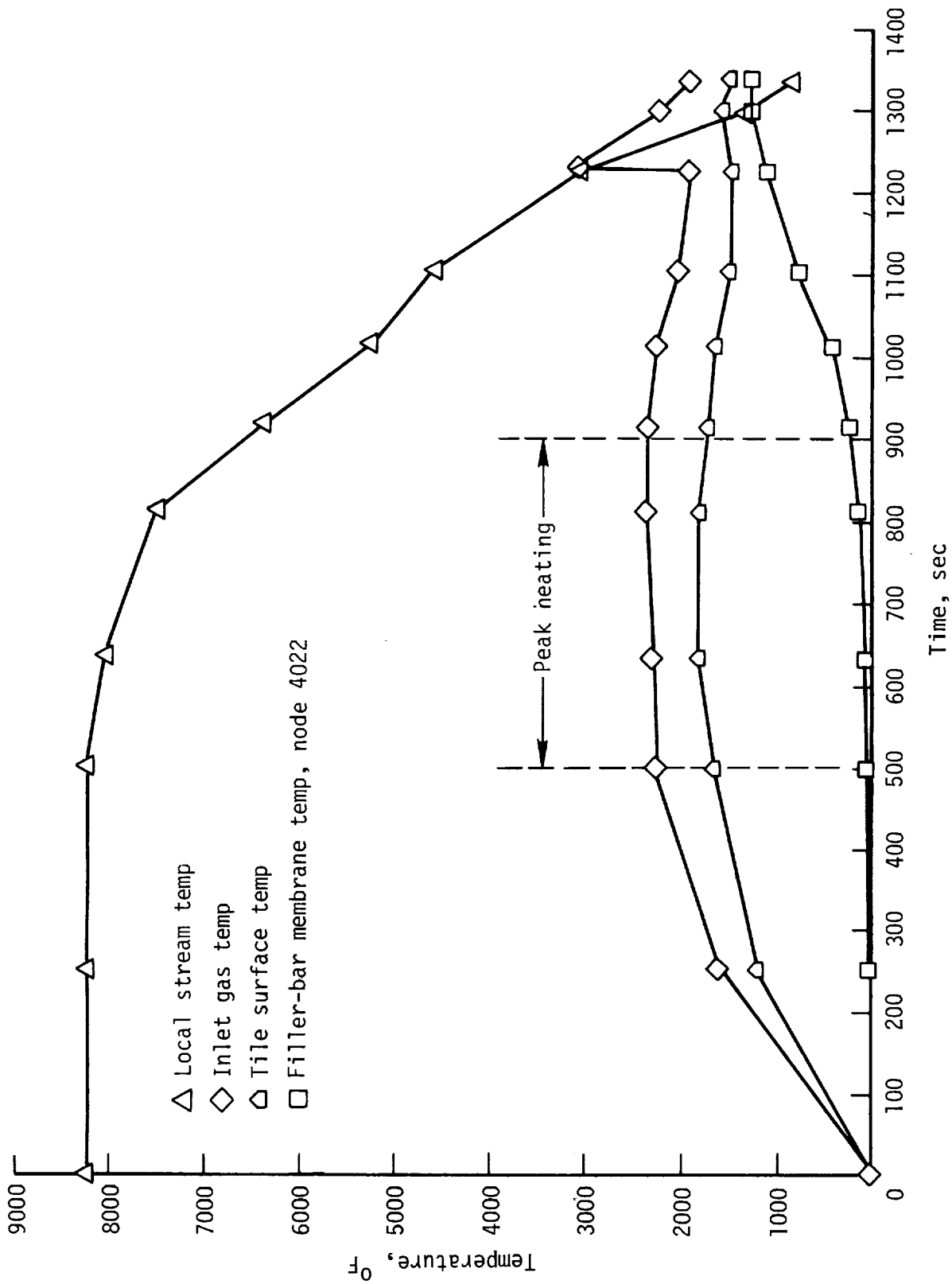


Figure 46.- Gap temperatures at wing location for 0.03-in. step and 0.05-in. initial gap.

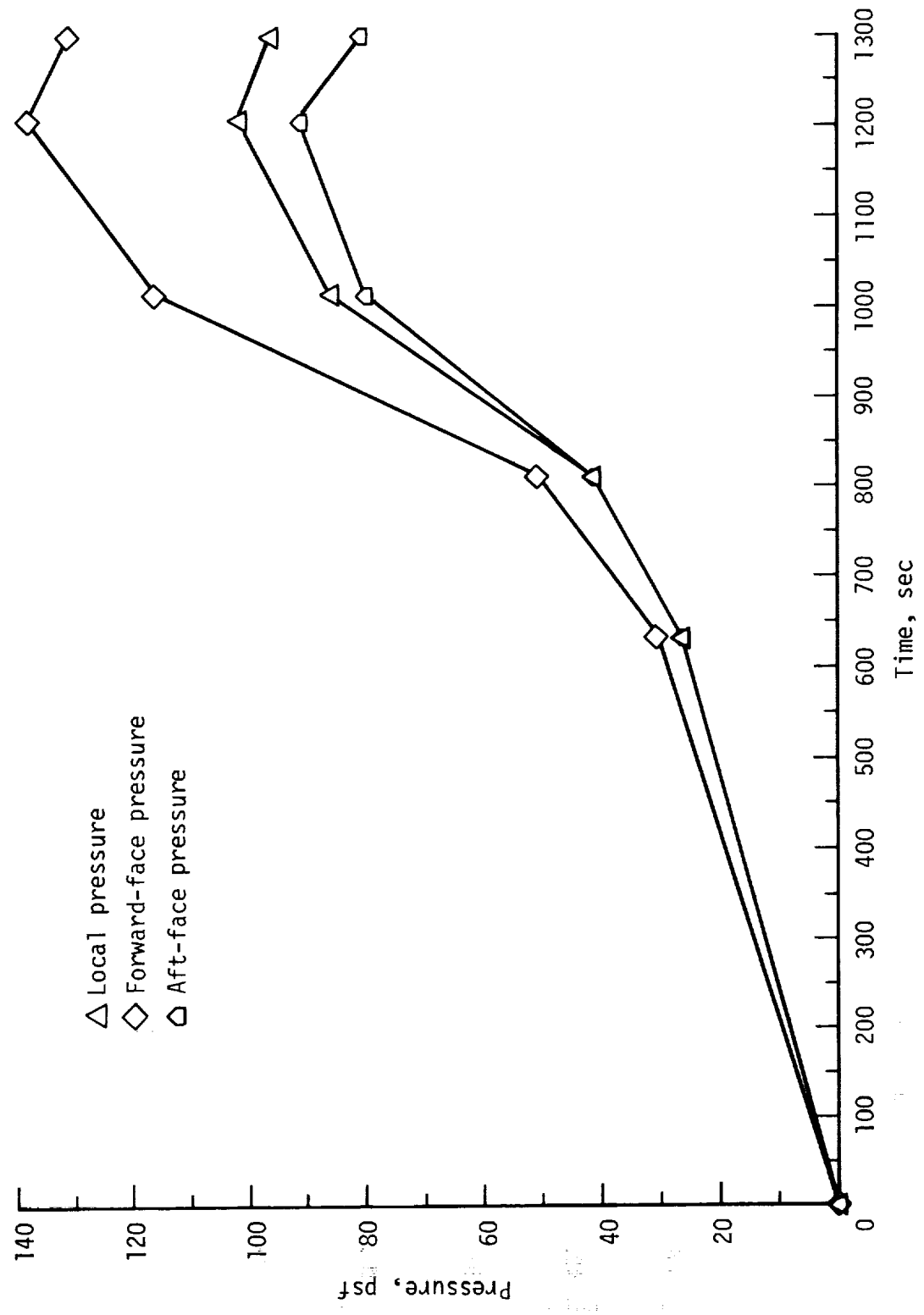


Figure 47.- Pressures at wing location for 0.06-in. step.

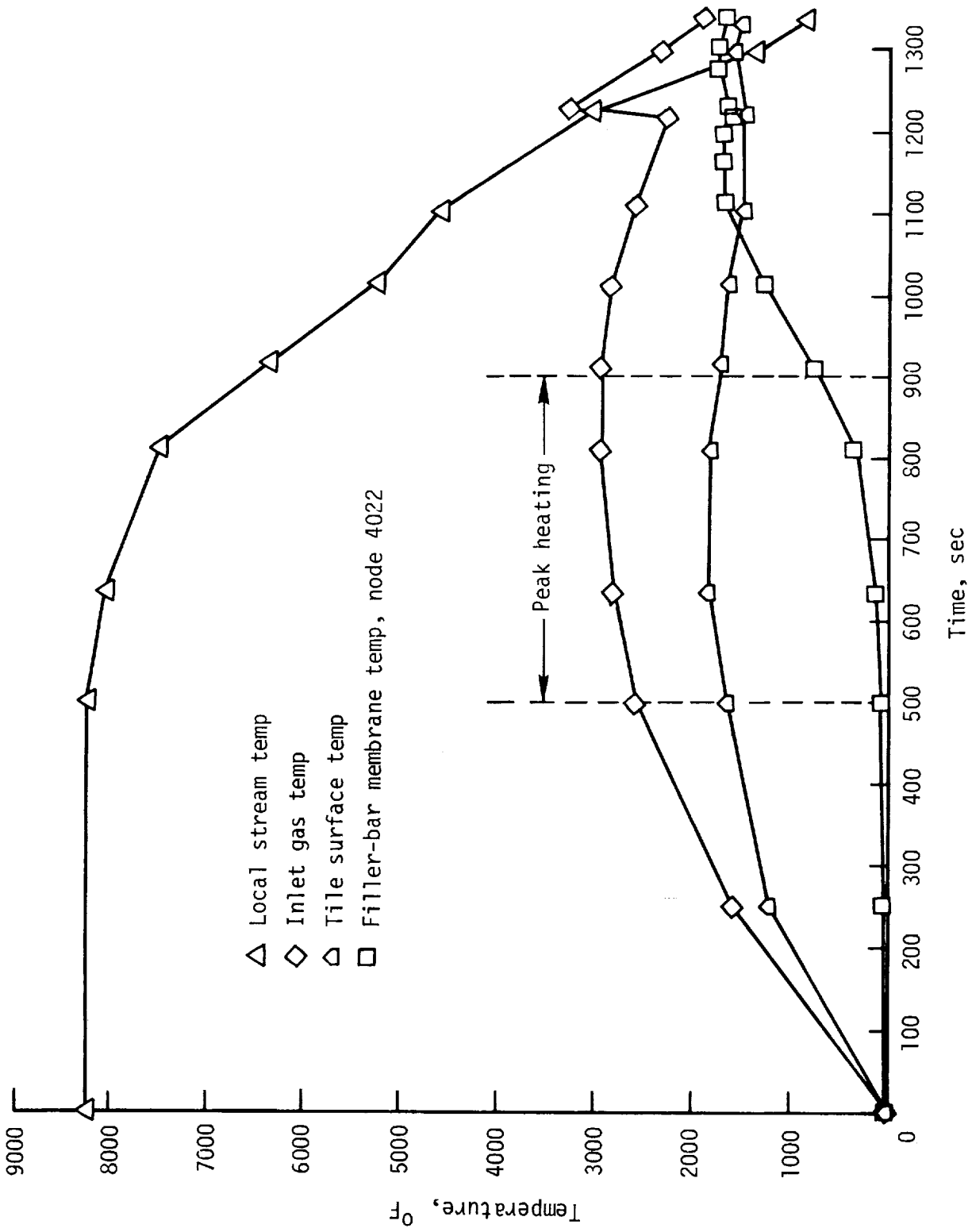


Figure 48.- Gap temperatures at wing location for 0.06-in. step and 0.05-in. initial gap.

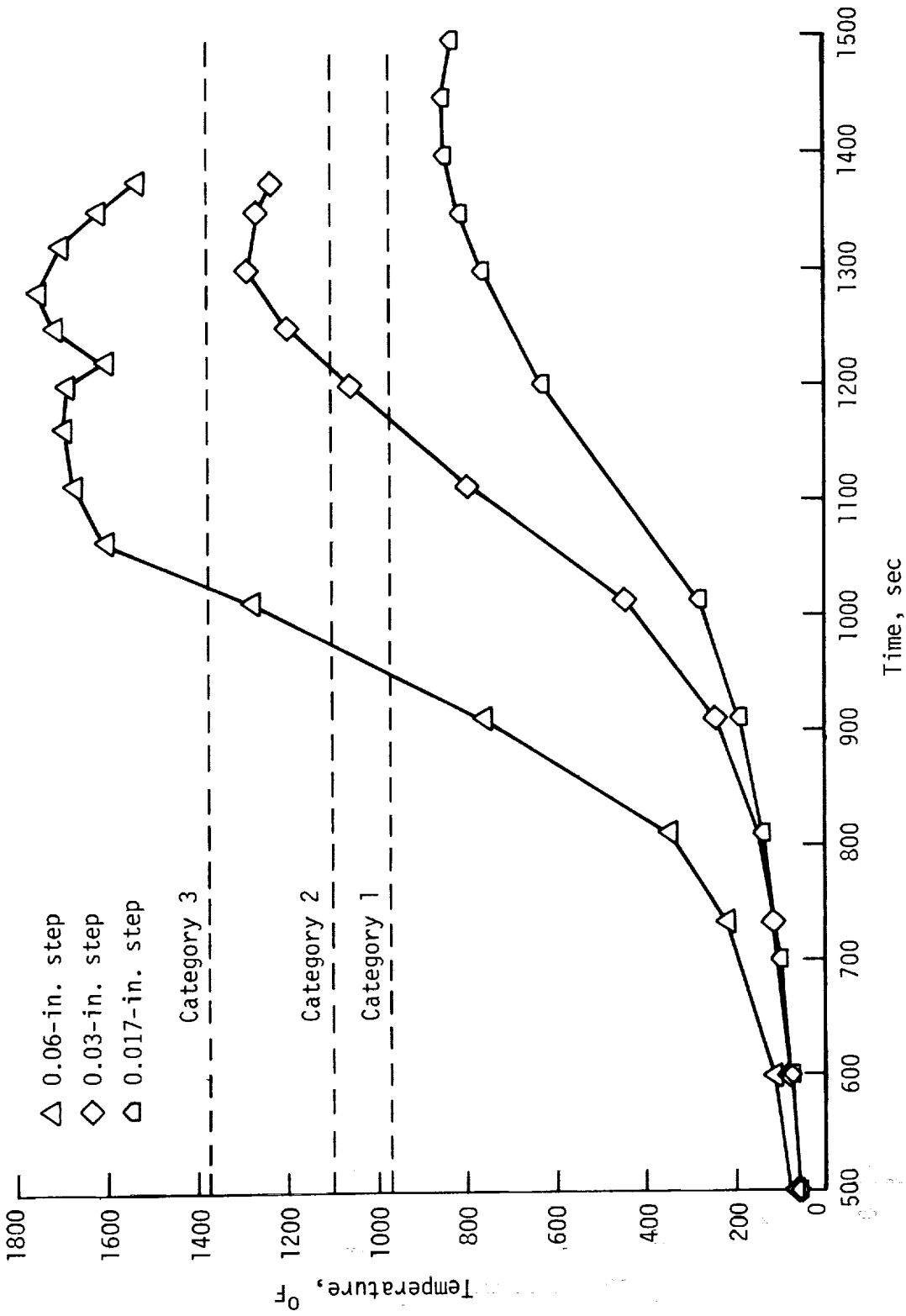


Figure 49.- Calculated temperatures at wing location for filler-bar membrane node of highest peak temperature, node 4022.

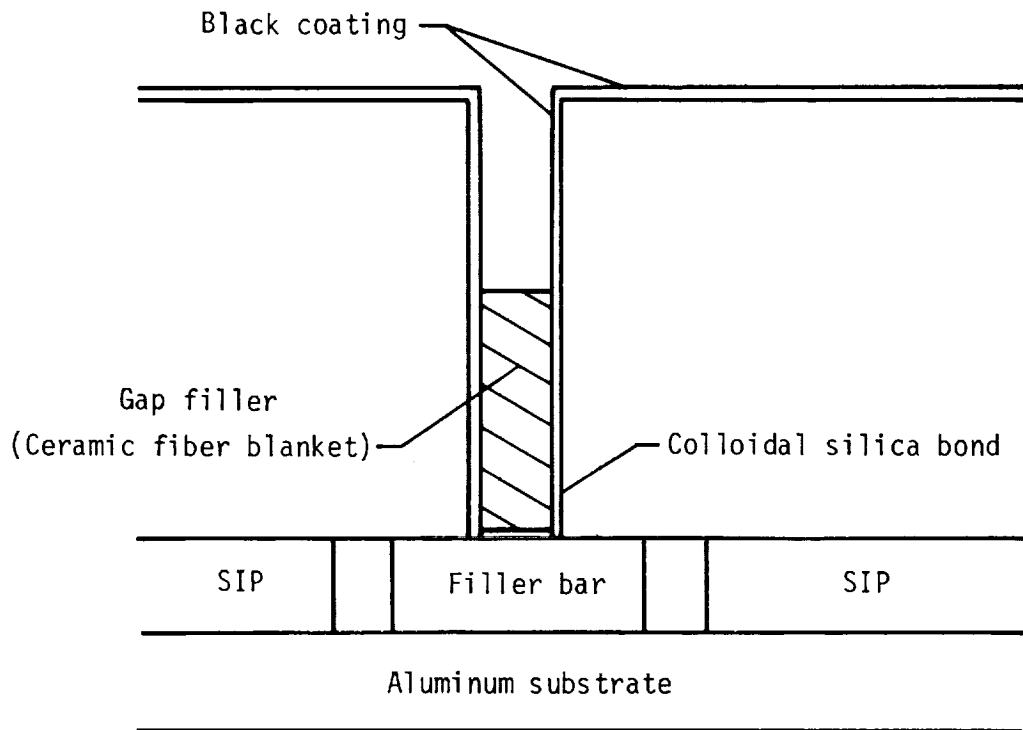


Figure 50.- Ceramic fiber gap-filler concept.

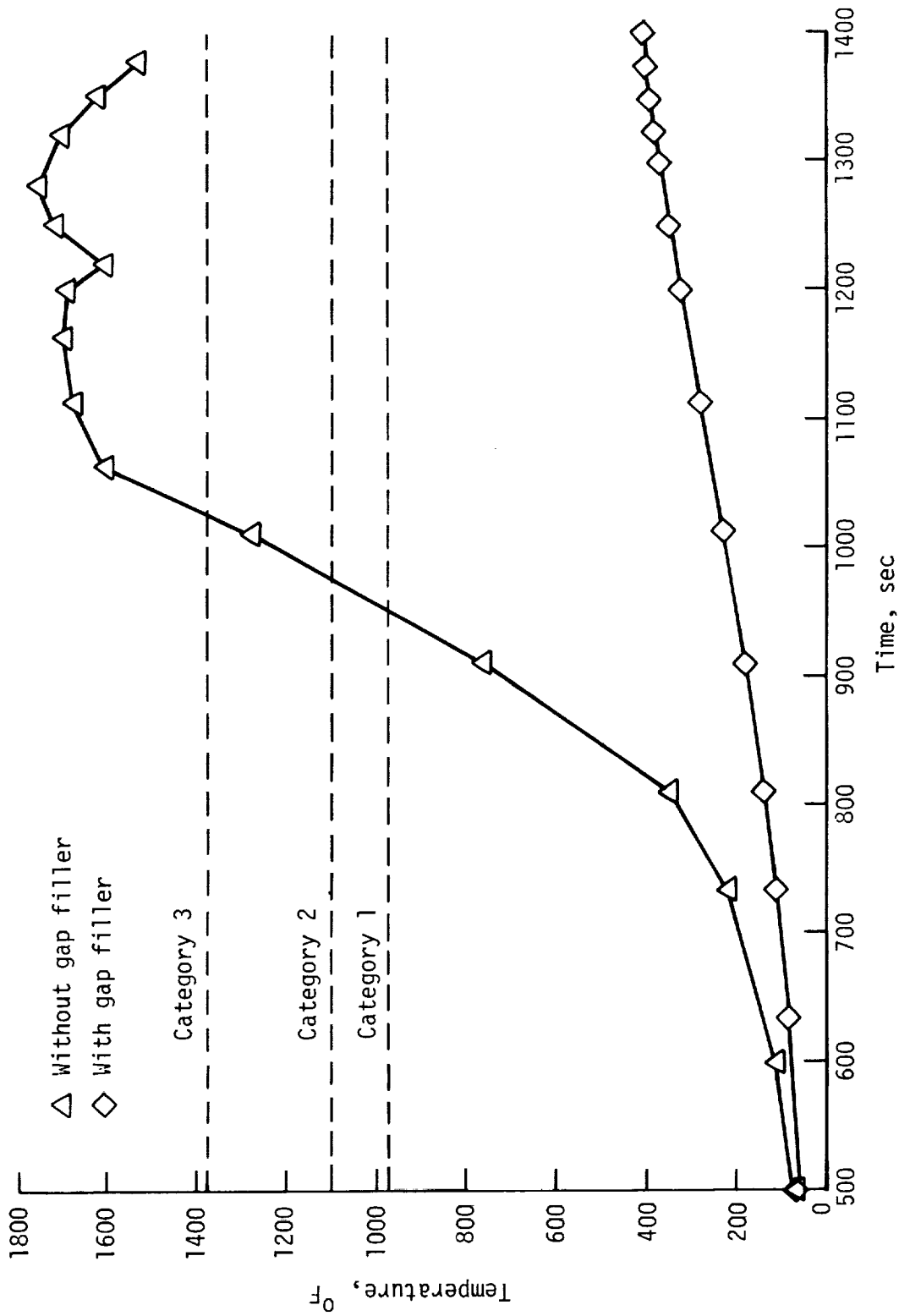
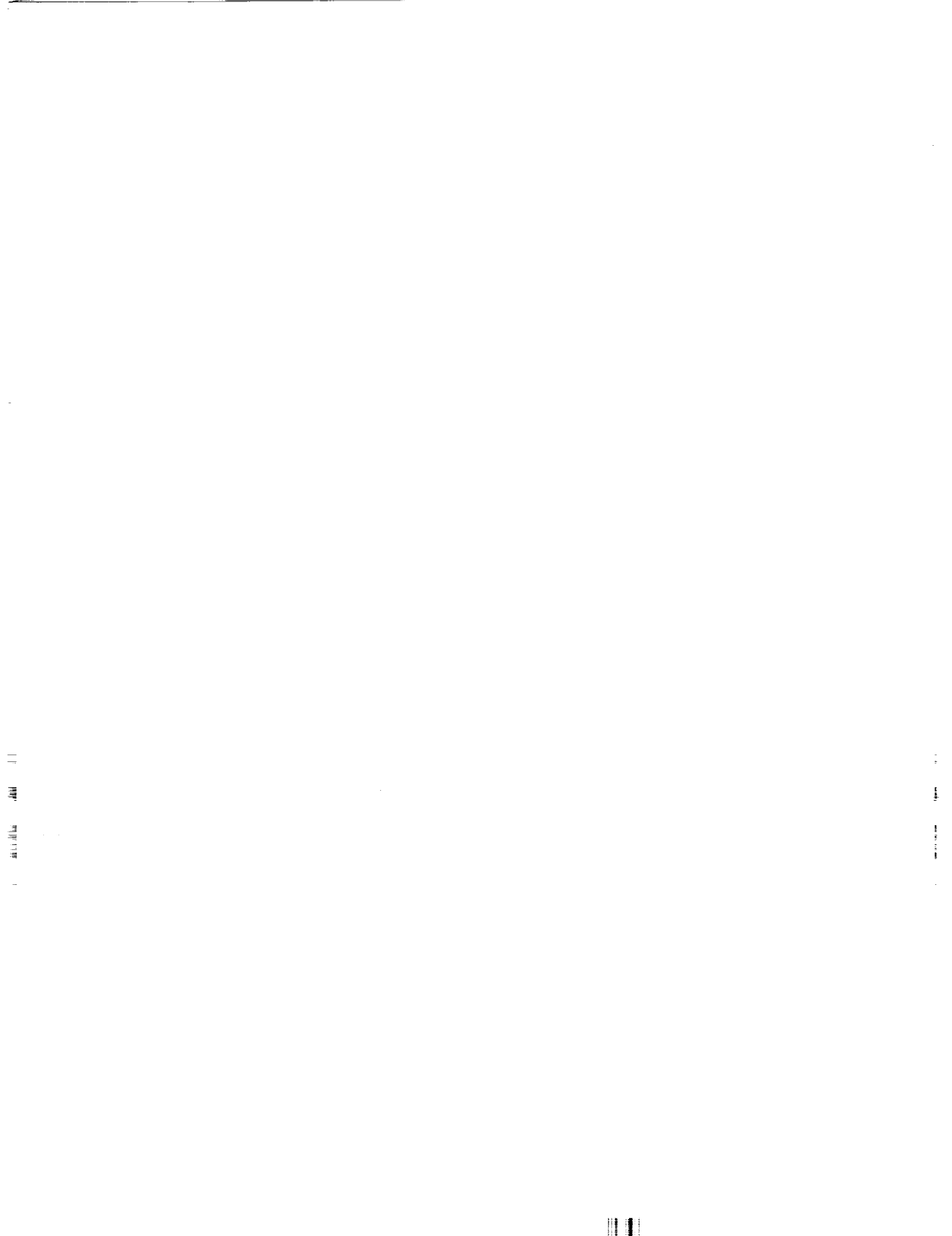


Figure 51.- Calculated temperatures of filler-bar-membrane node 4022, with half-height gap filler (Carborundum Fiberfrax 880JH) and without, at wing location, with 0.06-in. step and 0.05-in. initial gap.



1. Report No. NASA TP-2209		2. Government Accession No.		3. Recipient's Catalog No.	
4. Title and Subtitle ANALYSIS OF GAP HEATING DUE TO STEPPED TILES IN THE SHUTTLE THERMAL PROTECTION SYSTEM				5. Report Date August 1983	
				6. Performing Organization Code 986-15-10-04-00	
7. Author(s) D. H. Petley, D. M. Smith, C. L. W. Edwards, and A. B. Carlson				8. Performing Organization Report No. L-15636	
				10. Work Unit No.	
9. Performing Organization Name and Address NASA Langley Research Center Hampton, VA 23665				11. Contract or Grant No.	
				13. Type of Report and Period Covered Technical Paper	
12. Sponsoring Agency Name and Address National Aeronautics and Space Administration Washington, DC 20546				14. Sponsoring Agency Code	
15. Supplementary Notes					
16. Abstract Analytical methods used to investigate entry gap heating in the Shuttle orbiter thermal protection system are described. Analytical results are given for a fuselage lower-surface location and a wing lower-surface location. These are locations where excessive gap heating occurred on the first flight of the Shuttle. The results of a study to determine the effectiveness of a half-height ceramic fiber gap filler in preventing hot-gas flow in the tile gaps are also given.					
17. Key Words (Suggested by Author(s)) Thermal protection system Entry heating Channel flow Gap heating Flow over steps			18. Distribution Statement Unclassified - Unlimited Subject Category 18		
19. Security Classif. (of this report) Unclassified		20. Security Classif. (of this page) Unclassified		21. No. of Pages 99	22. Price A05